DEPARTMENT OF HIGH-ENERGY PHYSICS
NATIONAL CENTRE FOR NUCLEAR RESEARCH
ŚWIERK

Study of η meson leptonic decays with WASA detector

Badanie rozpadów leptonowych mezonu η przy detektorze WASA

Marcin Berłowski

supervised by
prof. dr hab. Joanna Stepaniak

WARSAW 2013

Rodzicom

Abstract

The experiment took place at the Institute for Nuclear Physics of the Forschungszentrum Juelich in Germany using Wide Angle Shower Apparatus (WASA) detection system. The detector was installed at the Cooler Synchrotron (COSY) storage ring. Data sample was collected using the reaction $pp \to pp\eta$ at the incident proton energy of 1.4 GeV.

The analysis dedicated mainly to a search for the very rare $\eta \to e^+e^-$ decay is presented. The experimental branching ratio upper limit for this decay is three orders of magnitude larger then value predicted from the Standard Model calculations. The small probability of this decay makes the process very sensitive to possible nonconventional interaction which could lead to significant increase of the branching ratio.

The collected data sample corresponds to about $5.91 \cdot 10^7$ produced η mesons used in the analysis. The performance of the WASA detector was investigated using more frequent η meson decay channels like $\eta \to \gamma\gamma$ and $\eta \to e^+e^-\gamma$. Those two decay modes served as a testing field for the extraction of the reconstruction efficiency, cross-check of normalization and moreover for testing the response of the detector for both charged and neutral particles of various energies. The lack of the signal candidates leads to the branching ratio upper limit of $3.9 \cdot 10^{-6}$ *at CL* 90%, which is slightly better than the best present measurement from the HADES Collaboration.

Abstrakt

Eksperyment został przeprowadzony w Instytucie Fizyki Jądrowej przy Forschungszentrum Juelich w Niemczech. Użyty został w tym celu układ eksperymentalny WASA zainstalowany przy pierścieniu akumulującym COSY. Zostały zebrane dane dotyczące reakcji $pp \to pp\eta$, przy energii padających protonów 1,4 GeV.

W pracy przedstawiona jest analiza dedykowana głównie poszukiwaniu bardzo rzadkiego rozpadu $\eta \to e^+e^-$. Najnowszy pomiar limitu na ten rozpad jest około trzy rzędy wielkości większy od wartości przewidzianej obliczeniami w Modelu Standardowym. Małe prawdopodobieństwo tego rozpadu powoduje, iż proces ten jest bardzo wrażliwy na hipotetyczne niekonwencjonalne oddziaływania mogące prowadzić do istotnego wzrostu stosunku rozgałęzień.

Zebrana próbka danych eksperymentalnych odpowiada w przybliżeniu liczbie $5,91 \cdot 10^7$ wyprodukowanych mezonów η użytych w analizie. Działanie detektora było badane za pomocą częstszych rozpadów mezonu η na dwa fotony oraz foton i parę elektron-pozytron. Te dwa kanały rozpadu posłużyły jako pole testowe do zbadania zdolności rekonstrukcji detektora, sprawdzenia normalizacji pomiędzy kanałami oraz przeanalizowania odpowiedzi detektora na cząstki naładowane i neutralne o różnych energiach. Mała liczba możliwych kandydatów na rozpad $\eta \to e^+e^-$ jest, przy uwzględnieniu błędów, zgodna ze spodziewaną liczbą przypadków pochodzących z tła. Brak widocznych przypadków sygnału prowadzi do górnego ograniczenia na stosunek rozgałęzień $BR_{limit} < 3,9 \cdot 10^{-6}$ przy poziomie ufności 90%. Podany wynik jest nieznacznie lepszy od najnowszego pomiaru pochodzącego z kolaboracji HADES.

Contents

1 Theoretical Foundations and Present Status **1**
1.1 The η Meson . . . 1
1.2 The $\eta \to e^+e^-$ Decay in the Frame of Standard Model . . . 1
1.3 Experimental Results on $\eta \to e^+e^-$ Decay . . . 4
1.4 The $\eta \to e^+e^-$ Decay as a Probe of the New Physics . . . 5

2 Experiment **6**
2.1 Pellet Target . . . 7
2.2 Central Detector . . . 7
2.2.1 Coordinate System . . . 8
2.2.2 Scattering Chamber . . . 8
2.2.3 Superconducting Solenoid . . . 8
2.2.4 Mini Drift Chamber . . . 10
2.2.5 Plastic Scintillator Barrel . . . 10
2.2.6 Scintillating Electromagnetic Calorimeter . . . 11
2.3 Forward Detector . . . 13
2.4 The Light Pulser System . . . 15
2.5 Data Acquisition . . . 17
2.6 Trigger System . . . 18

3 Analysis **19**
3.1 Software Tools . . . 19
3.1.1 Monte Carlo Generation . . . 19
3.1.2 WASA Monte Carlo Detector Simulation . . . 20
3.1.3 Root Sorter Reconstruction Framework . . . 20
3.2 Track Reconstruction . . . 21
3.2.1 Forward Detector . . . 21
3.2.2 Central Detector . . . 22
3.3 Trigger Evaluation . . . 25
3.3.1 Trigger Concept . . . 25
3.3.2 Trigger Definition in the Experiment . . . 26
3.3.3 The Energy Trigger Effects . . . 27
3.3.4 Hardware Signals from the Energy Trigger . . . 27
3.3.5 Efficiency of the Energy Trigger . . . 28
3.3.6 Threshold of the Energy Trigger . . . 28
3.3.7 Monte Carlo Simulation of Trigger Response . . . 30
3.4 Rest Gas Contribution . . . 31
3.4.1 Monte Carlo Simulations for the Rest Gas Events . . . 31
3.4.2 Rest Gas Contamination in the Data . . . 34
3.5 External Conversion . . . 35

4 Normalization Using $pp \to pp(\eta \to \gamma\gamma)$ Reaction **40**

5 Analysis of $pp \to pp(\eta \to e^+e^-\gamma)$ Reaction **49**
5.1 Introduction 49
5.2 The $pp \to pp(\eta \to e^+e^-\gamma)$ Reaction Simulation 49
5.3 Time Cuts and Particle Multiplicities 51
5.4 Selection 56
5.5 Simulated Background Channels 60
5.6 Final Distributions for the $e^+e^-\gamma$ Decay 61

6 Search for $pp \to pp(\eta \to e^+e^-)$ Reaction **65**
6.1 The $\eta \to e^+e^-$ Signature 65
6.2 Background Reaction Channels to the $\eta \to e^+e^-$ Decay 67
6.2.1 The $pp \to pp\pi^+\pi^-$ 67
6.2.2 The $pp \to pp(\eta \to e^+e^-\gamma)$ 67
6.2.3 Dalitz Decays of Baryonic Resonances 68
6.2.4 Combinatorial Background 68
6.3 Monte Carlo Simulations 70
6.3.1 Signal from the $\eta \to e^+e^-$ 70
6.3.2 The $pp \to pp\pi^+\pi^-$ 70
6.3.3 The $pp \to pp(\eta \to e^+e^-\gamma)$ 70
6.3.4 Radiative Decay of Baryonic Resonances 71
6.3.5 Summary of Monte Carlo Simulations 71
6.4 Selection of the $\eta \to e^+e^-$ Event Candidates 71
6.5 Cut Optimization 73
6.6 Analysis of the $\eta \to e^+e^-$ Decay Channel 76

7 Results **82**
7.1 Background Contribution 82
7.2 Final Analysis of the $\eta \to e^+e^-$ Decay 85

8 Summary and Outlook **87**

Bibliography **88**

List of Figures

1 Pseudoscalar meson multiplet 1
2 Triangle diagram for the $P \to l^+l^-$ process 2
3 Table of η meson decays measured in Berłowski *et al.* 4
4 Overview of the WASA detector 6
5 Overview of the WASA pellet target 7
6 Beryllium beam pipe and crossing it pellet target tubes 9
7 Magnetic flux density map 9
8 The Mini Drift Chamber photographs 10
9 A schematic view of the ionization process in the straw 11
10 3D view of the central part of the Plastic Scintillator Barrel 12
11 Forward, central and backward parts of the Plastic Scintillator Barrel 12
12 One full section of the Plastic Scintillator Barrel 13
13 3D cross-section of the Scintillating Electromagnetic Calorimeter 13
14 Polar angle θ coverage of the Scintillating Electromagnetic Calorimeter 14
15 Schematic view of Forward Range Hodoscope 14
16 Schematic view of Forward Trigger Hodoscope 15
17 Schematic view of Forward Proportional Chamber 16
18 Schematic view of Forward Window Counter 16
19 The data acquisition system schematics 17
20 The trigger system overview 18
21 Flow chart of the analysis chain 19
22 Simulation of protons in the forward detector 22
23 Helix parametrization used for Mini Drift Chamber track reconstruction 24
24 Event display for a reconstructed event 25
25 Energy deposit in one half of electromagnetic calorimeter as a function of the deposit in the other one for $\eta \to \gamma\gamma$ simulation 26
26 3D cross section of the Scintillating Electromagnetic Calorimeter and its polar angle θ coverage 26
27 Photon θ and ϕ angle distribution for $\eta \to \gamma\gamma$ decay candidates 28
28 Invariant mass plots used for the efficiency calculations of the energy trigger for $\eta \to \gamma\gamma$ and $\eta \to e^+e^-\gamma$ reactions 29
29 The distributions of energy deposits in either half of electromagnetic calorimeter for data events with or without energy trigger tag 30
30 The distribution of the relation between the number of events with specific energy deposit with or without energy trigger tagged. 30
31 The simulation of flat contribution of the rest gas along z (beam) axis 32
32 Z vertex coordinate for Monte Carlo simulations with rest gas only 32
33 Invariant mass of two photons for $\eta \to \gamma\gamma$ with rest gas only Monte Carlo simulation 33
34 Reconstructed z vertex coordinate for $\eta \to e^+e^-\gamma$ simulation 33
35 Efficiency of z vertex coordinate reconstruction for $\eta \to e^+e^-\gamma$ simulation 33
36 Reconstructed z vertex coordinate for data events before and after efficiency correction 34

37 Reconstructed x and y vertex coordinate 35
38 Plot of the vertex distance as a function of the invariant mass of e^+e^- pairs calculated at the beam pipe position 36
39 The illustration of the effect on non-conversion and conversion pairs 36
40 Reconstructed vertex position in the XY plane 37
41 The value of reconstructed vertex distance 37
42 Invariant mass of electron-positron pair before and after conversion cut . . . 38
43 Invariant mass of e^+e^- pair after external conversion subtraction from data 38
44 Plot of the vertex distance as a function of the invariant mass of e^+e^- pairs calculated at the beam pipe position alternate approach 39
45 Charged tracks multiplicity in the Forward Detector per event in $\eta \to \gamma\gamma$ . . 40
46 Number of neutral tracks in the Central Detector per event in $\eta \to \gamma\gamma$ 40
47 Time difference between charged tracks in the Forward Detector in $\eta \to \gamma\gamma$. 41
48 Emission angle between selected two neutral tracks in the central detector in the XY plane in $\eta \to \gamma\gamma$ 41
49 Time difference between mean time of charged tracks in the Forward Detector and neutral tracks in the Central Detector in $\eta \to \gamma\gamma$ 41
50 Time difference between neutral tracks in the Central Detector in $\eta \to \gamma\gamma$ . . 42
51 Invariant mass of two photons and missing mass of two protons distributions for events with two or more photons in $\eta \to \gamma\gamma$ 42
52 Invariant mass of two photons for events with different number of high energy photons in $\eta \to \gamma\gamma$ 43
53 Invariant mass of two photons distribution for data events in the function of missing mass of two protons in $\eta \to \gamma\gamma$ 43
54 Energy deposits in each half of Electromagnetic Calorimeter in $\eta \to \gamma\gamma$ . . . 44
55 Invariant mass of two photons distribution for data events with fitted signal shape above polynomial background 44
56 Systematic effect on invariant mass of $\gamma\gamma$ of missing mass of two protons condition 46
57 Systematic effect on invariant mass of $\gamma\gamma$ of threshold on energy deposits . . 46
58 Systematic effect on invariant mass of $\gamma\gamma$ using gaussian shape for the signal distribution 47
59 Systematic effect on invariant mass of $\gamma\gamma$ using different ranges of fit 47
60 Feynman diagram showing the $\eta \to e^+e^-\gamma$, QED e^+e^- mass distribution and the squared transition form factor as a function of e^+e^- mass 50
61 Charged tracks multiplicity in the Forward Detector per event in $\eta \to e^+e^-\gamma$ 51
62 Charged tracks multiplicity in the Central Detector per event in $\eta \to e^+e^-\gamma$ 52
63 Neutral tracks multiplicity in the Central Detector per event in $\eta \to e^+e^-\gamma$. 52
64 Time difference between charged tracks in the Forward Detector in $\eta \to e^+e^-\gamma$ 52
65 Emission angle between selected two charged tracks in the central detector in the XY plane versus invariant mass of electron-positron pair in $\eta \to e^+e^-\gamma$ 53
66 Time difference between mean time of charged tracks in the Forward Detector and charged tracks in the Central Detector in $\eta \to e^+e^-\gamma$ 53
67 Time difference between charged tracks in the Central Detector in $\eta \to e^+e^-\gamma$ 54

68 Time correlation between charged tracks in the Central Detector and Plastic Scintillator hits in $\eta \to e^+e^-\gamma$ 54
69 Opening angle in the XY plane between selected two charged tracks in the central detector and one neutral track in $\eta \to e^+e^-\gamma$ 55
70 Time difference between the mean time of charged tracks in the Forward Detector and neutral tracks in the Central Detector in $\eta \to e^+e^-\gamma$ 55
71 Invariant mass of electron-positron pair in $\eta \to e^+e^-\gamma$ before channel selection 56
72 Missing mass of two protons as a function of invariant mass of $e^+e^-\gamma$ for events in data with a small invariant masses of electron-positron pairs in $\eta \to e^+e^-\gamma$ 56
73 Missing mass of two protons in $\eta \to e^+e^-\gamma$ 57
74 Invariant mass of electron-positron pair in $\eta \to e^+e^-\gamma$ 57
75 Opening angle between electron and positron in the LAB frame in $\eta \to e^+e^-\gamma$ 57
76 Emission angle of the η meson in the LAB frame in $\eta \to e^+e^-\gamma$ 58
77 Opening angle between electron-positron pair and photon in the LAB frame in $\eta \to e^+e^-\gamma$ 58
78 Missing mass of electron-positron pair and photon distribution in $\eta \to e^+e^-\gamma$ 59
79 Identification plot of ratio R equal to momentum divided by deposited energy in $\eta \to e^+e^-\gamma$ 59
80 Energy deposits in each half of the Electromagnetic Calorimeter in $\eta \to e^+e^-\gamma$ 60
81 Invariant mass of $e^+e^-\gamma$ for events with different number of photons in $\eta \to e^+e^-\gamma$ 61
82 Invariant mass of $e^+e^-\gamma$ for the final selection of the $\eta \to e^+e^-\gamma$ channel . . 62
83 Invariant mass of electron-positron pair for the final selection of the $\eta \to e^+e^-\gamma$ channel 62
84 Missing mass of two protons for the final selection of the $\eta \to e^+e^-\gamma$ channel 63
85 Invariant mass of $e^+e^-\gamma$ for the final selection of the $\eta \to e^+e^-\gamma$ channel using fit to the data 64
86 Missing mass of two protons after reconstruction for $\eta \to e^+e^-$ and $pp \to pp\pi^+\pi^-$ simulations 65
87 Invariant mass of electron-positron pair after reconstruction for $\eta \to e^+e^-$ and $pp \to pp\pi^+\pi^-$ simulations 66
88 Opening angle of electron-positron pair after reconstruction for $\eta \to e^+e^-$ and $pp \to pp\pi^+\pi^-$ simulations 66
89 Ratio between the particle momentum and it's deposited energy after reconstruction for $\eta \to e^+e^-$ and $pp \to pp\pi^+\pi^-$ simulations 66
90 Deposited energy of both of the central detector charged tracks after reconstruction for $\eta \to e^+e^-$ and $pp \to pp\pi^+\pi^-$ simulations 67
91 IM_{ee} cross-section for $pp \to pX$ reaction for the incident proton energy of 1.61 GeV 68
92 IM_{ee} cross-section for $pp \to pX$ reaction for various energy of protons 69
93 Forward detector charged tracks multiplicity for $\eta \to e^+e^-$ simulation and data 72
94 Time difference distribution for all combinations of charged tracks in the forward detector for $\eta \to e^+e^-$ simulation and data 72

95 Central detector charged tracks multiplicity for $\eta \rightarrow e^+e^-$ simulation and data 72
96 Opening angle between electron and positron on the XY plane for $\eta \rightarrow e^+e^-$ simulation and data . . . 73
97 Time difference between all combinations of charged tracks in the forward detector and the central detector charged tracks for $\eta \rightarrow e^+e^-$ simulation and data . . . 73
98 Time difference distribution for all combinations of charged tracks in the central detector for $\eta \rightarrow e^+e^-$ simulation and data . . . 74
99 Time correlation between all times taken from the plastic scintillator detector and time for each charged particle in central detector for $\eta \rightarrow e^+e^-$ simulation and data . . . 74
100 Invariant mass of electron-positron pair as a function of opening angle between electron and positron in simulations and data . . . 77
101 Invariant mass of electron-positron pair in simulations and data . . . 77
102 Opening angle between electron and positron in simulations and data . . . 78
103 Ratio between momentum and energy deposit in simulations and data . . . 78
104 The results of optimization procedure . . . 79
105 Deposited energy of each of the selected central detector charged track after selection for $\eta \rightarrow e^+e^-$ event candidates . . . 80
106 Opening angle between the selected central detector charged tracks on the XY plane after selection for $\eta \rightarrow e^+e^-$ event candidates . . . 80
107 Invariant mass of the selected electron and positron pair after selection for $\eta \rightarrow e^+e^-$ event candidates . . . 81
108 Identification of charged tracks in the central detector by the ratio R between momentum and energy deposited in the electromagnetic calorimeter for $\eta \rightarrow e^+e^-$ event candidates . . . 81
109 Missing mass of two protons for data $\eta \rightarrow e^+e^-$ event candidates after particle and time selection and optimization cuts . . . 83
110 Missing mass of two protons for data $\eta \rightarrow e^+e^-$ event candidates with polynomial fit to the points . . . 84

List of Tables

1 Basic properties of the η meson 2
2 The most prominent decays of the η meson 2
3 The most recent theoretical predictions for $\eta \to e^+e^-$ decay 3
4 Main properties of the pellet target system 8
5 Vertex x and y parameters obtained from data distributions using gaussian fit 34
6 Number of $\eta \to \gamma\gamma$ events in data and Monte Carlo acceptance after selection criteria 45
7 The values of systematic error estimation for the total number of η mesons produced 48
8 The acceptance for the simulated $\eta \to e^+e^-\gamma$ signal and background samples 60
9 Monte Carlo acceptance for tracks of different sign 70
10 Summary of Monte Carlo samples used in the $\eta \to e^+e^-$ analysis 71
11 Results of the cut optimization procedure in the $\eta \to e^+e^-$ analysis 79
12 Number of $\eta \to e^+e^-$ event candidates and expected background contributions 83
13 Number of $\eta \to e^+e^-$ event candidates and Monte Carlo acceptance after a given selection criteria 85

1 Theoretical Foundations and Present Status

1.1 The η Meson

The η meson along with $\pi^0, \pi^+, \pi^-, K^0, \overline{K}^0, K^+, K^-$, and η' belongs to the pseudoscalar meson multiplet within SU(3) flavor symmetry group (see fig.1). It was discovered in the collisions between pions and nucleus in 1961 at the Bevatron at Lawrence Berkeley National Laboratory. In the quark model the η meson is a linear combination of the two quantum states (η_1 and η_8) mixed with a certain angle θ:

$$\eta = \eta_8 cos(\theta) - \eta_1 sin(\theta), \tag{1}$$

where octet (η_8) and singlet (η_1) states have quark composition given by formulas:

$$\eta_8 = \frac{1}{\sqrt{6}}(u\overline{u} + d\overline{d} - 2s\overline{s})\eta_1 = \frac{1}{\sqrt{3}}(u\overline{u} + d\overline{d} + s\overline{s}) \tag{2}$$

If one express the mixing angle in the terms of ideal mixing angle $tan(\theta_i) = \frac{1}{\sqrt{2}}$, when the terms $u\overline{u} + d\overline{d}$ and $s\overline{s}$ decouple, one can obtain such an expression for the η meson pure SU(3) quark composition:

$$\eta = \frac{1}{\sqrt{2}}(u\overline{u} + d\overline{d})cos(\alpha) - s\overline{s}\ sin(\alpha), \tag{3}$$

where the new mixing angle $\alpha = \frac{\pi}{2} - \theta_i + \theta$. From the most recent experiments (see [1],[2]) we know that the value of θ angle is in the range of 14°-19°, with the best experimental result $\theta = -15.5° \pm 1.3°$ [2].

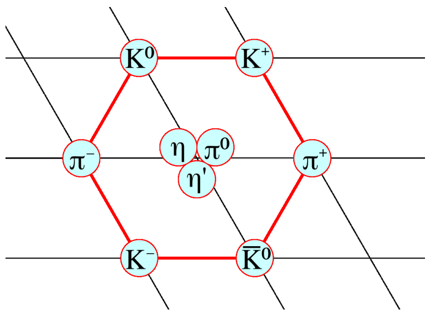

Figure 1: *Pseudoscalar meson multiplet.*

The basic properties of the η meson are covered in the tab.1.
In the tab.2 one can find the most prominent decays of the η meson.

1.2 The $\eta \to e^+e^-$ Decay in the Frame of Standard Model

In the lowest order of QED perturbation theory, the decay of the neutral meson, $P(q) \to l^-(p_-) + l^+(p_+)$, where $q^2 = M^2$, $p_\pm^2 = m^2$, (M - meson mass, m - lepton mass, and defining momenta to hold the relation $q = p_- + p_+$) is described by the one-loop Feynman amplitude

Property	Value
Mass	$(547.51 \pm 0.18)\ MeV$
Life time	$(5.0 \pm 0.3) \cdot 10^{-3}\ s$
Charge	0
Strangeness	0
Decay width	$(1.30 \pm 0.07)\ keV$
Baryon number	0
Lepton number	0
Quantum numbers $I^G(J^{PC})$	$0^+(0^{-+})$

Table 1: *Basic properties of the η meson, where I - isospin, G - G-parity, J - spin, P - parity, C - charge conjugation.*

Decay channel	Experimental measurement of the branching ratio [3]
$\eta \to \gamma\gamma$	39.31 ± 0.20 %
$\eta \to \pi^+\pi^-\pi^\circ$	22.73 ± 0.23 %
$\eta \to \pi^\circ\pi^\circ\pi^\circ$	32.56 ± 0.28 %
$\eta \to \pi^+\pi^-\gamma$	4.60 ± 0.16 %
$\eta \to e^+e^-\gamma$	0.7 ± 0.07 %

Table 2: *The most prominent decays of the η meson.*

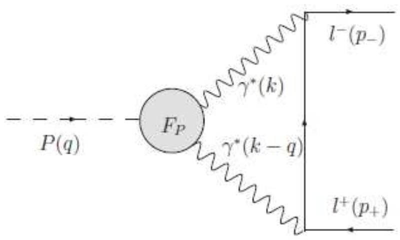

Figure 2: *Triangle diagram for the $P \to l^+l^-$ process with the pseudoscalar meson transition form factor $P \to \gamma^*\gamma^*$ in the vertex.*

(see fig.2) corresponding to the conversion of the neutral meson via two virtual photons into a lepton-antilepton pair. The normalized branching ratio is [4, 5, 6, 7]:

$$\frac{\Gamma_{P\to l^+l^-}}{\Gamma_{P\to\gamma\gamma}} = 2\beta(M^2)(\frac{\alpha m}{\pi M})^2|A(M^2)|^2, \tag{4}$$

where $\beta(q^2) = \sqrt{1-4m^2/q^2}$ and the reduced amplitude is:

$$A(q^2) = \frac{2}{q^2}\int\frac{d^4k}{i\pi^2}\frac{(qk)^2 - q^2k^2}{(k^2+i\epsilon)[(q-k)^2+i\epsilon][(p_- - k)^2 - m^2 + i\epsilon]}F_{P\to\gamma^*\gamma^*}(-k^2, -(q-k)^2), \tag{5}$$

with the transition form factor $F_{P\to\gamma^*\gamma^*}(-k^2, -q^2)$ being normalized as $F_{P\to\gamma^*\gamma^*}(0,0) = 1$. The so-called unitary bound can be extracted using the Cutkosky rules [8, 9] if in eq.(4) only the imaginary part of the amplitude, which is model independent, is taken into account:

$$ImA(q^2) = \frac{\pi}{2\beta(q^2)}ln\frac{1-\beta(q^2)}{1+\beta(q^2)}. \tag{6}$$

This is the contribution of two on-shell photons in the intermediate state. For $\eta \to e^+e^-$, using the relation $|A|^2 \geq ImA^2$, the value of unitary bound was found to be:

$$BR[\eta\to e^+e^-] = \Gamma_{\eta\to e^+e^-}/\Gamma_{total} \geq 1.78\cdot 10^{-9},$$

or in another form using as a reference η meson decay into two photons:

$$\Gamma_{\eta\to e^+e^-}/\Gamma_{\eta\to\gamma\gamma} \geq 4.51\cdot 10^{-9}.$$

The most recent theoretical calculations using various VMD versions and parametrization models like hidden gauge (see ref.[10]) and corrections for the models mentioned before like mass corrections (see ref.[11]) are collected in tab.3. The authors of ref.[12] gave the value

Decay channel	[13]	[11]	[10] hidden gauge	[10] modified VDM
$\Gamma_{\eta\to e^+e^-}/\Gamma_{total}$ (10^{-9})	4.60 ± 0.09	5.24	4.68 ± 0.01	4.65 ± 0.01

Table 3: *The most recent theoretical predictions for $\eta \to e^+e^-$ decay.*

of BR[$\eta \to e^+e^-$] as follows:

$$\Gamma_{\eta\to e^+e^-}/\Gamma_{total} = (5\pm 1)\cdot 10^{-9}.$$

The authors of ref.[14] gave predictions for this decay:

$$\Gamma_{\eta\to e^+e^-}/\Gamma_{total} = (5.8\pm 0.2)\cdot 10^{-9}.$$

In ref.[15] normalized BR value is given with respect to the η meson decay into two photons:

$$\Gamma_{\eta\to e^+e^-}/\Gamma_{\eta\to\gamma\gamma} = (6.2\pm 0.3)\cdot 10^{-8}.$$

This value corresponds to:

$$\Gamma_{\eta\to e^+e^-}/\Gamma_{total} = (2.4\pm 0.1)\cdot 10^{-8}$$

1.3 Experimental Results on $\eta \rightarrow e^+e^-$ Decay

The experimental search for this decay started in 1974, when Davis et al. in his work [16] put a limit $BR_{exp} < 3 \cdot 10^{-4}$ *at* $CL = 90\%$ based on $1.2 \cdot 10^4$ sample of η decays.

More recent works from 1996 (White et al. [17]) and 1997 (Browder et al. [18]) where mainly directed to the search for this particular decay channel. In the first one the data were taken at the Saturne η facility using $pd \rightarrow^3 He\eta$ reaction obtaining the total η event sample of $N_\eta = (1.22 \pm 0.01) \cdot 10^9$. The main variable used in the final selection process was the opening angle of electron-positron deviation between the measured value in the spectrometer and the value calculated from full body kinematics. The calculated 90% confidence level upper limit corrected by the uncertainties was $< 2 \cdot 10^{-4}$ based on 9.1 background events in the expected signal area. In the second work data collected by the CLEO II detector at the CESR were used. The η mesons were produced in the e^+e^- collisions with 10 GeV center-of-mass energy. The $\eta \rightarrow e^+e^-$ decay candidates were search in invariant mass of e^+e^- spectrum and $N_{\eta \rightarrow e^+e^-} = 27.1$ event candidates were found and this number leads to 90% confidence upper limit $< 7.7 \cdot 10^{-5}$.

In 2008 also the branching ratio limit $< 2.7 \cdot 10^{-5}$ *at* $CL = 90\%$ were published in [19]. It is worth to mention due to the fact that it used the same detector as in this work but located on CELSIUS storage ring and it was using $pd \rightarrow^3 He\eta$ reaction slightly above to the η meson production threshold at 893 MeV of incident proton projectiles energy. The decay candidates were searched on 2-dim plot of invariant mass of e^+e^- versus the opening angle between electron and positron. The limit was based on $2.41 \cdot 10^5$ eta meson candidates and under the assumption of no event candidates were seen in the area of interest. The obtained values for branching ratios or branching ratio limits are shown in the figure 3.

Decay mode	BR	BR limit 90% CL
1. $\eta \rightarrow e^+e^-e^+e^-$	$(2.7^{+2.1}_{-2.7}{}_{stat} \pm 0.1_{syst}) \times 10^{-5}$	$<9.7 \times 10^{-5}$
2. $\eta \rightarrow \pi^+\pi^-\mu^+\mu^-$	–	$<3.6 \times 10^{-4}$
3. $\eta \rightarrow \mu^+\mu^-\mu^+\mu^-$	–	$<3.6 \times 10^{-4}$
4. $\eta \rightarrow e^+e^-$	–	$<2.7 \times 10^{-5}$
5. $\eta \rightarrow \pi^+\pi^-e^+e^-$	$(4.3^{+2.0}_{-1.6}{}_{stat} \pm 0.4_{syst}) \times 10^{-4}$	–
6. $\eta \rightarrow e^+e^-\mu^+\mu^-$	–	$<1.6 \times 10^{-4}$
7. $\eta \rightarrow e^+e^-\gamma$	$(7.8 \pm 0.5_{stat} \pm 0.8_{syst}) \times 10^{-3}$	–

Figure 3: *The measured branching ratios for different η meson decay channels with lepton-antilepton pair(s) taken from Berłowski et al. [19].*

Today the best upper limit for $\eta \rightarrow e^+e^-$ decay $BR_{exp} < 4.9 \cdot 10^{-6}$ *at* $CL = 90\%$ comes from HADES experiment [20]. It was operated at GSI laboratory and used data from proton-proton collisions at 3.5 GeV kinetic beam energy. Using the invariant mass distribution of

e^+e^- pairs in the range of η meson mass, the experimental data points were fitted using a polynomial background function with the exclusion of some range around eta meson mass. Then using known value of η meson production cross section and upper limit for signal counts the value mentioned above was obtained.

1.4 The $\eta \to e^+e^-$ Decay as a Probe of the New Physics

The pseudoscalar mesons decay into e^+e^- pair became one of the most interesting topics in today low-energy hadron physics, since there is a possible admixture of non-SM processes that can enhance the BR of this decay. The most recent and very precise experimental value of $BR(\pi^\circ \to e^+e^-) = (7.49 \pm 0.29 \pm 0.25) \cdot 10^{-8}$ determined by KTeV collaboration exceeds latest theoretical calculations from Dorokhov and collaborators [13, 21, 11] by 3 standard deviations. The suggestion from Kahn *et al.* [22] is that the possible explanation can be the exchange of an off-shell neutral boson U of mass $m_U \sim (10-100)MeV$. This indication is an extension of previous work originated by Fayet [23, 24]. The U boson was previously proposed by Boehm *et al.* [25, 26, 27, 28] (see also ref.[29]) in the light dark matter models to mediate the annihilation of a neutral scalar dark matter particle χ of (1-10) MeV mass in the reaction $\chi\chi \to e^+e^-$. Such theoretical models can explain the positon/electron excess observed in several experiments [30, 31, 32] by an annihilation of dark matter particles into e^+e^- pairs. This models were also used as an explanation for a 511 keV line observed by INTEGRAL experiment [33] emanating from the center of the Galaxy due to excess of positrons produced in this annihilation process [22].

The possible explanation proposed by Kahn *et al.* [22] in order to explain the mismatch between experimentally obtained value and theory predictions for the branching ratio $BR(\pi^\circ \to e^+e^-)$ is to assume that coupling of the neutral vector meson U to the d and u quark fields of the e^+e^- pair and π° via the axial-vector components g_A^d, g_A^u and g_A^e respectively. For the calculations simplicity, a common axial coupling $g_A \equiv g_A^u - g_A^d \equiv g_A^e$ of the order of $g_A = (2.0 \pm 0.5) \cdot 10^{-4} \cdot m_U/(10\ MeV)$ was fitted. The calculation was based on the model of SM tree-level process $\pi^\circ \to Z^* \to e^+e^-$, where Z boson mass was replaced by by the much lighter mass m_U of the neutral vector meson U and where the weak coupling constant is replaced by g_A. Under the assumption that the octet axial-vector quark-coupling is of the same order as above, the U boson contribution to the branching ratio $BR(\eta \to e^+e^-)$ is about 10^{-9}, which agrees with theoretical calculation by Dorokhov *et al.* [13, 21, 11] and it is much smaller than the experimental bound value $2.7 \cdot 10^{-5}$ obtained by CELSIUS/WASA collaboration [19]. However, using the same fit, the prediction for contribution of order $2.0 \cdot 10^{-5}$ to $BR(\eta \to \mu^+\mu^-)$ is an order of magnitude larger than the experimentally measured value $BR(\eta \to \mu^+\mu^-) \sim (5.7 \pm 0.9) \cdot 10^{-6}$ [34]. The mismatch can by explained in the two ways: either axial-vector coupling of the U meson to the muon is smaller than g_A^e or the octet axial-vector quark coupling is smaller than $g_A^u - g_A^d$.

2 Experiment

The Wide Angle Shower Apparatus (WASA) detector was designed to study production and decays of light mesons. Pions and eta mesons are produced in hadronic interactions between proton beam and small spheres of frozen hydrogen or deuterium coming from integrated into detector setup internal pellet target. It consist of two main parts (see fig.4):
- Forward Detector to measure recoiled and scattered particles;
- Central Detector to study the meson decay products.

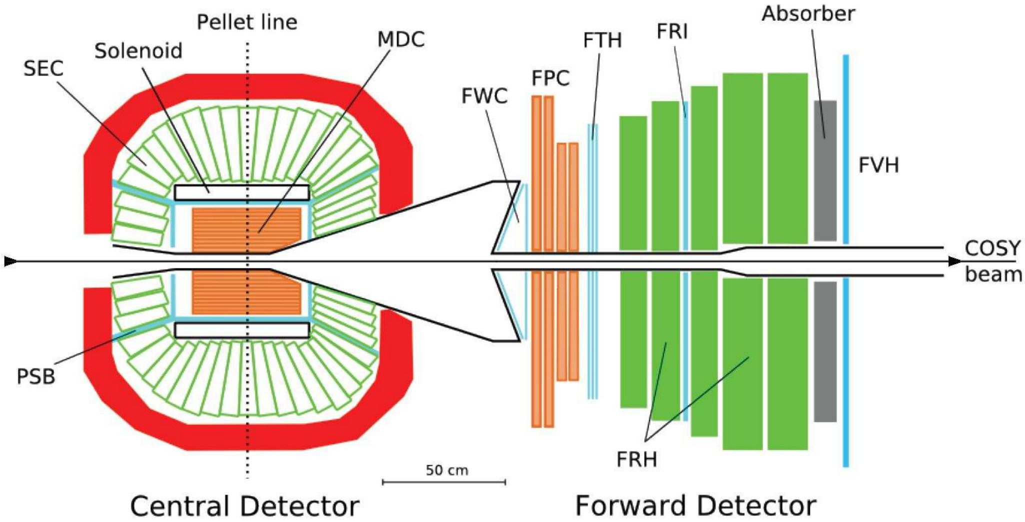

Figure 4: *Overview of the WASA detector.*

The forward part consists of several layers of plastic scintillators and of proportional drift counters. The central part consists of cylindrical drift chamber located in the magnetic field provided by superconducting solenoid, surrounded by a barrel of thin plastic scintillators and finally by an electromagnetic calorimeter of CsI(Na) crystals. This almost 4π setup allows to investigate rare processes with high luminosities in the order of $10^{32}\ cm^{-2}s^{-1}$. Physic program is focused on rare leptonic decays and because of that the detector components were optimized for the detection of dilepton pairs and a minimization of external photon conversion close to interaction region.

The history of WASA detector started with *"Letter of Intent for a research program on elementary particle physics at CELSIUS"* in 1984. In 1987 came the proposal for the detector itself. The setup was tested and developed on CELSIUS beam in The Svedberg Laboratory, Uppsala, Sweden during 1992-1998. In 1999 the 4π setup and internal target system was finally completed and was mounted on the beam. Since then until 2005 data was taken using p+p and p+d reactions with energies up to 1.36 GeV. In 2005 the proposal of moving the WASA detector due to the shutdown of accelerator was accepted. Installation in the COSY synchrotron in Juelich, Germany was successfully accomplished in the fall of 2006 and since the spring of 2007 the WASA detector has been taking data.

2.1 Pellet Target

The pellet target was a very unique installation designed especially for the CELSIUS/WASA experiment [35, 36]. The main parts are shown in fig.5 and the basic characteristics are covered in tab.4. The whole setup is placed on the top of the platform of central detector. It provides a stream of frozen hydrogen or deuterium droplets called pellets. This kind of arrangement is suited for internal target experiments to accomplish both reasonable beam life time (here in order of a few minutes), high luminosities in the order of $10^{32}\ cm^{-2}s^{-1}$ and reduction of the probability for secondary interaction inside the target area. In the setup's heart where pellet generator is located, liquid steam of hydrogen or deuterium is formed into the jet of droplets by a vibrating nozzle and injected into scattering chamber via skimmer where the droplets freeze by evaporation in the pressure and temperature below their triple point. Just before the scattering chamber the stream of pellets is collimated using several tubes and guided by the flow of the carrier gas to the interaction area. Due to the collimation and turbulence the typical rate of pellets is ~ 5000 per second. After the interaction the pellets are deposited in the pellet beam dump, were the pellets are decelerated and stored. The remains of the evaporated pellets is removed by the pumping system located around interaction region.

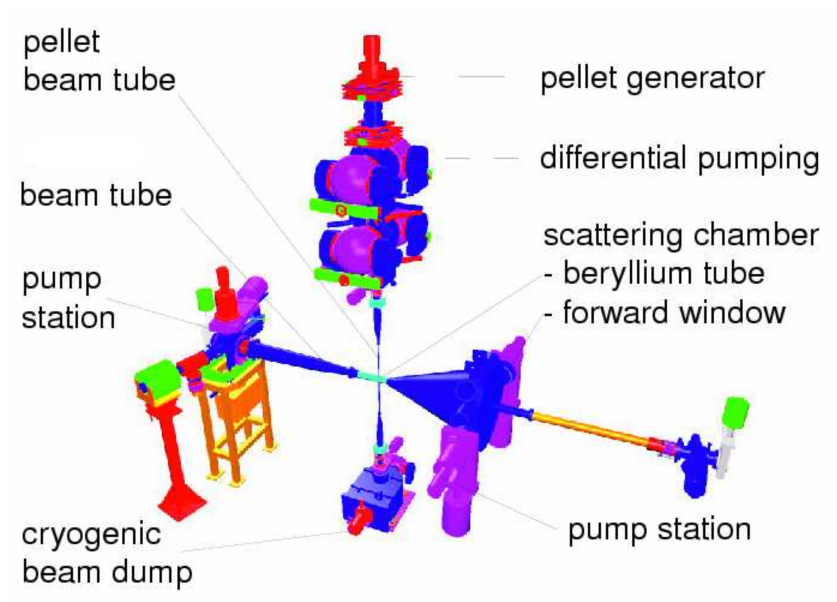

Figure 5: *Overview of the WASA pellet target.*

2.2 Central Detector

The Central Detector surrounds the interaction region inside Scattering Chamber (see fig.4). Mini Drift Chamber (MDC) in the magnetic field of Super Conduction Solenoid (SCS) and Scintillator Electromagnetic Calorimeter (SEC) provides information on energy and momentum of measured charged as well as neutral particles. Plastic Scintillator Barrel (PSB) can be used for detection, identification and discrimination on the trigger level between neutral and charged particle tracks.

2.2.1 Coordinate System

The description of the WASA detector can be done in either cartesian (x, y, z) coordinate system or in spherical (r, θ, ϕ) coordinates. Both are based on a right-handed coordinate system with the origin in the interaction point and z axis defined by the beam direction. The plane transverse to the beam direction defines the $x - y$ plane, where positive x axis is pointing horizontally outwards of the accelerator ring and y axis is pointing vertically upwards. The polar angle θ is measured from the beam (z) axis and the azimuthal angle ϕ is the angle on $x - y$ plane starting from positive x axis.

2.2.2 Scattering Chamber

In order to keep the amount of passive material next to interaction region reduced to minimum the scattering chamber of radius 30 mm made of 1.2 mm beryllium was used (see fig.6). To lower the probability of secondary interactions beryllium was chosen do to the fact that the conversion of photons in the electric field of a nucleus is connected directly to square of the atomic number of the material.

2.2.3 Superconducting Solenoid

The Superconducting Solenoid provides the axial homogeneous magnetic field up to 1.3 T for the measurement of the momenta of the particles tracked by the Mini Drift Chamber. It's cooled down to 4.5° K by using of liquid Helium installation. Presence of magnetic field also protects the whole central detector from low energy Delta electrons produced in the experiment. The wall thickness of the solenoid was minimized to 0.18 radiation lengths to ensure accuracy and sensitivity of energy measurements in the electromagnetic calorimeter. To provide the return path for the magnetic flux whole central detector is enclosed in yoke, made of 5 *tons* of pure iron. The yoke also serves as a shield for photomultipliers from magnetic field. The distribution of magnetic field inside the WASA detector is shown in fig.7 taken from [37].

Property	Value
Pellet diameter	$25 - 35\ \mu m$
Pellet frequency	$\sim 7\ kHz$
Distance between pellets	$9 - 20\ mm$
Effective target thickness	$10^{15}\ atoms/cm^2$
Pellet velocity	$\sim 80\ m/s$

Table 4: The pellet target system main properties.

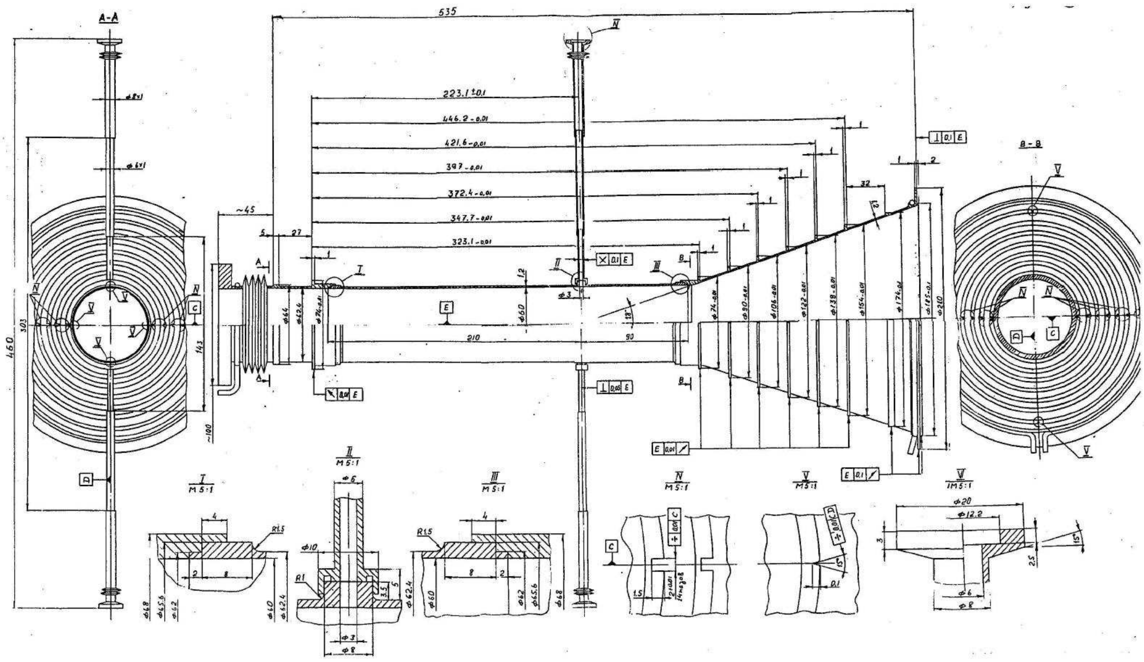

Figure 6: *Beryllium beam pipe and crossing it pellet target tubes.*

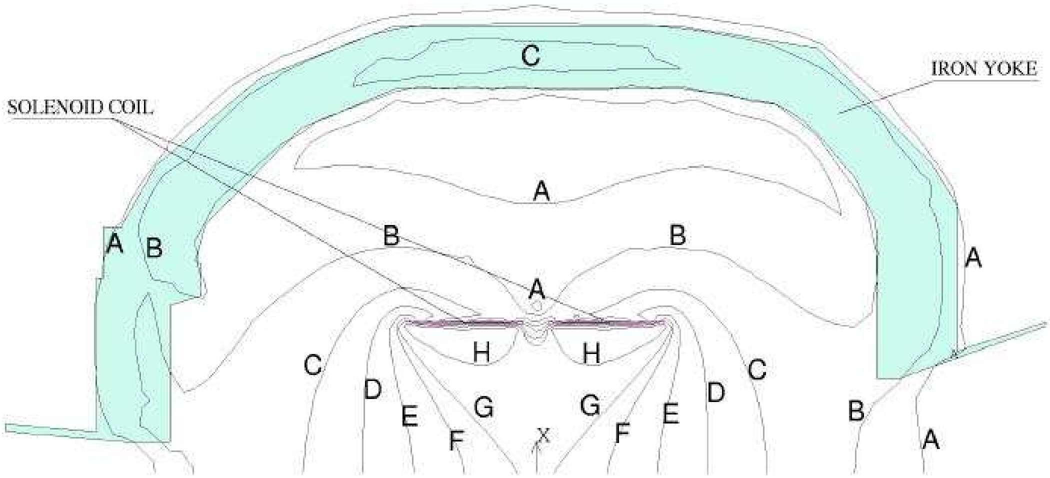

Figure 7: *Magnetic flux density calculated for a coil current of 667 A, which corresponds to the magnetic field of 1.3 T in the interaction region. Contour maxima are indicated by lines marked A-H, where:* $A = 0.10\ T, B = 0.25\ T, C = 0.50\ T, D = 0.75\ T, E = 1.00\ T, F = 1.20\ T, G = 1.30\ T, H = 1.50\ T$.

2.2.4 Mini Drift Chamber

The Mini Drift Chamber (MDC) consists of 1738 tubes (also called straws) made of 25 μm Mylar and filled with a gas mixture consisting of 80% argon and 20% ethane (C_2H_6). In the center of each straw a 20 μm sensing wire made of stainless steel is placed. The tubes are organized into 17 layers with increasing radii - 5 innermost layers include straws of a radius of 2 mm, the next 6 layers - 3 mm and the last 6 layers - 4 mm. In order to determine also z-coordinate of tracks each even layer is skewed by a small angle (4°-6°) with the respect to the beam axis (see fig.8ab). Each layer of tubes is joined and held in place by plates shaped from an aluminum-beryllium alloy (50% Al-50% Be) into semi-rings surrounding the beam pipe. For the mechanical construction purpose the MDC is enclosed in cylindrical cover mode of 1 mm thick Al-Be alloy.

a) b)

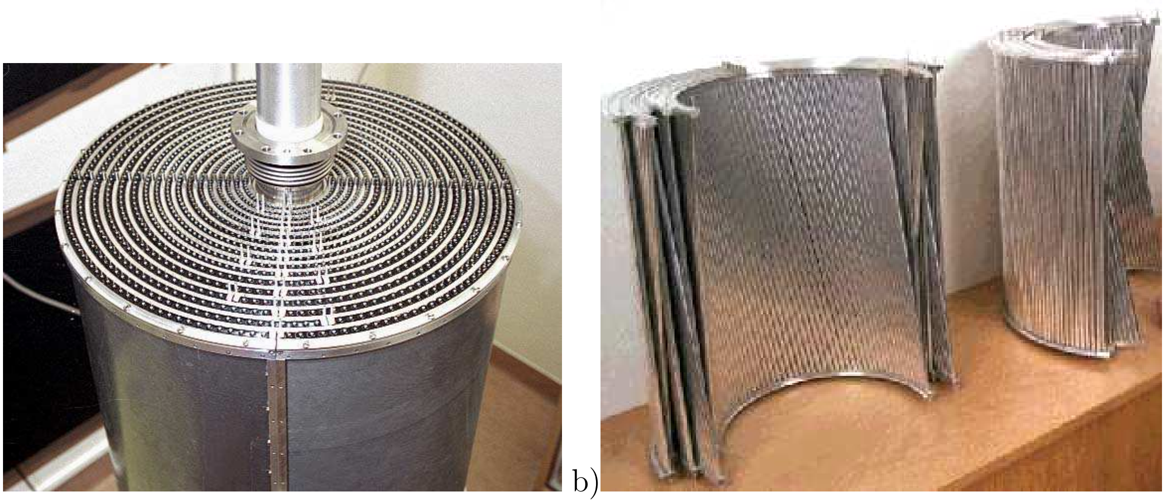

Figure 8: *The Mini Drift Chamber photographs showing: a) layer structure around beam pipe, b) details of separated layers.*

The signal is created by interaction of passing through ionizing particle with the filling gas. Electron-ion pairs from generated ionizing clusters are drifting towards the electrodes due to potential difference created by applying hight voltage to the sensing wire with the respect to outer cylinder. On it's way induced electrons can create even more electrons due to interaction with the gas mixture. In the wire close area the electric field is large enough to produce electron-ion pair cascade and eventually create a signal. By the looking at the shape of the signal and drift time needed for the electrons to reach the anode from the interaction point it is possible to determine the distance of the passing-through particle from the center of the tube in order to reconstruct the track parameters with resolution better the the straw diameter (see fig.9). The track curvature with the value of the magnetic field allows to determine the particle momentum. A more detailed description of the MDC construction and it's operation can be found in [38].

2.2.5 Plastic Scintillator Barrel

The Plastic Scintillator Barrel is placed inside of the solenoid and surrounds Mini Drift Chamber (see fig.10). It consists of central barrel-shaped part and closing it pair of end

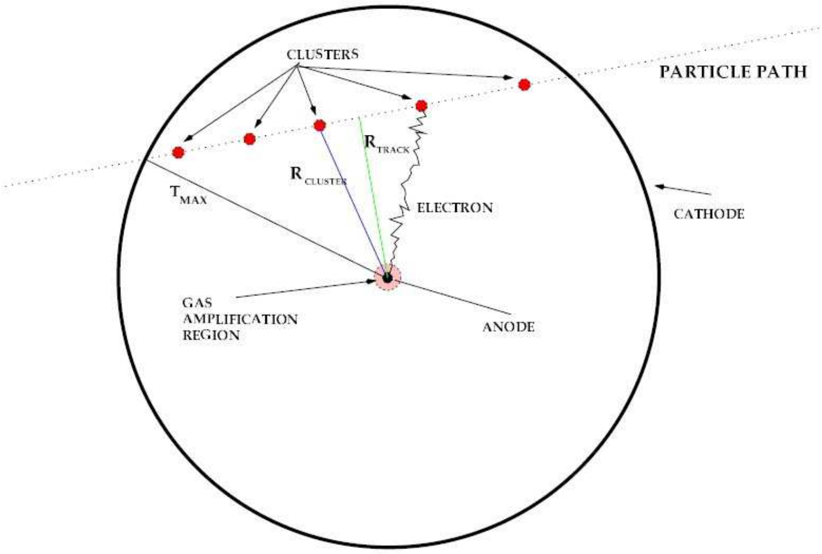

Figure 9: *A schematic view of the ionization process in the straw.*

caps (see fig.11). The central part is build with 50 elements (each of 550 mm long and 38 mm wide) formed into 2 layers with a small (6 mm) overlap between nearby elements. The end caps contain 48 trapezoid-shaped elements in each part formed into circles where front part is flat and backward conical. The elements are shaped in such a way that the edges of each element overlaps with the neighboring one to avoid gaps. Each part is made of 8 mm thick BC-408 plastic scintillator and connected to the readout system by light guides attached to each of 146 elements (see fig.12).

The Plastic Scintillator Barrel is an essential system in trigger logic to distinguish between charged and neutral particles. Also on the level of offline analysis it provides information used for the identification of charged particles. More information about design and performance of the WASA plastic scintillator can be found in [38].

2.2.6 Scintillating Electromagnetic Calorimeter

The Scintillating Electromagnetic Calorimeter consists of 1012 sodium-doped CsI scintillating crystals placed between the solenoid and the iron yoke surrounding all other active parts of the Central Detector (see fig.13). The scattering angles covered by this detector are between 20° and 169° (see fig.14) and this setup allows to cover 96% of 4π decay space. The crystals shape are truncated pyramids and there are arranged in 24 layers. Crystals lengths vary from 30 cm in the central part to 25 cm in the forward and 20 cm in the backward part and corresponds to $\sim$ 16 radiation lengths and $\sim$ 0.8 hadronic interaction lengths. The Calorimeter provides information for measurement of deposited energies and emission angles of both neutral and charged particles. Energy resolution for photons can be described by a formula: $\frac{\delta_E}{E} = \frac{5\%}{\sqrt{E(GeV)}}$ and for stopped charged particles, the energy resolution is $\sim$ 3%, with stopping power of crystals equal to: 190 MeV for pions, 400 MeV for protons and more than 800 MeV for electrons.

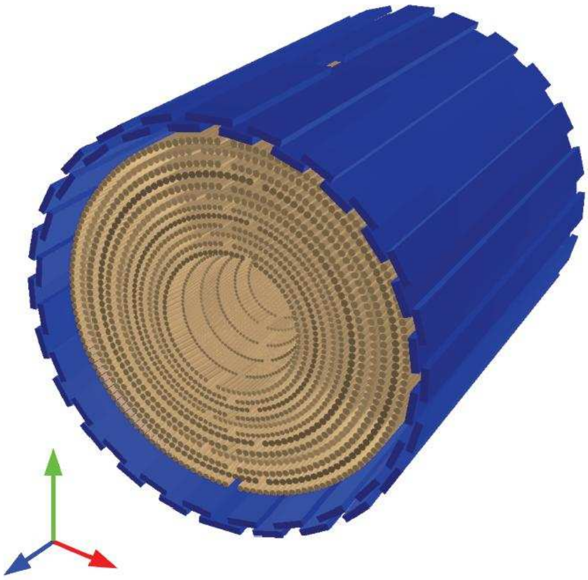

Figure 10: *3D view of the central part of the Plastic Scintillator Barrel (blue) surrounding the Mini Drift Chamber (brown).*

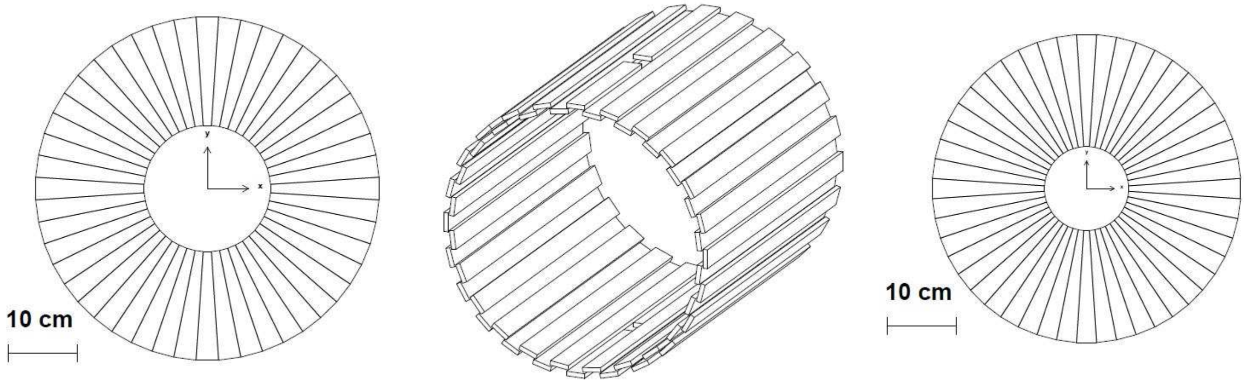

Figure 11: *Forward, central and backward parts of the Plastic Scintillator Barrel.*

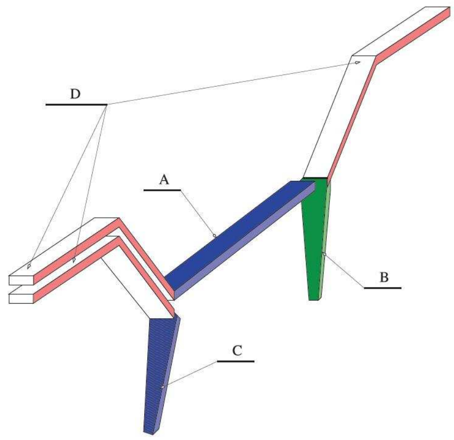

Figure 12: *One full section of the Plastic Scintillator Barrel. A-C denotes individual elements, D light guide connections.*

The Scintillating Electromagnetic Calorimeter and its performance is described in more details in [40]

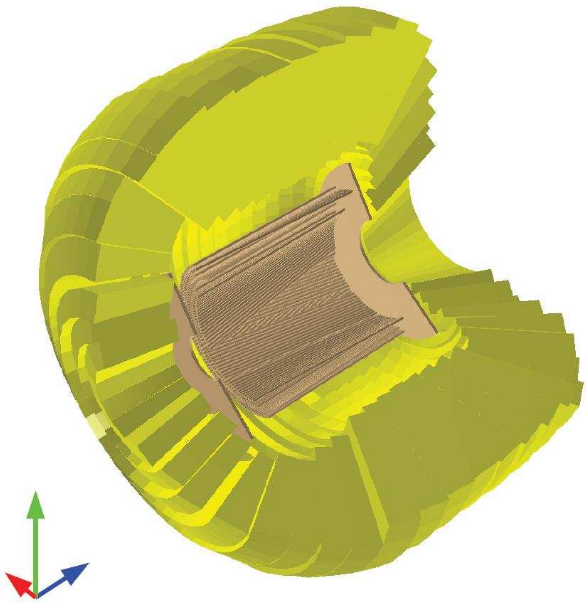

Figure 13: *3D cross section of the Scintillating Electromagnetic Calorimeter (yellow) surrounding the Mini Drift Chamber (brown).*

2.3 Forward Detector

The WASA-at-COSY Forward Detector consists of several plastic detectors for time and energy information and a straw tracker for a measurement of track trajectory angles. Is designed to detect particles between 3 and 18 degrees polar angle and provide a precise information for triggering purpose.

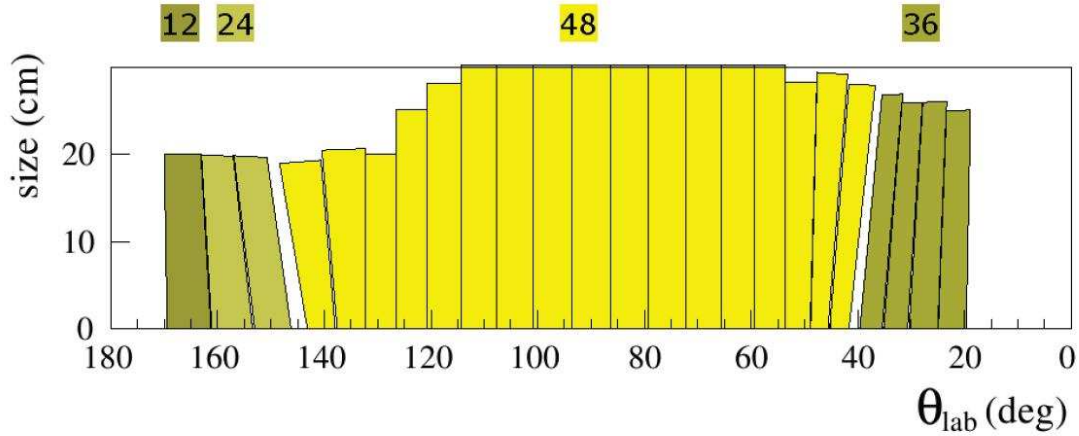

Figure 14: *Polar angle θ coverage of the Scintillating Electromagnetic Calorimeter in the function of individual crystal length. The numbers on the top of the picture show amount of elements in each of 24 calorimeter rings.*

The main part of Forward Detector with the most active material is Forward Range Hodoscope (FRH), consisting of five layers of each of 24 pie-shaped detectors (see fig.15). The first three layers are made of 110 mm thick plastic scintillator while the last two have a thickness of 150 mm. It is used for the determination of the kinetic energy via the energy deposit of particle in it. The total stopping power for protons is 360 MeV and the stopping power for ^3He ions is 1 GeV.

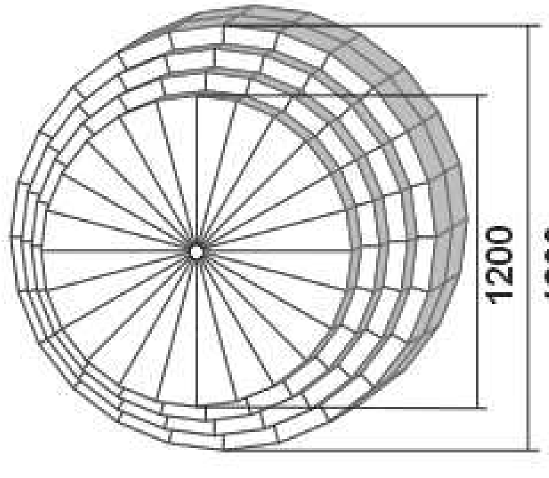

Figure 15: *Schematic view of Forward Range Hodoscope. Diameters of each layer are shown in mm.*

To have precise information about particle track and in order to identify particle three thin plastic detectors are placed in the front of FRH. The Forward Trigger Hodoscope consists of three layers of 5 mm plastic scintillator. The first layer contains 48 pie-shaped elements and the following two layers are each contain of oppositely oriented Archimedian shaped elements. The fig.16 shows the idealized procedure of determination of passing particles both polar and azimuthal angles. This unique geometry plays an important role on the trigger level. This detector is also used for a precise time information and moreover combination of both FRH and FTH allows to use offline identification of particles.

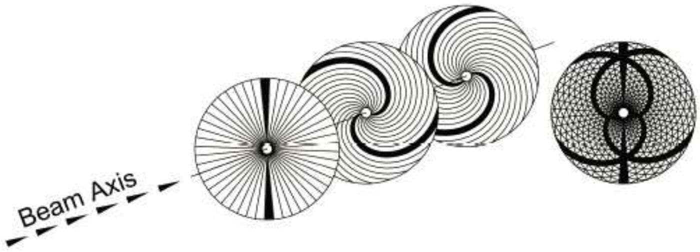

Figure 16: *Schematic view of Forward Trigger Hodoscope with the example of hits from two particles marked in black. Joining information from all three layers allows to determine both polar and azimuthal angles of passing particles.*

The most precise information about angles of forward-scattered particles are provided by the Forward Proportional Chamber (FPC). It is made of four modules divided into four layers. Each layer contains 122 aluminized 8 mm mylar tubes (called also straws). The first and the third layers are shifted with respect to the second and fourth to improve the resolution (see fig.17). The working principle of straw tubes is almost the same as described before for MDC in section 2.2.4. The FPC provides about a factor of two improvement on the azimuthal and polar angles of the reconstructed particle compared to using only the FTH pixel ([42]). Coincidence between the pixel in the FTH and a track from the FPC also helps to filter out particles not coming from the interaction region and improves the azimuthal and polar angles determination of the reconstructed tracks as compared to using only FTH information.

The Forward Window Counter (FWC) is the first detector of the FD along the beam direction. It consists of two layers of 3 mm thick plastic scintillators shaped into 24 pie-looking elements. The elements of both layers are shifted half an element with respect to each other in order to provide two times better azimuthal angular effective granularity (see fig.18). Online this detector serves as multiplicity counter and offline provides information for particle identification.

2.4 The Light Pulser System

In order to monitor the transmitted gain of individual scintillation counters during the experiment the light pulses via light fibers are used. Since the two types of scintillators are used also two different light sources were designed. A xenon flash tube is used for the CsI(Na) elements of the calorimeter and three LED-based light sources for all plastic scintillators. The light pulser signals are monitored directly via photodiodes and serve as reference signals used in the offline analysis to correct for changes in the gain. More detailed description can be found in [39].

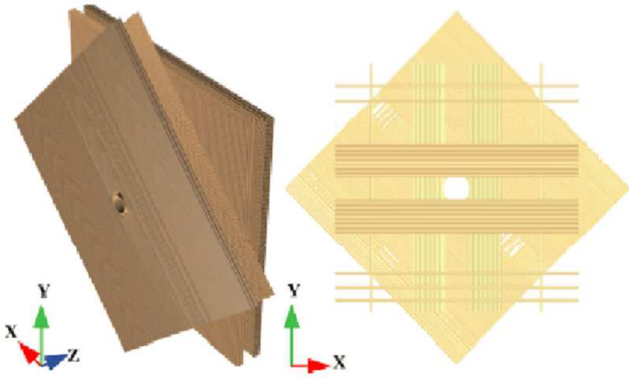

Figure 17: *Schematic view of Forward Proportional Chamber in order to illustrate its orientation.*

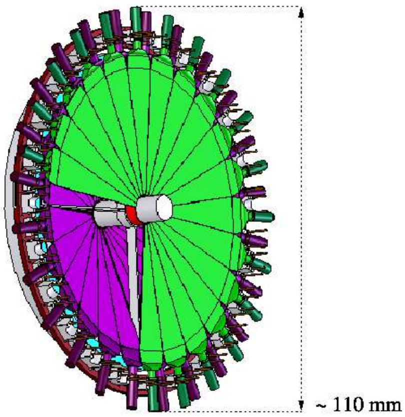

Figure 18: *Schematic view of Forward Window Counter with some elements removed to see its structure.*

2.5 Data Acquisition

In order to collect information from different detectors providing variety of signals, several specialized digitization modules are used in WASA-at-COSY experiment. Those modules use a self-triggering mode to digitalize and store internally the signals from corresponding detectors. When the trigger signal is invoked the information from modules is extracted and written with time stamp of each detector response. A schematic picture of the DAQ is shown in fig.19 and more information can be found in [41].

For the crystal scintillation detectors, signals are extracted via photomultipliers, propagated into splitter boxes and from there send through discriminators into trigger system and charge-to-digital-converters (QDCs). Continuously analog signals are sampled by analog-to-digital-chips (ADCs). Due to the fact that electromagnetic showers can spread along many crystals the electromagnetic calorimeter is divided into groups of crystals within which energy sum is collected. Two different methods for QDC signal shaping can be used - one is so called "fixed gate" and the second mode is named "floating gate". The difference between those two is that the fixed gate integrates the signal for a certain amount of time starting from a given trigger time and the following looks for a signal inside a certain time window defined by a pulse-searching algorithm. The rising edge of signal provides also the signal time. Within QDC modules also base line subtraction is automatically performed.

Plastic scintillators produce a significantly shorter signals and after ADC conversion they must be stretched via a signal shaper before integration in QDCs to determine energy and sending to trigger system via leading edge discriminator to provide time information as a logical signal as an output.

As for straw detectors of MDC and FPC the signals are amplified, sent to the discriminators and output from there is collected by time-to-digital-converters (TDCs).

The introduced system can provide event rates of 10 Hz for a typical event size of 8 kB ([42]). The limiting factors are event size and the speed of writing to disk which lead to dead time of 20 μs per event. During experiment data are stored in RAID (Redundant Array of Independent Disks) arrays which are for practical purposes were divided into 20 GB files called runs.

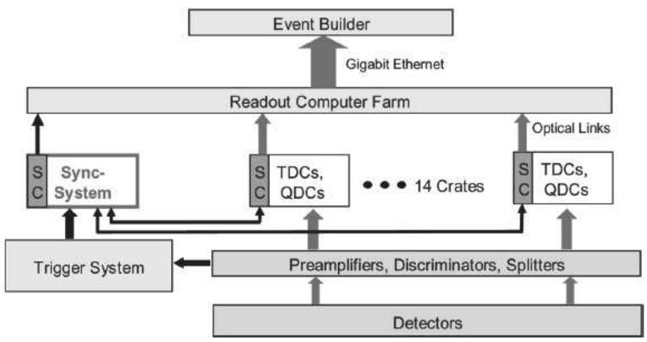

Figure 19: *The data acquisition system used in WASA-at-COSY experiment.*

2.6 Trigger System

In order to reduce the initial amount of data collected with the pellet count rates more then 5000 per second and luminosities up to 10^{32} $cm^{-2}s^{-1}$ a kind of trigger system is needed (see fig.20). It allows to focus on only interesting from the experiment point of view events. Trigger logic makes a decision about discarding or saving particular event based on the information about hit multiplicities, individual detector matching, energy deposits in selective detectors, cluster multiplicity and time coincidences. In order to provide the information on the track charge, the signals from the electromagnetic calorimeter are matched with signals from the plastic scintillator elements using timing information and geometrical overlapping of plastic scintillators with the crystals' clusters. In between, two energy thresholds (high and low) are applied to give logic signals for both energy settings. To provide information on the total energy deposited in the electromagnetic calorimeter or in its subsections (e.g. its halves), the analog signals are summed. If the analog signal sum is greater than a set up threshold the logical signal of certain length from discriminators is formed. This signal is combined with the other signals from another detectors and if all of them are matching the event is saved.

To form more sophisticated trigger conditions, the initial trigger signals can be combined in coincidence matrix, allowing to use up to 32 different coincidence conditions. Those 32 conditions can be furthermore prescaled to allow high rate triggers be present in the data stream. The mask and logical "AND" and "OR" units finally start the readout (the logic units were developed at Uppsala University for the CELSIUS/WASA experiment [43]). The information about trigger logic, trigger rates and prescaling factors are saved into data stream to allow offline analysis of for example trigger efficiencies or to check which trigger started the data acquisition.

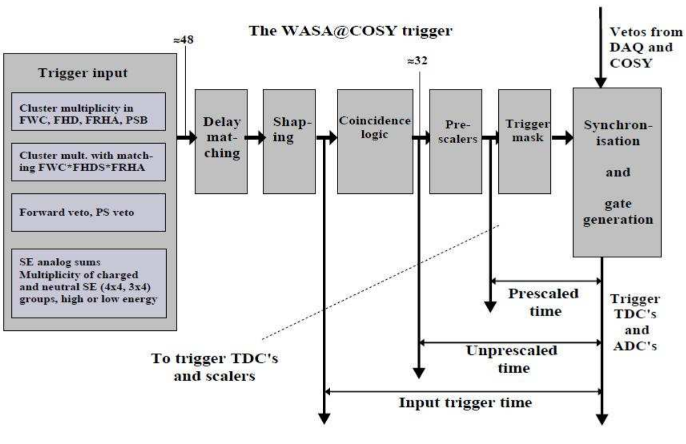

Figure 20: *The trigger system used in WASA-at-COSY experiment.*

3 Analysis

3.1 Software Tools

In order to analyze experimental data a specialized software have been used. To decode and interpret the detector response we used Root Sorter analysis software which allows to reconstruct tracks from the information obtained from the individual detectors. For computer simulations of the detector response Monte Carlo methods were used. It was done in the two step process: first the decay physics were generated using a event generator and on the next step the detector response were simulated with a WASA Monte Carlo package. Analysis were performed using ROOT data analysis framework [46, 47]. The typical analysis chain of data and Monte carlo simulation is shown in fig.21.

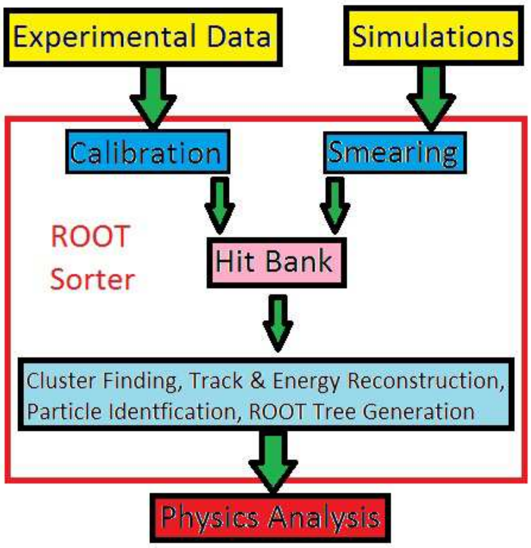

Figure 21: *Flow chart of the analysis chain.*

3.1.1 Monte Carlo Generation

Two different methods for simulations of various decay reactions were used. The first and simpler one were using the build-in Phase Space generator into ROOT software package, called TGenPhaseSpace. The second method used is completely based on ROOT, originally developed for HADES Collaboration in GSI and called Pluto event generator [44, 45]. It is a simulation framework for heavy ion and hadronic-physics reactions in the energy regime up to a few GeV. It is based on C++ code implemented into ROOT environment. Pluto phase-space generation software is based on GENBOD procedures taken from the CERN-LIB package [48]. It allows in the simple manner to choose the reaction of interest, set the properties of beam and target and choose if the user wants to use more sophisticated physics models of production and particle decays. In the output of both generators the four-momentum vectors are created for all the final state particles produced in the reaction. This output serves as input for the simulation of the detector response. The part of simulations presented in this work is based on the v5.35 version of the PLUTO package within ROOT v5.26 environment. The same version of ROOT package have been used for ROOT build-in Phase Space generator.

3.1.2 WASA Monte Carlo Detector Simulation

The WASA Monte Carlo package (WMC) was created based on GEANT3 package developed in CERN [49, 50]. It simulates the propagation of particles through the WASA detector. Full description of the detector was implemented including position, dimensions, material type of each of its components. The software is responsible for the interaction of passing through particles with the active or passive detector elements. The map of magnetic field is implemented as well as particle decays, hadronic interactions and secondary effects like external conversion. In order to have similar resolution in both Monte Carlo simulations and data the smearing parameters are introduced. As an input for simulation WMC takes the output files from the generation. As an output it provides a special file containing responses of all the WASA detectors that interacted in the simulated event. Moreover this file contains the initial values of parameters (including the four-momentum vectors) used for the simulation which is very crucial in understanding the detector response for a certain criteria and obtaining the reconstruction efficiency. On the other hand there are couple of effects that are not implemented in the simulation software. The most noticeable are: trigger response simulations, electronic noise and chance coincidence events (so-called pileups).

3.1.3 Root Sorter Reconstruction Framework

Root Sorter analysis environment is base on ROOT data analysis framework [51]. It was developed to carry online as well as offline data analysis. Originally, it was developed for the ANKE experiment at COSY synchrotron and later, it was rewritten for the purpose of the WASA experiment. It has a modular structure i.e. detector information decoding and track reconstruction are carried in the individual modules in such a way that high level modules are automatically calling the necessary low level modules. This kind of structure and working principle allows to use only parts of Root Sorter code as may be required and add user code without any changes in the ongoing one.

The decoded data are at first stored in the raw hit bank based on energy and time information decoded from the individual detectors. After calibration there are copied to the hit bank. In the case of Monte Carlo simulations the working flow is a little bit different, because the raw Monte Carlo data is at first stored in its own hit bank and after smearing copied to the normal hit bank. The smearing step is necessary in order to match the simulated and real data resolution of the WASA detector. From this point the analysis of Monte Carlo simulation and data is the same. The hits from each subdetector element that derive from the same particles are merged into clusters and stored in the cluster bank. Next the track finding routine is invoked which connects the clusters from different detectors, merge them into tracks and store them in the track bank. It is worth to mention that cluster and track finding algorithms differ depending on the subdetectors.

3.2 Track Reconstruction

The track reconstruction procedure for the most of the WASA experimental setup detectors consists of the following two steps:

- hits in each detector are merged into clusters by checking the geometrical overlap or neighborhood of particular hit element and its timing. In this step the deposited energy is summed and the mean time is calculated. The cluster finding algorithm starts with the element with the locally highest energy deposit and iteratively adds all neighboring elements.

- Clusters are merged into tracks using predefined allowed time windows and angular overlapping.

For specific detectors the tracks can consist of only one cluster, for example Central Detector neutral tracks that consist of information only from Electromagnetic Calorimeter. For the Forward Detector different track candidates can share the same cluster.

The outcome of tracking procedure is four different class of tracks:
FDC - Forward Detector Charged tracks, consisting of at least one cluster in one of thin forward detector scintillators
FDN - Forward Detector Neutral tracks, containing of no clusters in one of thin forward detector scintillators, but with cluster in the Forward Range Hodoscope
CDC - Central Detector Charged tracks, tracks with either Plastic Scintillator or Mini Drift Chamber information
CDN - Central Detector Neutral tracks, consisting of only a single cluster in the Electromagnetic Calorimeter

3.2.1 Forward Detector

The track finding algorithm for Forward Detector is based on geometrical overlapping between different layers forming this detector. The routine starts with pixel pattern found in the 3 layers of Forward Trigger Hodoscope, as shown in fig.16. This set of clusters provides a starting values for θ and ϕ angles, when we assume that the particle was produced in the interaction point of beam and target located at the center of coordinate system. Next this values are used to search for overlapping clusters in different forward detectors. To provide the more precise angular information the initial angular values are compared to the hits in the Forward Proportional Chamber (shown in fig.17) to adjust them if necessary and improve them in general by at least a factor of 2. For this the purpose the positions of sense wires in FPC are used. At the end of track finding algorithm the cluster information from other forward detectors is added to the track. This step requires the minimum energy deposited in the particular detector and it is using the angular overlapping and time differences between different detectors.

In order to describe the process of charged particle traveling through matter and reconstruct its energy via the energy losses in the specific forward detector layers the Bethe-Bloch formula is used. It describes the average energy loss per unit length as shown in equation 7 [3]. For a particle with speed v, charge z, and energy E, traveling a distance x into a target of atomic number Z and mean excitation potential I, the relativistic version of the formula is proportional to:

$$-\frac{dE}{dx} \sim Z\rho\frac{z^2}{\beta^2}\left[ln\left(\frac{2m_e c^2\beta^2}{I(1-\beta^2)}\right)-\beta^2\right], \tag{7}$$

where m_e is the electron mass, ρ is the density of the target material, c is speed of light and $\beta = \frac{v}{c}$. This formula is valid for massive particles like protons and charged pions but for electrons the recoil effects are more significant, so the modified version of equation 7 is used. In order to apply this relation for kinetic energy reconstruction the offline tables were generated. This tables cover energy loss patterns for a specific particle with a known scattering angle and kinetic energy. The plot of kinetic energy dependance as a function of deposited energy is shown in fig.22a for a simulation of $pp \to pp\eta$. The visible steps on

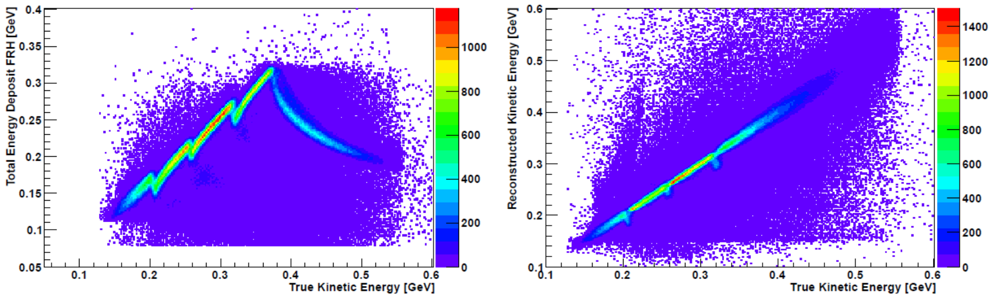

Figure 22: *Relationship between true kinetic energy and energy deposited in the FRH for simulated protons from the reaction $pp \to pp\eta$ (a). True versus reconstructed kinetic energy for the same simulated reaction (b).*

the left hand side of the plot correspond to protons stopping in a certain layer of Forward Range Hodoscope. The fifth layer of FRH is not visible due to the fact that particles passing through the whole detector are indistinguishable from the ones stopping in the last layer of FRH. Protons with energy above 360 MeV pass through the whole detector and this effect is visible as curved line in the right hand side of the fig.22. Fig. 22b illustrates the true value of kinetic energy known from the simulations plotted against reconstructed kinetic energy for $pp \to pp\eta$ generated events. The holes in this spectrum are due to the protons stopping in the inactive material of the detector and were treated in the analysis as stopped in the previous layer of FRH. The background visible in both plots is connected to nuclear interactions of the protons.

For the purpose of the analysis all charged tracks in the forward detector were treated as protons.

3.2.2 Central Detector

Mini Drift Chamber

Mini Drift Chamber (MDC) used in WASA detector is a cylindrical straw chamber in which the better resolution of hit position than the position of wires is achieved using the drift time measurement (see 2.2.4). The collected drift time spectra parametrization converts it to the drift distance which is the radius of closest approach of the ionizing particle with respect to the anode wire. The parametrization depends on a straw position, drift gas mixture, electric field applied between the anode wire and the tube cylinder and magnetic field strength and direction. In addition for the conversion between drift distance and drift time we need to know the drift velocity of electrons in the gas inside the tube and the mean time between collisions of the drifting electrons. The initial time information is derived from fast plastic scintillators surrounding the MDC. In order to reconstruct particle momentum and its scattering angle the information from the MDC detector is used. The implemented algorithm uses pattern recognition by invoking the global fit to all hits in the MDC. The pattern recognition procedure assumes constant magnetic field along the z (beam) axis in which charged particles' tracks should take a form of helices. In the projection to the XY plane the tracks are represented as circles. The parameters of tracks in such a representation are as follows:

- R - radius of a track on the XY plane connected to its momentum
- $R_\circ$ - distance of the center of a tracks circle on the XY plane to the origin of the coordinate system
- $\phi_\circ$ - the azimuthal angle between OX axis and straight line crossing the origin of the coordinate system and the center of a tracks circle
- θ - helix's dip angle which indicates the inclination of the tracks tangent line in the respect to the XY plane
- $z_\circ$ - z coordinate of the track in the point of closest approach between the origin of the coordinate system and track on the XY plane
- Q - the charge of the particle

The parameters are visualized in fig.23.

If we define r as a distance from the origin of the coordinate system to a tracks point and ϕ as azimuthal angle of the track we can describe the so-called ,,half-helix" which is a part of the helix from its closest point to its most distant point with respect to the z axis by a following equations [38]:

$$z = z_\circ + \frac{R}{tan(\theta)} arccos\left(\frac{R_\circ^2 + R^2 - r^2}{2R_\circ R}\right) \tag{8}$$

$$\phi = \phi_\circ + Q \cdot arccos\left(\frac{R_\circ^2 - R^2 + r^2}{2R_\circ r}\right) \tag{9}$$

$$l = R \cdot arccos\left(\frac{R_\circ^2 + R^2 - r^2}{2R_\circ R}\right) \tag{10}$$

The plot of helix's z coordinate against the curvature length, l is a straight line.

The track reconstruction procedure is divided into two consecutive parts called ,,XY-plane procedure" and ,,Z procedure". The track parameters R, $R_\circ$, $\phi_\circ$, and Q are calculated during the first one and $\phi_\circ$ and θ during the former using the information from inclined layers

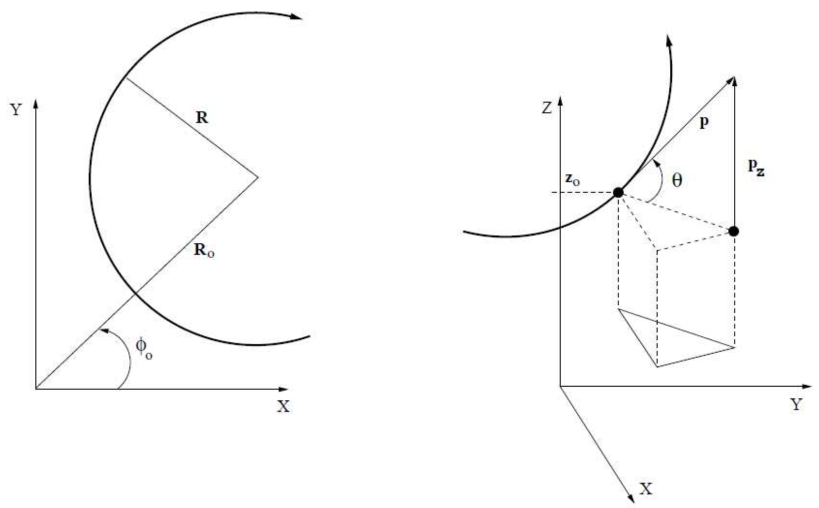

Figure 23: *Helix parametrization used for Mini Drift Chamber track reconstruction.*

of tubes. After the both routines the track parameters are converted into the momentum vector using the average value of magnetic field along the track, its curvature (R) and scattering angles (θ and ϕ). More information about reconstruction algorithm can be found in [52]. The efficiency of MDC track reconstruction using this algorithm is better than 90% for charged track of energy 50 MeV or greater excluding very high or very low θ angles when the number of hit tubes is insufficient for the proper track reconstruction.

Figure 24 shows the event display for a reconstructed event with four charged tracks in the central detector. The lines represent the reconstructed tracks in the MDC, black bars hits in PSB and pink areas the projection of the hit SEC elements (the size of the crystals and the radial position of their front faces are not in scale).

Plastic Scintillator Barrel

The Plastic Scintillator Barrel (PSB) is a set of detectors used for deriving precise time information about charged particles. It is also used as a veto for the neutral ones. It surrounds the Mini Drift Chamber in order to combine the information from both detectors. The central part of PSB consists of overlapping elements to increase the detection efficiency and provide better granularity for the azimuthal angle determination. The hits in specific scintillator element are merged using well defined overlapping regions. The merging procedure checks if the hits are satisfying the minimum requirement of deposited energy greater than 0.5 MeV and the time difference between the hits less than 10 ns. If so, the time information is set to an average from individual hits and energy deposit is assigned from a hit in a cluster with the greatest energy deposit.

Electromagnetic Calorimeter

Due to the fact that electromagnetic showers in the Electromagnetic Calorimeter (SEC) frequently is larger than the size of individual crystal the hits here are combined into clusters according to their position, relative time information and energy deposit. Starting from the

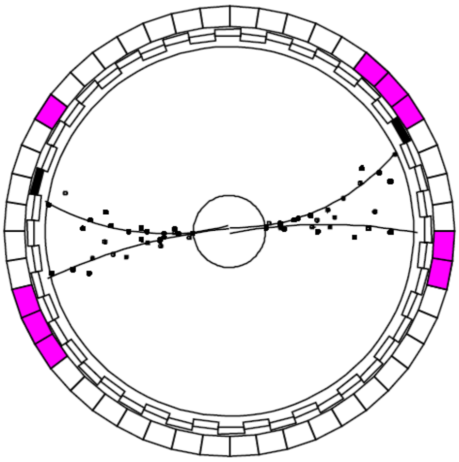

Figure 24: *Event display for a reconstructed event with four charged tracks in the central detector. For more information please refer to the text. Picture taken from Berłowski et al. [19].*

crystal with the highest energy deposit of minimum 5 MeV the merging procedure searches for the neighboring hit with a time difference less than 50 ns and minimum energy of 5 MeV. This hit is added to the cluster if not already belonging to another cluster. This algorithm is then started from the next crystal. The position of cluster is calculated as the energy weighted mean of the contributing crystals response. After constructing the cluster the whole routine is started again for the next highest energy hit not yet merged into any of clusters. In the analysis to reject the electronic noise only clusters of energy more than 20 MeV were considered.

3.3 Trigger Evaluation

In order to reduce the data flow written to disk and select only events with desired signature a trigger system was used. In the experiment data were collected with a certain set of triggers. These were among other: the minimum bias trigger, ,,neutral trigger", ,,charged trigger", and so called ,,energy trigger".

3.3.1 Trigger Concept

The trigger used in this work was designed and developed especially for electromagnetic decays of η meson and in principle it should accept only event where we observe high energy deposits in the both sides of the central part of electromagnetic calorimeter. The energy deposit in one half of electromagnetic calorimeter as a function of the deposit in the other one is shown in fig.25 for the simulation of $\eta \to \gamma\gamma$ decay channel. In fig.26 the schematic view of the electromagnetic calorimeter is shown. Its central part is denoted in white. The division plane contains the beam direction vector and y vector defined in the right-handed coordinate system with the origin in the interaction point and z axis defined by the beam direction. This type of trigger should treat in the similar manner electromagnetic decays of the eta meson like: $\eta \rightarrow \gamma\gamma$, $\eta \rightarrow e^+e^-\gamma$, $\eta \rightarrow e^+e^-$, $\eta \rightarrow e^+e^-e^+e^-$. It is true for the small masses of the virtual photon(s) in single and double Dalitz decays and due to the similar response in electromagnetic calorimeter for both electrons and photons. For the technical details of this trigger construction see section 2.6.

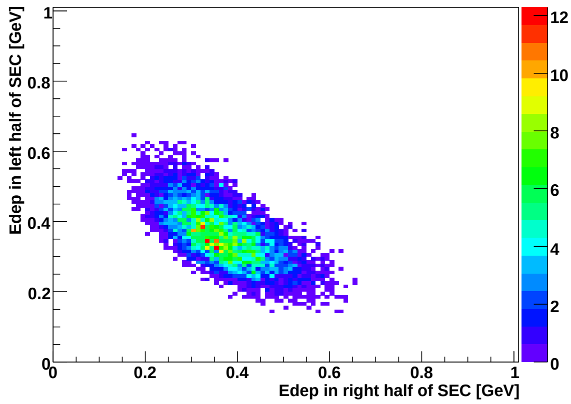

Figure 25: *Energy deposit in one half of electromagnetic calorimeter as a function of the deposit in the other one for $\eta \rightarrow \gamma\gamma$ simulation.*

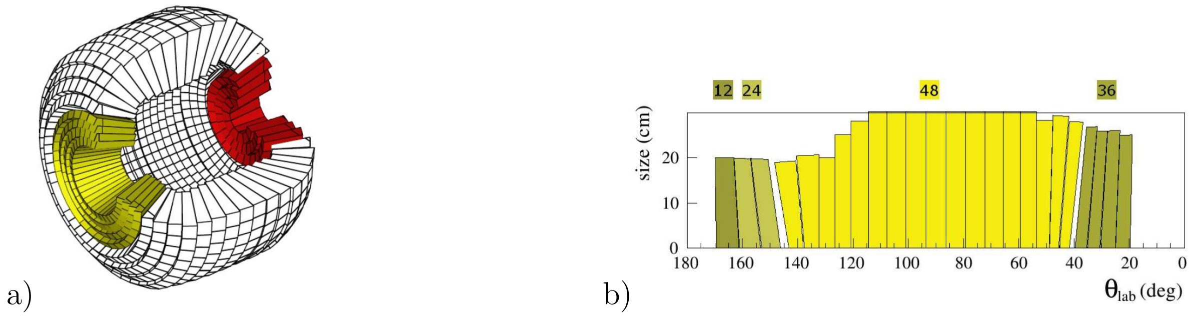

Figure 26: *a) 3D cross section of the Scintillating Electromagnetic Calorimeter. The backward parts and forward parts are colored in red and yellow respectively. b) Polar angle θ coverage of the Scintillating Electromagnetic Calorimeter in the function of individual crystal length. The numbers above the picture show amount of elements in each of 24 calorimeter rings.*

3.3.2 Trigger Definition in the Experiment

The main trigger selected and used in this work was so called ,,energy trigger". In the experiment it has number 10 in the hardware trigger table. The definition of trigger, which have been used during the whole run period was:

[fhdwr2 & frhb2 & Vfvh1 & ecrl],

where the & sign here means logical conjunction between the individual conditions, three first acronyms are the conditions for protons going into forward detector when η meson is produced:
fhdwr2 - track matching (coincidence of modules in the ϕ angle) between Forward Trigger Hodoscope, Forward Window Counter and Forward Range Hodoscope, at least matching tracks, low threshold of Forward Window Counter used. More information on matching trigger can be found in Ref.[53];
frhb2 - at least 2 hits in the second layer of Forward Range Hodoscope;
Vfvh1 - veto condition on the Forward Veto Hodoscope.
The forth abbreviation (**ecrl**) stands for high energy deposit in central part of the central detector in both sides of the Electromagnetic Calorimeter.

In the analysis two other triggers were used: ,,neutral trigger" (trigger number 26) and ,,charged trigger" (trigger number 30). The definitions of those triggers were: [fhdwr2 & frhb2 & Vfvh1 & seln2 & Vps1] and [fhdwr2 & frhb2 & Vfvh1 & ps2 & sel1] respectively, where:
seln2 - at least 2 neutral clusters in the Electromagnetic Calorimeter, where neutral cluster is defined as having no geometrical overlapping with hits in the Plastic Scintillator Barrel;
Vps1 - veto condition on the Plastic Scintillator Barrel;
ps2 - at least 2 hits in the Plastic Scintillator Barrel;
sel1 - at least one cluster in the Electromagnetic Calorimeter, this cluster can be both neutral or charged.

During the whole experiment the triggers mentioned above were unprescaled.

3.3.3 The Energy Trigger Effects

The influence of the trigger conditions on the collected data sample is shown by comparing Monte Carlo simulations and data for the $\eta \to \gamma\gamma$ decay channel. Since the only part of electromagnetic calorimeter connected to the trigger system was the cental part we shouldn't have any particles in the θ angular range outside $(40^\circ - 140^\circ)$ interval. In fig.27a the distribution of θ angle for $\eta \to \gamma\gamma$ decay candidates is shown, the trigger cut line at 40° is clearly seen. Due to the fact that the trigger request high energy deposit in the both halves of electromagnetic calorimeter also the drop of effectiveness of particle detection in ϕ angular range around the points where two halves of calorimeter meet is seen. The effect is shown in fig.27b.

3.3.4 Hardware Signals from the Energy Trigger

The natural way to check the trigger response is to take a look at the hardware signals coming from the trigger for each half of the central part of electromagnetic calorimeter. Those signals should be available at the level of data analysis but unfortunately the corresponding information in the data set was found to be uncorrelated with the energy deposits in the respective half of the electromagnetic calorimeter. Such behavior contradicts the expectation. It means that we have no access to the true values of signals in the analyzed data set.

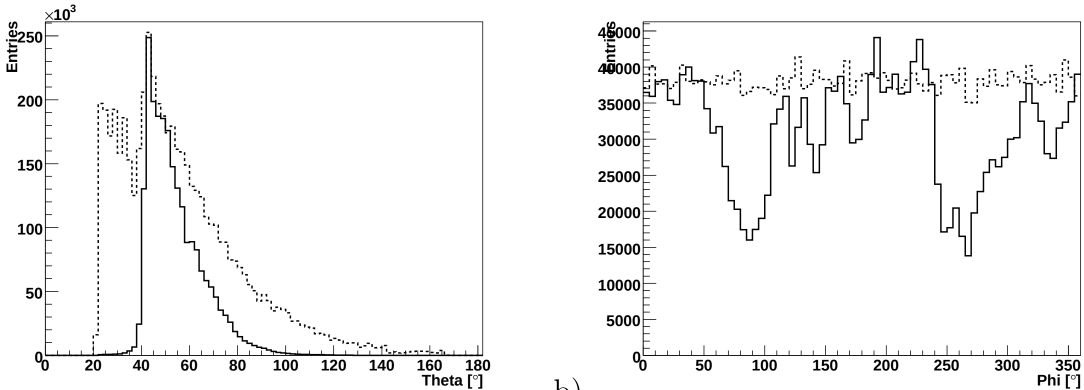

a) b)

Figure 27: *Photon θ (a) and ϕ (b) angle distribution for $\eta \to \gamma\gamma$ decay candidates in Monte Carlo simulation without the trigger condition (dashed line) and data (solid line). Monte Carlo simulations were normalized to data.*

3.3.5 Efficiency of the Energy Trigger

In order to estimate efficiency of energy trigger the data collected with energy trigger and two more generic triggers were compared. Two channels were selected: for $\eta \to \gamma\gamma$ reaction ,,neutral trigger" (number 26) were chosen for comparison and for $\eta \to e^+e^-\gamma$ reaction event tagged with ,,charged trigger" (number 30) were selected. For both channels collected events with corresponding triggers were analyzed the same way as for "energy trigger". The plots in fig.28 show invariant mass spectra (histogram) with gaussian fit to the signal (blue) and polynomial fit to the background (green). The solid red line indicates the sum of signal and background functions. For efficiency calculations the following equation were used:

$$Eff_{tr10} = N_{tr10\&trX}/N_{trX}, \tag{11}$$

where letter N stands for number of events in the signal using the condition that event was tagged with a specific trigger number(s). In the fig.28 the corresponding plots used for efficiency calculations are shown. Each set of pictures contains the invariant mass of two neutral clusters (a) or invariant mass of $e^+e^-\gamma$ (b) for three different triggers (energy trigger - TR10, neutral trigger - TR26, charged trigger - TR30). Each histogram was fitted with a gaussian distribution over a polynomial background, and the number of events comes from the gaussian signal content. The efficiency of the ,,energy trigger" were found to be very similar in both cases and equal to $\sim 70\%$.

3.3.6 Threshold of the Energy Trigger

The distributions of energy deposits in either half of electromagnetic calorimeter are shown in fig.29 for events tagged with energy trigger and without it. By dividing those two distributions one can evaluate a trigger efficiency function for the energy deposit in the half of electromagnetic calorimeter. The following fit function was used:

$$\frac{A}{1 + B * exp(-C * x^2)}, \tag{12}$$

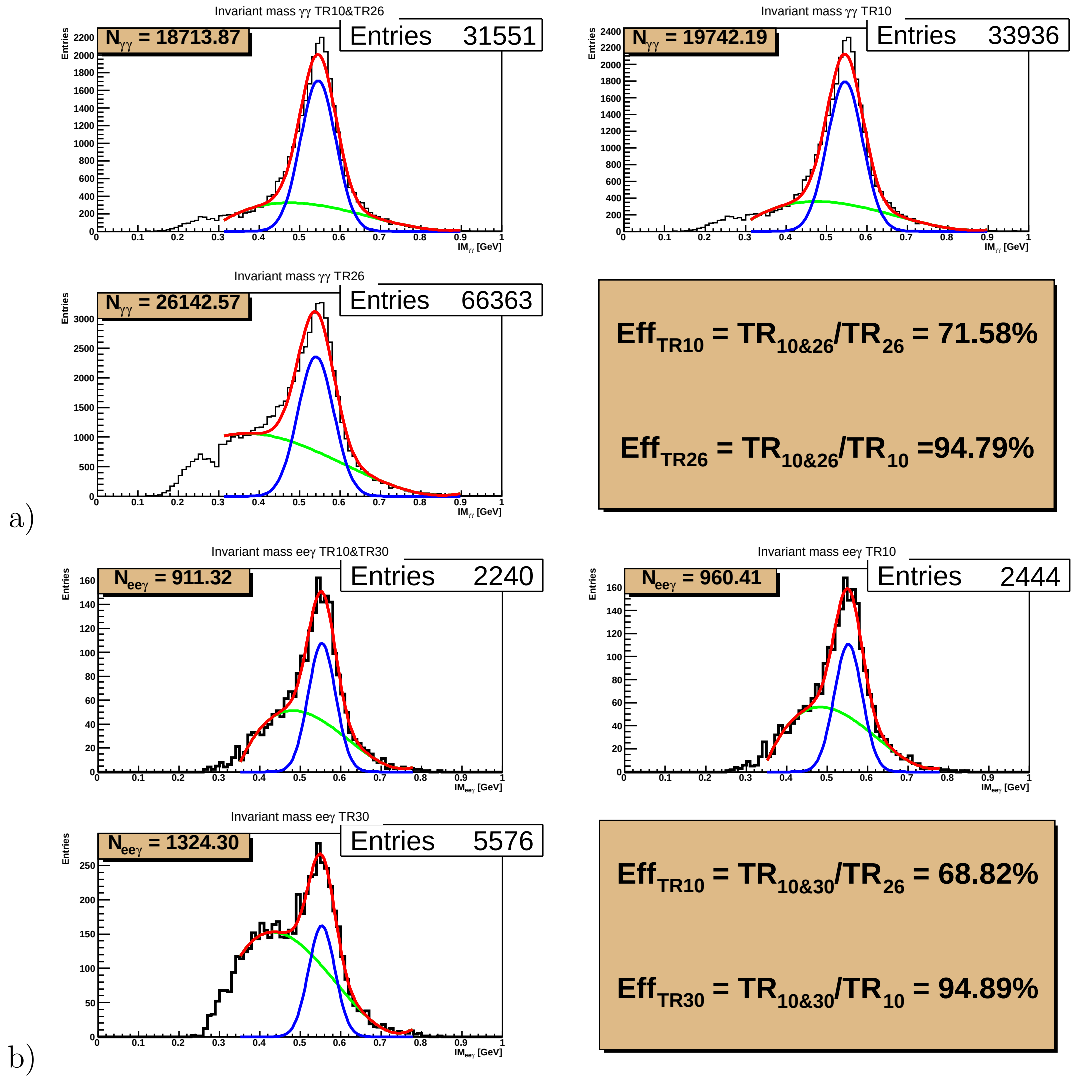

Figure 28: *Invariant mass plots used for the efficiency calculations of energy trigger for the two eta meson decay channels: a) $\eta \rightarrow \gamma\gamma$, b) $\eta \rightarrow e^+e^-\gamma$ (for a more detailed description see text).*

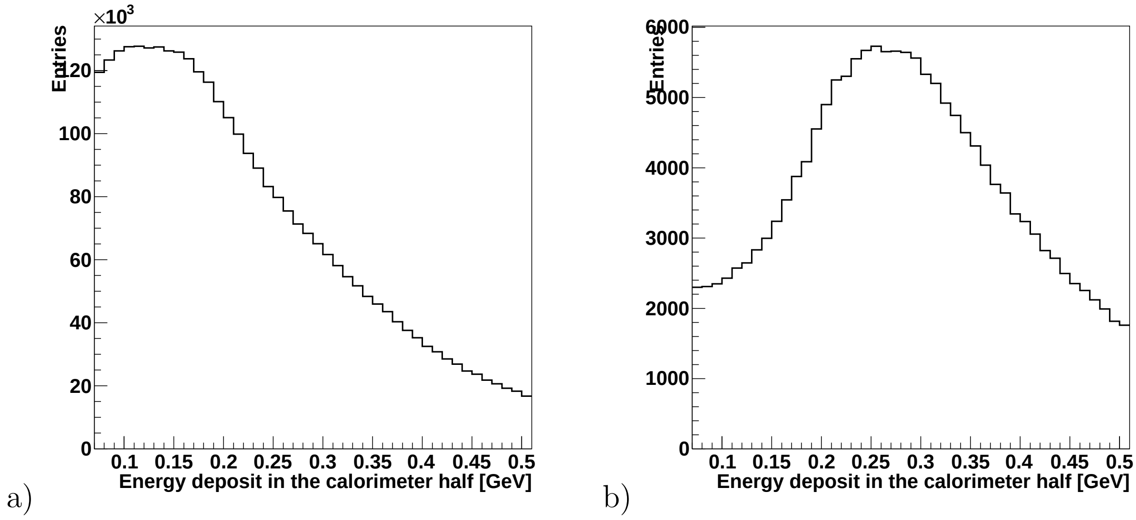

Figure 29: *The distributions of energy deposits in either half of electromagnetic calorimeter: a) events without energy trigger, b) events tagged with energy trigger flag.*

where A, B and C are the free parameters, and the x variable is the value of bin from the histogram. The fig.30 shows the fit results in the range of 0.1 GeV up to 0.4 GeV. The fit chi2 per number of degrees of freedom was 4.2. Outside the $0.1 - 0.4$ GeV range the constant lines were plotted.

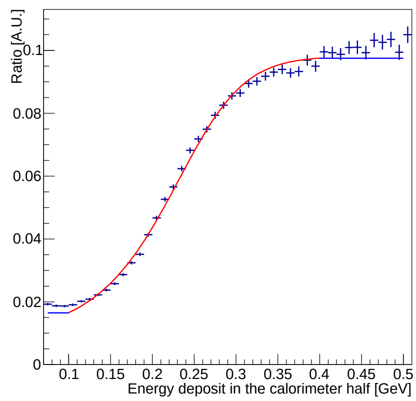

Figure 30: *The distribution of the relation between the number of events with specific energy deposit with or without energy trigger tagged. Data is shown as points with statistical error only, red line shows the fit results in the range of* $0.1 - 0.4$ GeV *and blue line indicates the linear behavior range assumed.*

3.3.7 Monte Carlo Simulation of Trigger Response

The function obtained above after normalization to the unity at the highest point of the fit was used to simulate energy trigger response in the simulation. For energy deposits in halves of electromagnetic calorimeter outside the $0.1 - 0.4\ GeV$ range constant behavior was assumed with probability of 1 for the energy deposits above $0.4\ GeV$ and minimal probability for energy deposit below $0.1\ GeV$ - the same as minimum value of the probability function in the $0.1\ GeV$ point. After the normalization this function tells us about the probability of saving an event with a given energy deposit in either half of electromagnetic calorimeter. In simulations each event were reweighted according to the product of the probabilities corresponding to the energy deposit in each half of electromagnetic calorimeter.

It was checked that the application of the probability function to the generated $\eta \to \gamma\gamma$ events leads to decreasing of an acceptance to $\sim 80\%$. This number can be compared to previously calculated for data trigger efficiency 72%.

3.4 Rest Gas Contribution

,,Rest gas" is defined as the remnants of gas left in the scattering chamber due to evaporated and bounced out pellets not sucked entirely by the pump system. The purpose for this study is following: we expect that charged events should have worse acceptance outside the ,,true" vertex point than neutral events, due to the reconstruction algorithm issues and geometrical coverage of Mini Drift Chamber. The second effect is that when we reconstruct neutral tracks from hits in the Electromagnetic Calorimeter we assume for angle determination that the vertex point were in the center of coordinate system. In that case events produced not in the vertex are reconstructed with wrong angles and as a consequence we assume wrong momentum vector for them. This should effect the invariant mass reconstruction and moreover acceptance derived from Monte Carlo simulations. This study also allows us to measure the contribution of the rest gas in the data sample, as a byproduct we can measure in data the spread and position of x and y vertex coordinate to tune the Monte Carlo simulations. The x value is correlated with pellet diameter and its positioning and y value depends on the width and spread of the COSY beam. In order to investigate the influence of the rest gas on the reconstruction of events the following Monte Carlo simulations were performed.

3.4.1 Monte Carlo Simulations for the Rest Gas Events

In the Monte Carlo simulation program the flat distribution of the rest gas along z (beam) axis were assumed (see fig.31). So instead of smeared around (0,0,0) vertex point in the simulations we investigate the case where z vertex point coordinate with equal probability takes value between -90 cm and 90 cm. A special algorithm for vertex reconstruction using a point of closest approach of two charged tracks as a vertex position. For this method 100k of $pp \to pp(\eta \to e^+e^-\gamma)$ simulated events were used. In order to be able to extract the reconstructed vertex point only events with exactly 2 oppositely charged tracks were used. Also to be sure that we don't interchange electrons in the central detector with protons we allow only events with 2 forward charged tracks within the angular acceptance of the detector. Furthermore we neglect events where the distance between charged tracks is greater than 5 mm, which clearly indicates wrongly reconstructed tracks, as both particles should come from the same point of interaction. As expected for the $pp \to pp(\eta \to e^+e^-\gamma)$ simulation events accepted by the above conditions were located near the true $z = 0$ vertex

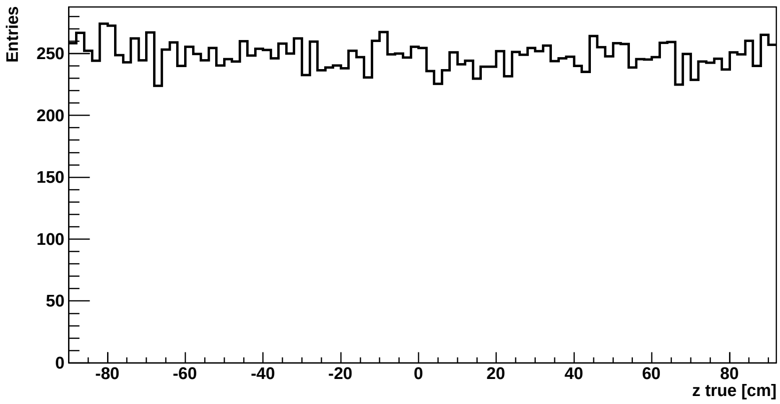

Figure 31: *The simulation of flat contribution of the rest gas along z (beam) axis.*

point (see fig.32a). For completeness we check also spread of true z coordinate of the vertex

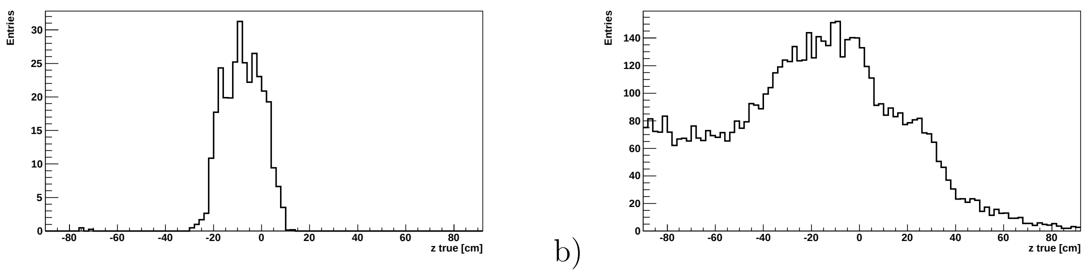

a) b)

Figure 32: *True z vertex coordinate for the selected after reconstruction* $\eta \to e^+e^-\gamma$ *events (a) and* $\eta \to \gamma\gamma$ *events (b) with rest gas only (simulations).*

for the $pp \to pp(\eta \to \gamma\gamma)$ simulations of 100k events with the same flat vertex z coordinate distribution. Here we only accept events with 2 forward charged tracks within the angular acceptance of the detector and exactly 2 neutral particles in the central detector. In comparison the accepted true vertex points are much more stretched along z axis (see fig.32b). This effect has a strong influence in the reconstructed invariant mass of eta, which can be seen in fig.33a and fig.33b. In the first picture the $IM_{\gamma\gamma}$ is shown and in the second figure $IM_{\gamma\gamma}$ is plotted in the function of the true vertex position. The events downstream or upstream the beam direction have wrong momentum vectors assumed due to the reconstruction algorithm that calculates them as coming from the center of coordinate system. The cut line at -50 cm and 40 cm are connected to the particles collected with backward or forward part of electromagnetic calorimeter respectively and therefore having completely wrong angles reconstructed. To quantify the effect of the rest gas, the efficiency of vertex reconstruction for $\eta \to e^+e^-\gamma$ channel was calculated by dividing the reconstructed vertex point spectra (see fig.34) by the distribution of true value of vertex position. The output histogram was parameterized with gaussian fit over a polynomial function (see fig.35).

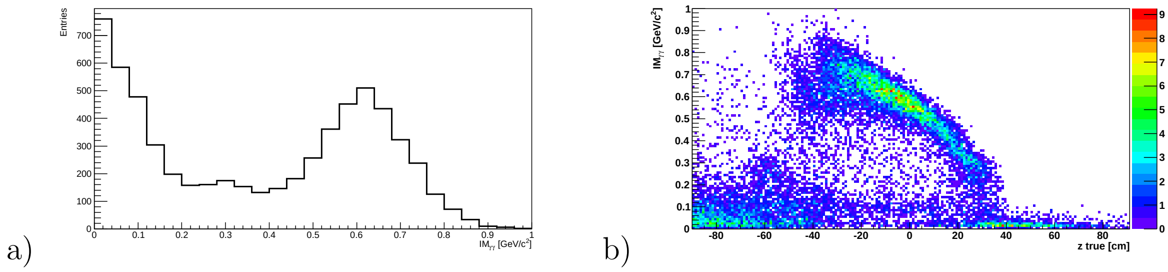

Figure 33: *a) Reconstructed invariant mass of two photons, b) Invariant mass of two photons as a function of true z vertex coordinate. Both pictures for $\eta \to \gamma\gamma$ with rest gas only Monte Carlo simulation .*

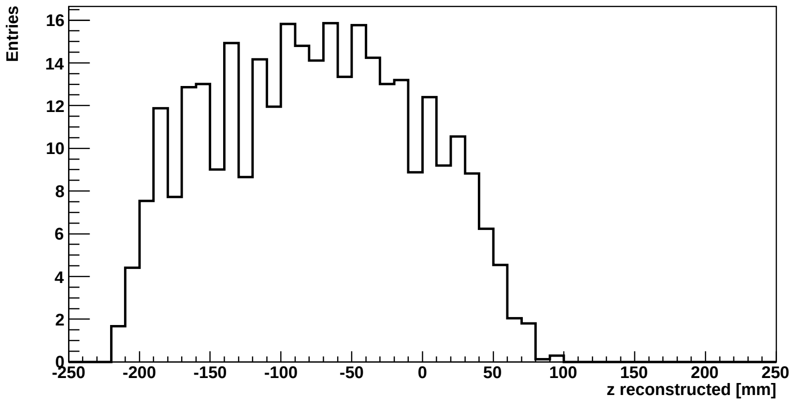

Figure 34: *Reconstructed z vertex coordinate for Monte Carlo $\eta \to e^+e^-\gamma$ simulation with rest gas only after channel selection.*

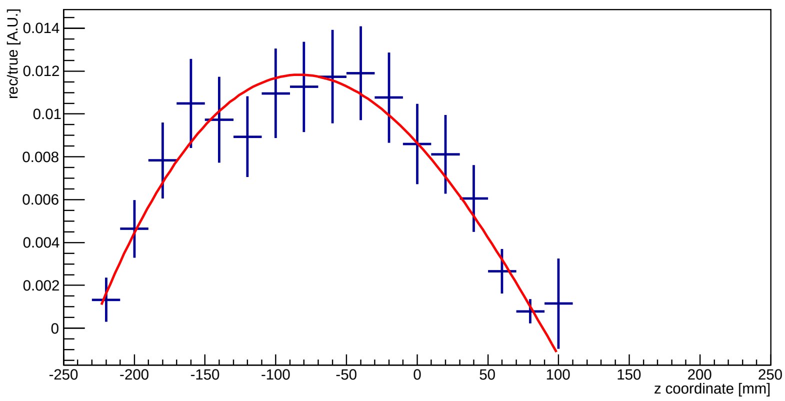

Figure 35: *Efficiency of z vertex coordinate reconstruction for $\eta \to e^+e^-\gamma$ Monte Carlo simulation with rest gas only after channel selection (the last data point is excluded from the fit).*

3.4.2 Rest Gas Contamination in the Data

The same study as for the Monte Carlo simulations were performed for data sample where we have an admixture of the beam interactions with the rest gas. The selection of events and procedure for vertex reconstruction was the same as for $\eta \to e^+e^-\gamma$ Monte Carlo simulations in the previous section. The plot of reconstructed z value is shown in fig.36a for the 20 runs of experimental data. In order to extract the value of rest gas amount we divide the spectra

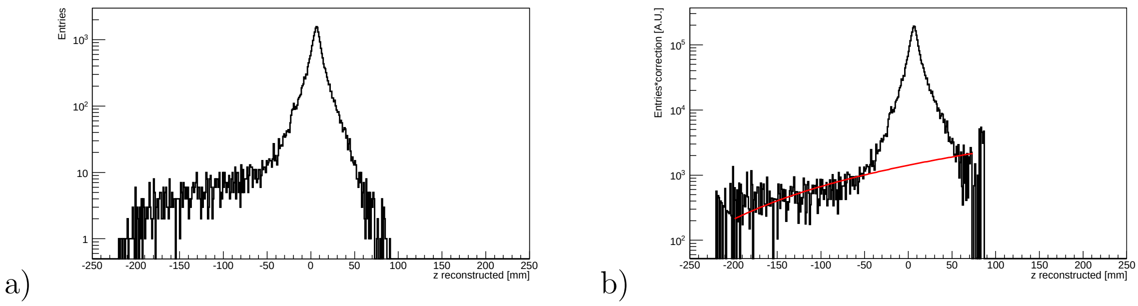

Figure 36: *Reconstructed z vertex coordinate for data events before (a) and after (b) efficiency correction. The polynomial fit to the rest gas contribution is shown (for more information please see the text).*

by the efficiency function bin by bin. Next, the efficiency corrected spectrum is fitted with gaussian distribution above the polynomial background. The outcome of this procedure can be seen in fig.36b with polynomial fit line only that shows the rest gas contribution. The value of rest gas contamination in data is estimated to 10% and it is constant along the whole time of the experiment. The one remarkable thing that we can derive from the reconstructed data vertex point is that we don't see almost any rest gas contribution along positive z values most likely due to reconstruction reasons.

To have better parametrization of vertex position the x and y components of vertex points reconstructed from data were analyzed. Parameters of fitted gaussian distribution shown in fig.37 were used to improve a Monte Carlo simulations. The values of parameters obtained are summarized in table 5.

	Mean [mm]	σ [mm]
Vertex x position	-0.27 ± 0.01	1.46 ± 0.01
Vertex y position	0.23 ± 0.01	1.80 ± 0.01

Table 5: *Vertex x and y parameters obtained from data distributions using gaussian fit.*

It is seen that larger fraction of events coming from the rest gas interactions are accepted in the case of $\eta \to \gamma\gamma$ than in $\eta \to e^+e^-\gamma$ decay channel. The data spectra were used to parameterize the vertex position and its spread for the Monte Carlo simulations.

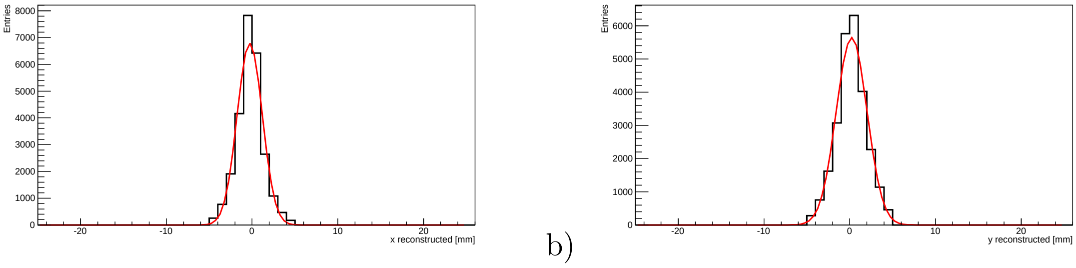

a) b)

Figure 37: *Reconstructed x (a) and y (b) vertex coordinate for data events with superimposed gaussian fit results (red line).*

3.5 External Conversion

One of the most prominent backgrounds to single Dalitz decay of η meson is external conversion of photons in the detector material, especially those coming from $\eta \to \gamma\gamma$. The lepton pair vertex position was calculated from the closest distance between the measured points on the two charged tracks in the XY plane. Than the reconstructed vertex is set to the mean values of that points coordinates. Reconstructed vertex position in the XY plane is shown in fig.40. It is observed that the external conversion mainly occurs in the material of beryllium beam tube at $R = 30\ mm$. In same the figure the clusterization of points is seen at the position of connection between pellet tubes and beam pipe at 90° and 270°. Such effect is not observed in the real data. It can be explained by the wrong material type and its amount implemented in the simulations. To have the proper description of data in the simulations we define the graphical cut to get rid of these kind of events shown in fig.40a as a red line. Vertex distance which is the distance in the XY plane from $(0, 0)$ point to the calculated vertex position point is presented in fig.41. In the parallel we calculate the invariant mass of e^+e^- pair at the position of beam pipe, which should be smaller then 10 MeV for external conversion. The idealized idea of the different behavior of external conversion and single Dalitz is shown in fig.39. It is clearly seen that the concentration of events in the smallest mass region and for the vertex position larger than about 30 mm is due to the external conversion and should be removed. In the fig.38 the plot of vertex distance as a function of the invariant mass of e^+e^- pair calculated at the beam pipe position is shown for simulated single Dalitz decay of eta meson (a), simulated photon conversion events from $\eta \to \gamma\gamma$ (b) and the data (c). We define conversion events by the value of the vertex distance and invariant mass of e^+e^- pair calculated at the beam pipe position as shown in fig.38a with an area between red lines.

From Monte Carlo simulations of $\eta \to e^+e^-\gamma$ channel and $\eta \to \gamma\gamma$ decay with the external photon conversion the signal to external conversion background ratio changed after the cut from $2:1$ to $19:1$. The signal loss estimated from the simulations is 15% and the external conversion reduction is at the level of 91%. The shape of invariant mass of electron-positron pair before and after the conversion reduction procedure is shown in fig.42. Also in fig.43 the shape of invariant mass of electron-positron pair after conversion subtraction is shown in the comparison to expected spectrum from the reconstructed single Dalitz of η meson.

The alternative approach for the conversion cut is illustrated in fig.44 where plot of

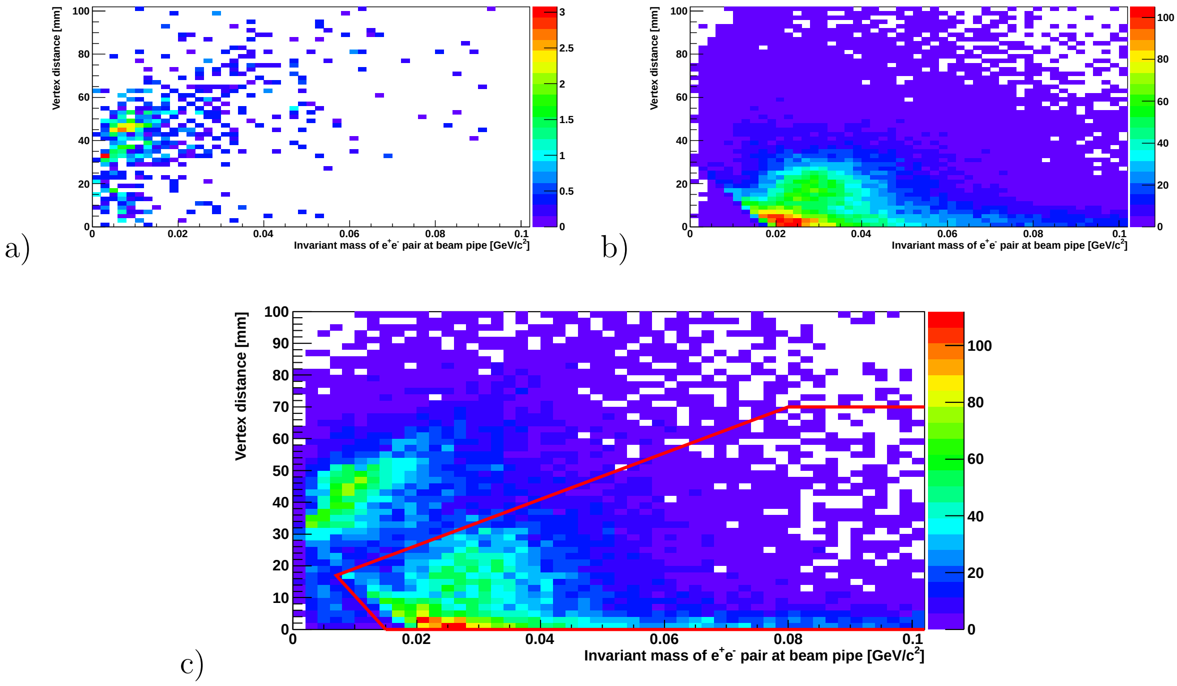

Figure 38: *Plot of vertex distance as a function of the invariant mass of* e^+e^- *pairs calculated at the beam pipe position: a) generated conversion events from* $\eta \to \gamma\gamma$ *decays, b) single Dalitz of* η *meson simulation, c) data with the selection condition shown in red.*

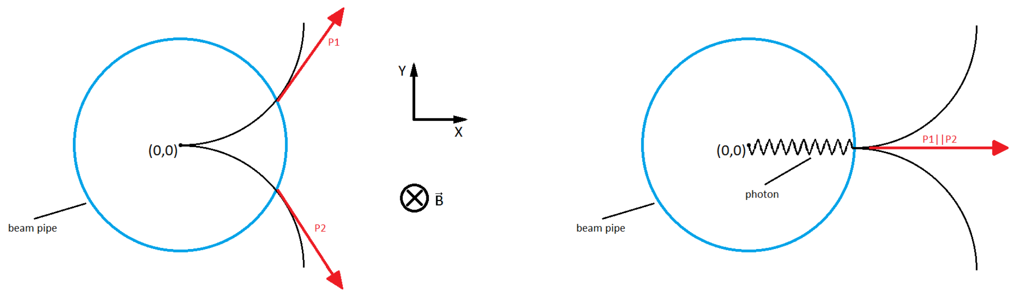

Figure 39: *The illustration of the effect on non-conversion and conversion pairs. The left diagram shows single Dalitz of* η *meson, where the* e^+e^- *pair is coming from the origin. In this case the magnetic field changes the direction of momentum vectors and therefore invariant mass of* e^+e^- *pairs calculated in the point of beam pipe is larger than the actual value. The right diagram shows the external conversion effect for single photon. Here, the* e^+e^- *pair is created in the beam pipe so the momentum vectors are parallel and the invariant mass is close to the mass of two electrons.*

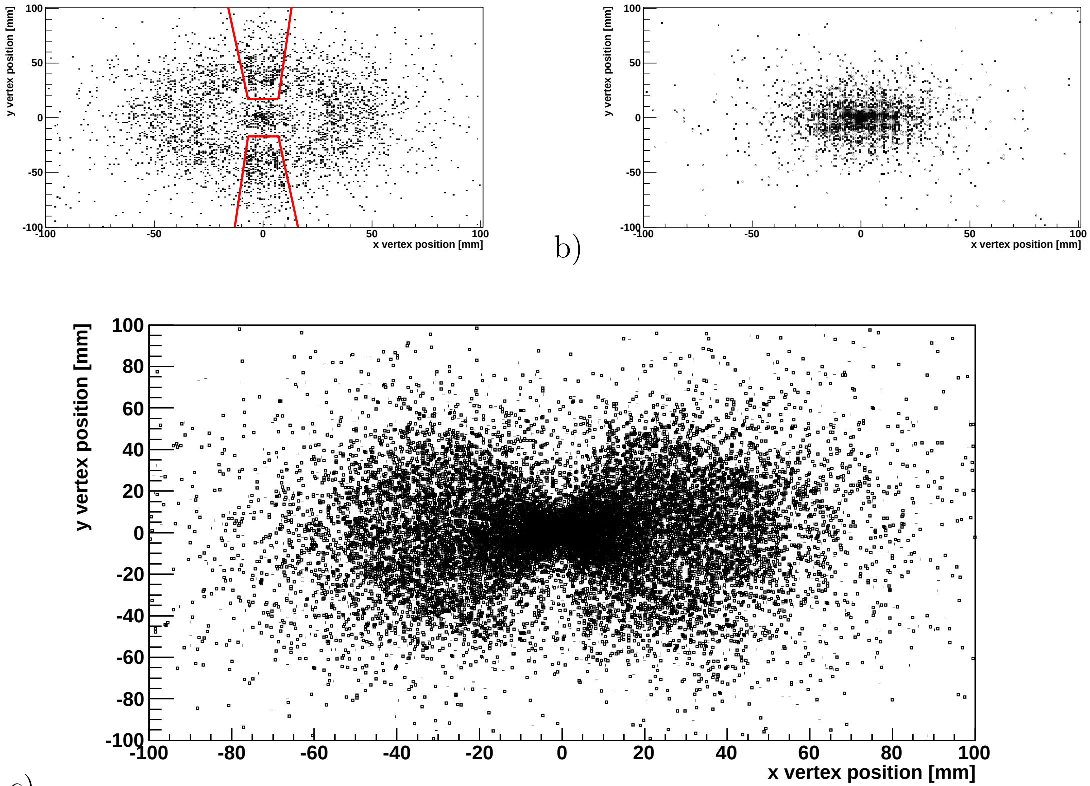

Figure 40: *Reconstructed vertex position on the XY plane: a) generated conversion events from $\eta \to \gamma\gamma$ decays, the red line shows the graphical cut used to suppress unwanted conversion events in the simulation, b) single Dalitz of η meson simulation, c) data.*

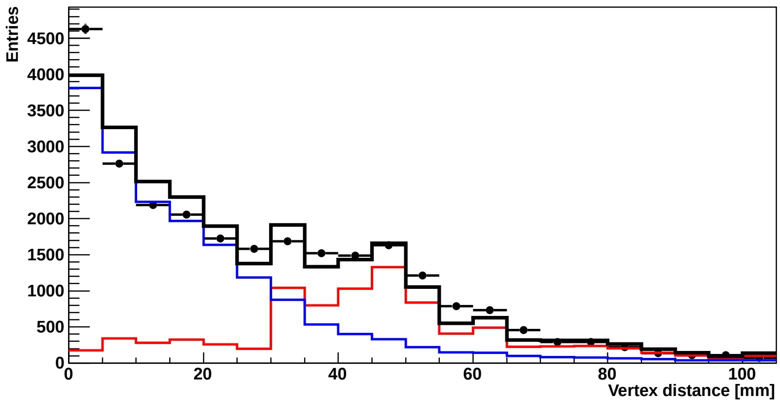

Figure 41: *The value of reconstructed vertex distance. Full points - data, blue line - single Dalitz of η meson simulation, red line - generated conversion events from $\eta \to \gamma\gamma$ decays, black line - sum of above Monte Carlo simulations.*

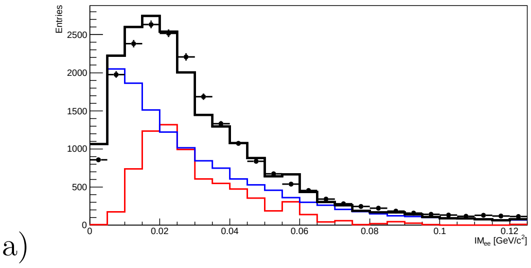

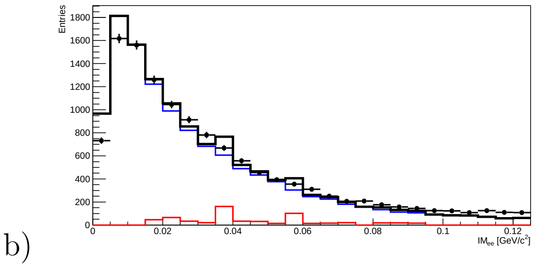

Figure 42: *Invariant mass of e^+e^- pair: a) before conversion cut, b) after conversion cut. Full points - data, blue line - single Dalitz of η meson simulation, red line - generated conversion events from $\eta \to \gamma\gamma$ decays, black line - sum of above Monte Carlo simulations.*

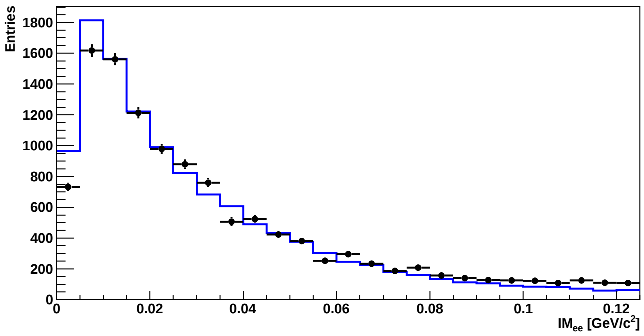

Figure 43: *Invariant mass of e^+e^- pair after external conversion subtraction from data. Full points - data, blue line - single Dalitz of η meson simulation.*

vertex distance as a function of the invariant mass of e^+e^- pairs calculated at the beam pipe position is shown. The red lines define the conversion area and indicate the cuts on the vertex distance greater than 30 cm and the invariant mass of e^+e^- pairs calculated at the beam pipe position less than 10 MeV. The analysis under this conditions change the signal to external conversion background ratio after the cut to 22 : 1 as compared to previously obtained 19 : 1. The signal loss is 20% in this case and the external conversion reduction is equal to 93% (previously 15% and 91% respectively). The difference between the cuts used gives some information about systematic errors of this condition. It did not change substantially the shape or number of event on the final distribution of the invariant mass of e^+e^- pairs.

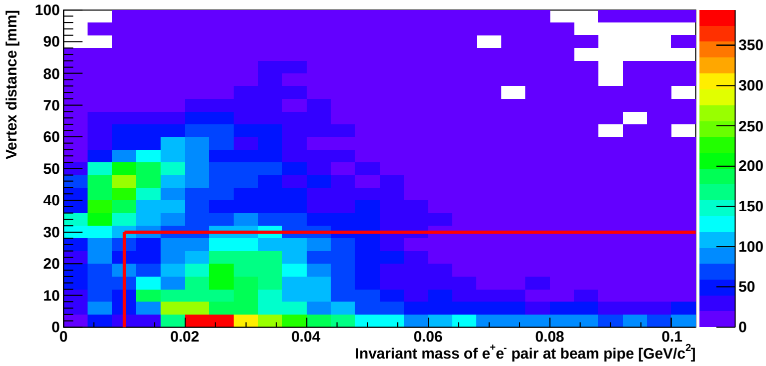

Figure 44: *Plot of vertex distance as a function of the invariant mass of* e^+e^- *pairs calculated at the beam pipe position for data with the alternative selection condition shown in red. For more information please refer to the text.*

4 Normalization Using $pp \to pp(\eta \to \gamma\gamma)$ Reaction

For the normalization (to estimate the number of η mesons produced in the data sample) $\eta \to \gamma\gamma$ decay channel was used. To clean up and enhance data sample for this particular decay channel following requirements were applied:

- Two or more charged tracks in the Forward Detector. Number of those track for data and Monte Carlo simulation for $\eta \to \gamma\gamma$ is shown on fig.45.

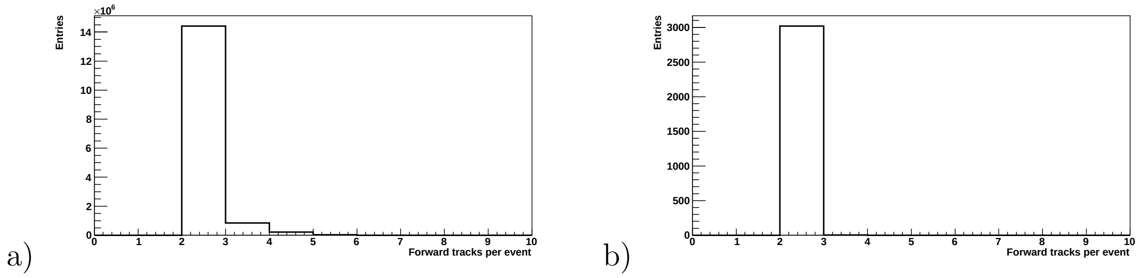

Figure 45: *Charged tracks multiplicity in the Forward Detector per event: a) data and b) $\eta \to \gamma\gamma$ simulation.*

- Two or more neutral tracks in the Central Detector. Multiplicity of those tracks for data and Monte Carlo simulation for $\eta \to \gamma\gamma$ is shown on fig.46.

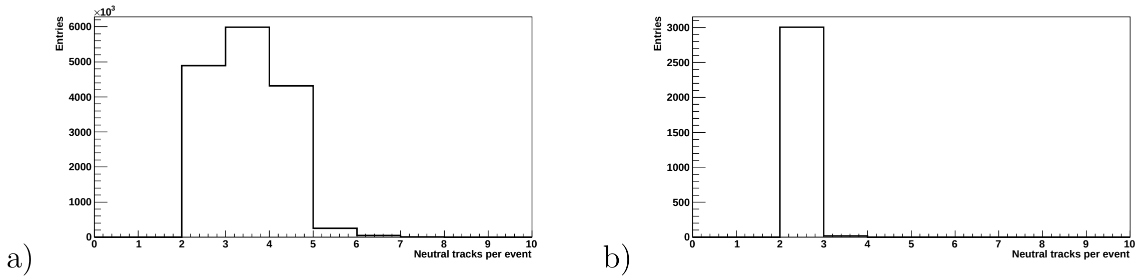

Figure 46: *Neutral tracks multiplicity in the Central Detector per event: a) data and b) $\eta \to \gamma\gamma$ simulation.*

- No charged tracks in the Central Detector.
- The two charged tracks in the Forward Detector closest in time within theta angular range of 3°-18° and emitted with the time difference less than 20ns (see fig.47 for the time difference distribution for those tracks) were selected.
- We request two neutral tracks in the Central Detector giving the greatest opening angle between them in the XY plane (approximation of back-to-back emission of the two photons from the eta meson decay in the CM system - see fig.48).

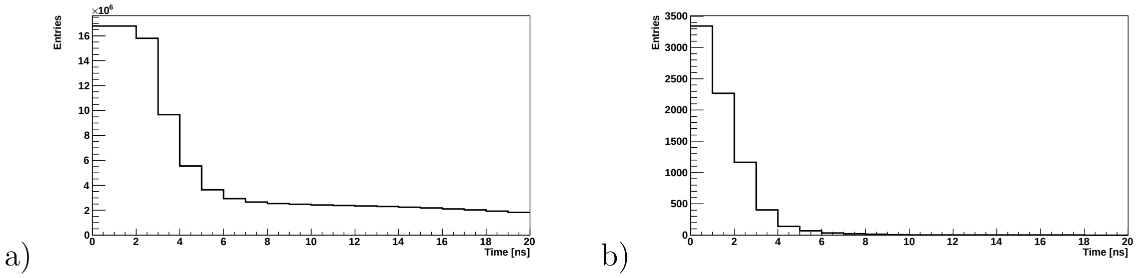

Figure 47: *Time difference between charged tracks in the Forward Detector: a) data and b)* $\eta \to \gamma\gamma$ *simulation.*

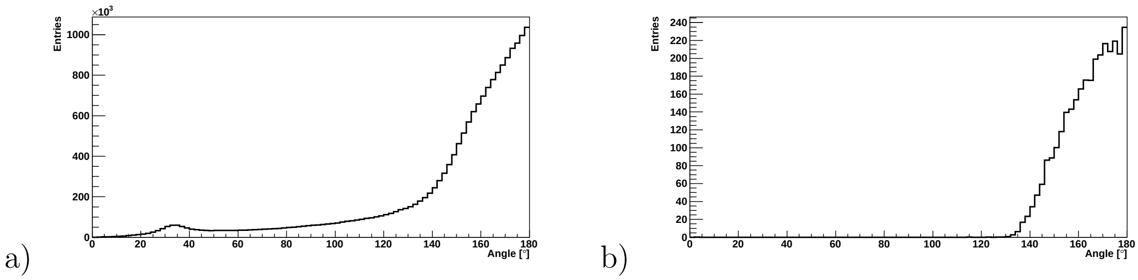

Figure 48: *Emission angle between selected two neutral tracks in the central detector in the* XY *plane: a) data and b)* $\eta \to \gamma\gamma$ *simulation.*

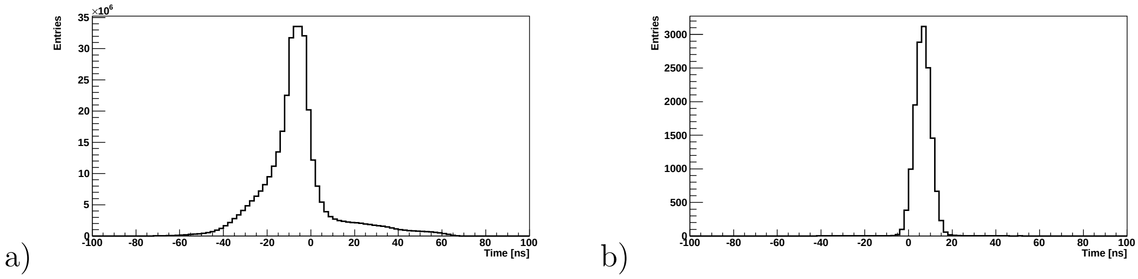

Figure 49: *Time difference between mean time of charged tracks in the Forward Detector and neutral tracks in the Central Detector: a) data and b)* $\eta \to \gamma\gamma$ *simulation.*

- The neutral tracks have to be emitted in [-25,+35]ns bounds around mean time of two Forward Detector charged tracks found in previous step (see fig.49 for the time difference distribution for those tracks). In addition the time difference between the two Central Detector neutral tracks cannot be greater than 50ns (see fig.50 for the time difference distribution for those tracks) and there cannot be any Plastic Barrel Scintillator hit in the time interval of 100ns around each of this Central Detector neutral track.

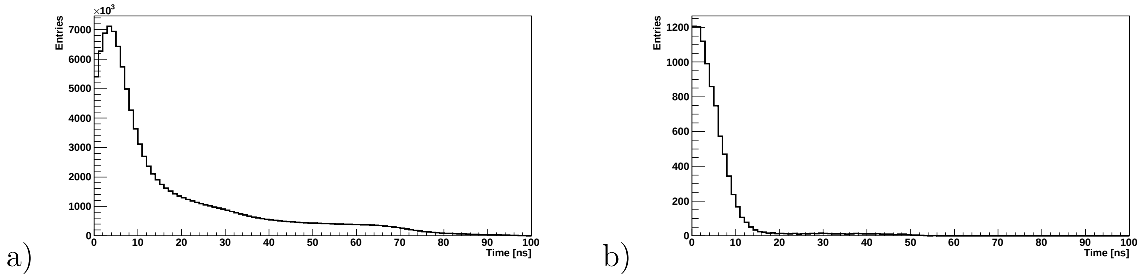

Figure 50: *Time difference between neutral tracks in the Central Detector: a) data and b)* $\eta \to \gamma\gamma$ *simulation.*

- Each neutral track have to be in the proper theta angle interval to mimic the trigger conditions for Monte Carlo data sample (for more information about trigger see section 3.3 [trigger]).

Those cuts left us with $1.94 \cdot 10^7$ $\eta \to \gamma\gamma$ event candidates (see fig.51 for invariant mass of two photons and missing mass of two protons distribution). At first let define a low energy

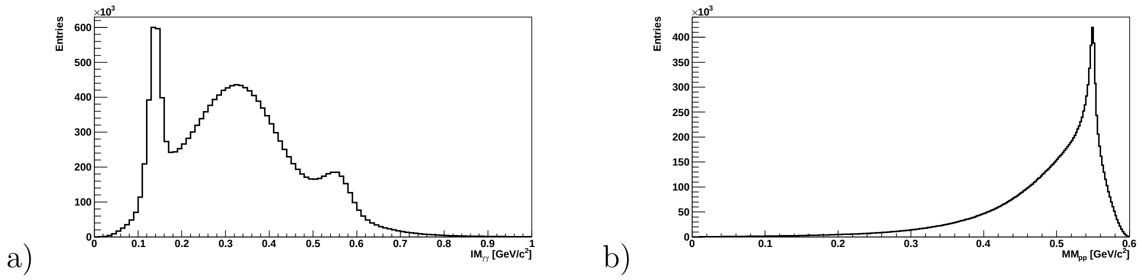

Figure 51: *Distributions for events with two or more photons: a) invariant mass of two photons and b) missing mass of two protons.*

photon as a neutral track in the Central Detector with momentum less than 50 MeV and a high energy photon as a neutral track in the Central Detector with momentum greater than 150 MeV. We divide the invariant mass distribution of two photons into two different classes - one with exactly two high energy photons and any number of low energetic photons and the second one with more than two high energy neutral tracks in the Central Detector. In fig.52 one can see invariant mass distributions for both classes and the second one doesn't show a maximum at the mass of $\eta \to \gamma\gamma$ decay. Due to that fact for further analysis only events with exactly two high energy neutral tracks in the Central Detector were chosen. In fig.52a one can also see the gaussian fit, above polynomial background to the π° invariant mass distribution that gives $\sigma = 17.6\ MeV$ $(FWHM = 41.4\ MeV)$ and peak position at $136.7\ MeV$. The correlation of invariant mass of two photons and missing mass of two

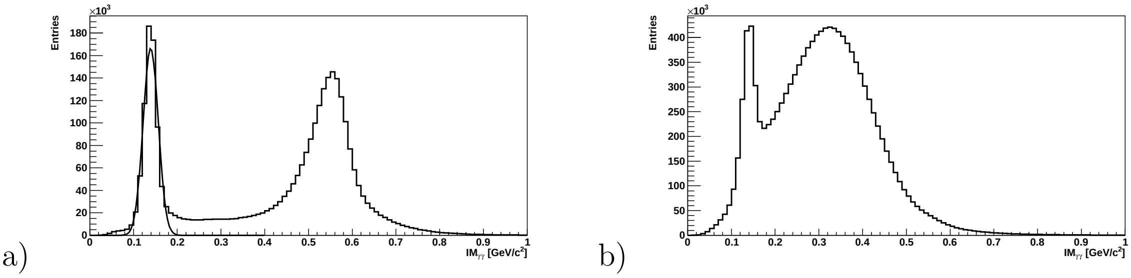

Figure 52: *Invariant mass of two photons for data events with: a) exactly two high energy photons b) more than two high energy photons. In the left diagram fit to* π° *mass is shown.*

protons for events with exactly two neutral particles in the Central Detector are shown in the fig.53, where one can clearly see the area of η meson production and it's decay into two photons and the band of π° production with some photons lost due to geometrical acceptance of Electromagnetic Calorimeter and reconstruction efficiency. In order to have

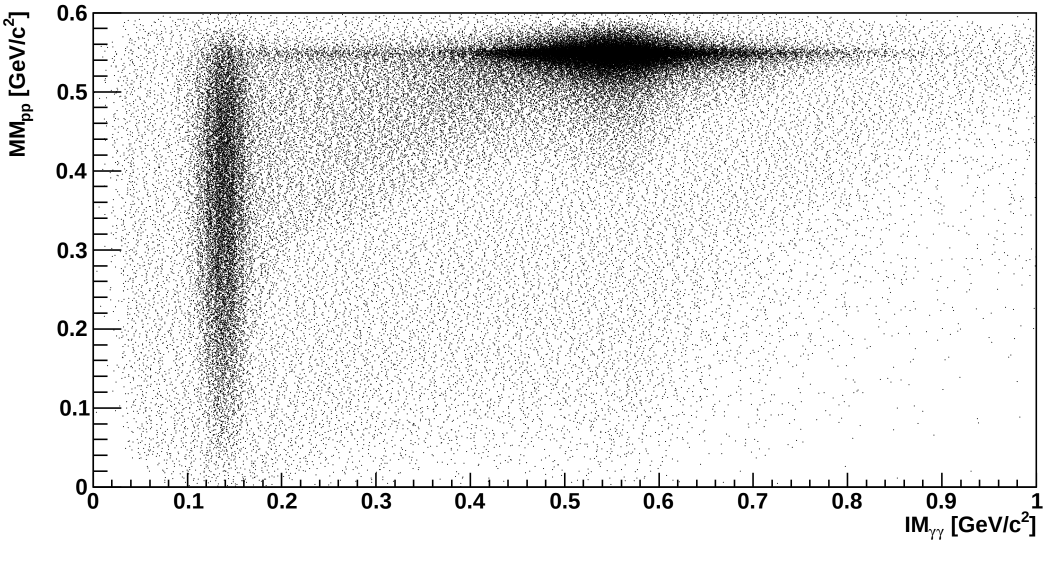

Figure 53: *Invariant mass of two photons distribution for data events in the function of missing mass of two protons.*

the same conditions for data and Monte Carlo simulation we select trigger effects cut of energy deposit in each half of SEC $>$ 150 MeV and each photon in the opposite half of the central detector. In fig.54 correlation between energy deposits in each half of Electromagnetic Calorimeter is shown. We choose most of η meson decays by requesting missing mass of two protons in the range of the η meson mass, so MM_{pp} in $0.5 - 0.6\ GeV$ interval. In fig.55 the invariant mass of two photons distribution is shown. The signal shape was fitted above polynomial background in the range of $0.2 - 0.9\ GeV$, to estimate the background shape above peak. The fit results are as follows: in the data distribution of invariant mass of two photons we have 76% signal content with 15% of polynomial background under $\eta \to \gamma\gamma$ peak and less than 9% of unknown content that can be due to overlapping events. The fit results shows that we are left with $N_{ev} = 1.4 \cdot 10^6$ events. For further calculations

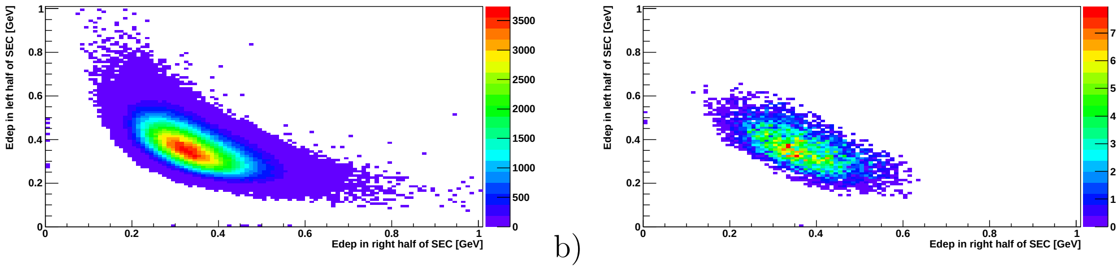

a) b)

Figure 54: *Energy deposits in each half of Electromagnetic Calorimeter: a) data and b)* $\eta \to \gamma\gamma$ *simulation.*

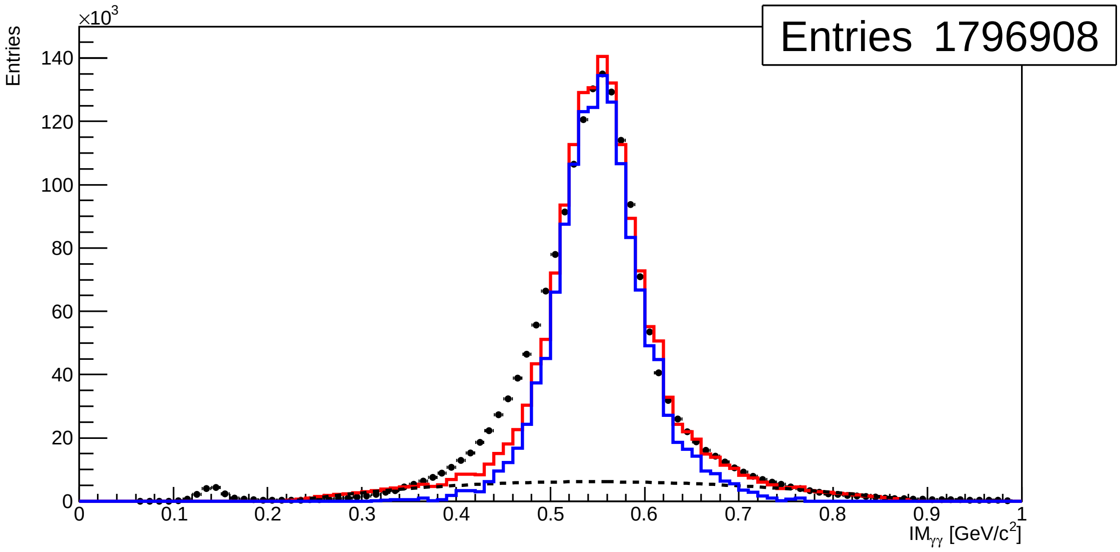

Figure 55: *Invariant mass of two photons distribution for data events (points) with fitted signal shape (blue line) above polynomial background (dotted line). Red line is a sum of signal function and background contribution.*

we define acceptance for $\eta \to \gamma\gamma$ decay channel based on Monte Carlo simulations as:

$$Acc_{\gamma\gamma} = Tr_{eff} \cdot Geo_{acc} \cdot Rec_{eff} \cdot Cuts, \tag{13}$$

where the acceptance includes trigger efficiency (Tr_{eff}), geometrical acceptance (Geo_{acc}), reconstruction efficiency (Rec_{eff}) as well as selection criteria described above ($Cuts$). For the final selection the acceptance is equal to 6.0%. The number of event surviving each set of cuts and acceptance after certain analysis steps are summarized in table 6.

Requirement	N_{ev} data	MC Acc
Any number of photons	$12.21 \cdot 10^6$	9.7%
Two high energy photons	$2.24 \cdot 10^6$	9.0%
γ energy, EdepLR, MMpp	$1.78 \cdot 10^6$	6.0%
Shape Fit	$1.40 \cdot 10^6$	6.0%

Table 6: *Number of $\eta \to \gamma\gamma$ events and Monte Carlo acceptance after selection criteria. N_{ev} - Number of data events surviving particular cut; MC Acc - Acceptance taken from $\eta \to \gamma\gamma$ channel simulation under this condition. Each criterion assumes that all previous requirements were also in use and each counts only events within $0.2 - 0.9$ GeV range of invariant mass of two photons. For the explanation of each of the selection cuts please refer to the text.*

The total number of the produced η mesons can be estimated using the formula:

$$N_\eta = N_{ev}/(Acc_{\gamma\gamma} * BR_{\gamma\gamma}), \tag{14}$$

where BR for $\eta \to \gamma\gamma$ is equal to 39.31% [3]. Finally the total number of η mesons produced during the data collection is:

$$N_\eta =\sim 5.97 \cdot 10^7.$$

To estimate the systematic uncertainty of obtained above value for the total number of η mesons produced it has been recalculated with different initial conditions for several selection criteria mentioned in this section. The simple way to obtain the value of the systematic uncertainty (σ_{sys})is to add the squares of all individual contributions under the square root:

$$\sigma_{sys} = \frac{1}{N}\sqrt{\sum_i (x_r - x_i)^2}, \tag{15}$$

where x_r is reference value and x_i is measurement under the change in the analysis code. The checked analysis conditions were described below, and the systematic error contributions are summarized in the table 7.

- Missing mass of two protons cut (MM_{pp}).
  The missing mass of two protons cut helps us to select events coming from η meson decays. The original cut value was MM_{pp} in $0.5 - 0.6$ GeV interval. In order to check the influence of this criterion we differ this cut in two ways: one is more strict with the MM_{pp} cut value $0.52 - 0.58$ GeV and the second one is more loose with the MM_{pp} cut value $0.48 - 0.62$ GeV. The corresponding distributions of signal shape fitted above polynomial background are shown in fig.56.

- Photon selection for the analysis.
  In the analysis we change the way in which we select photons for further calculations. In the original two photons are chosen from all available with the requirement of highes opening angle in the XY plane. Here we change this condition to the one that selects two most energetic neutral particles in the central detector. The corresponding distributions of invariant mass of two photons is almost the same as before.

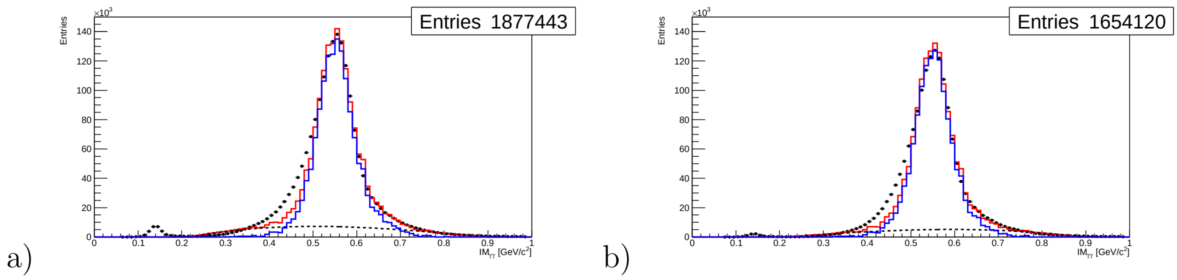

Figure 56: *Invariant mass of two photons distribution for data events (points) with fitted signal shape (blue line) above polynomial background (dotted line). Red line is a sum of signal function and background contribution. The pictures shows the distributions with a change in the cut on missing mass of two protons to more loose one (a) or more strict one (b) as described in text.*

- Threshold value for the energy deposits in the halves of electromagnetic calorimeter ($EdepLR$).
  In $\eta \to \gamma\gamma$ decay at this energy photons should have the high value of the opening angle and therefore aim into opposite halves of electromagnetic calorimeter. The threshold value ensures that the event collected is connected to the situation where we have at least two photons of high energy possibly coming from $\eta \to \gamma\gamma$ decay. The corresponding distributions of signal shape fitted above polynomial background are shown in fig.57.

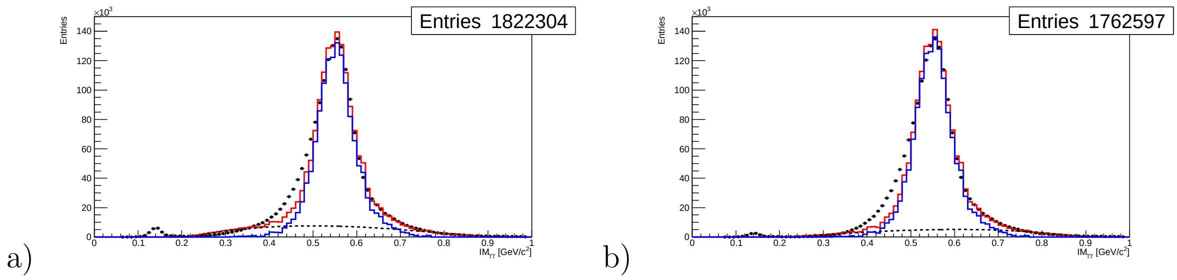

Figure 57: *Invariant mass of two photons distribution for data events (points) with fitted signal shape (blue line) above polynomial background (dotted line). Red line is a sum of signal function and background contribution. The pictures shows the distributions with a change in the condition on threshold energy deposited in the electromagnetic calorimeter to more loose one (a) or more strict one (b) as described in text.*

- Threshold value for the minimum energy of photon to be considered as high energy in the analysis (E_γ).
  In the analysis we finally select only events with a strict number of photons of energy grater than 150 MeV. If we change the threshold value to either 125 MeV or 175 MeV we don't see almost any change in the final distribution.

- The shape of the signal function fitted as gaussian distribution ($EdepLR$).
  Two checks were performed when for the fitting the final distribution of the invariant

mass of two photons we used gaussian shape instead of signal shape for Monte Carlo simulations. The corresponding distributions of signal shape fitted above polynomial background are shown in fig.58. The left picture shows the fit results for the sum of single gauss above polynomial background and the left one illustrates the results for fit of double gauss with polynomial function. In the first case the mean value of gauss distribution was a free parameter but in the second picture both functions had fixed mean value to the η meson mass.

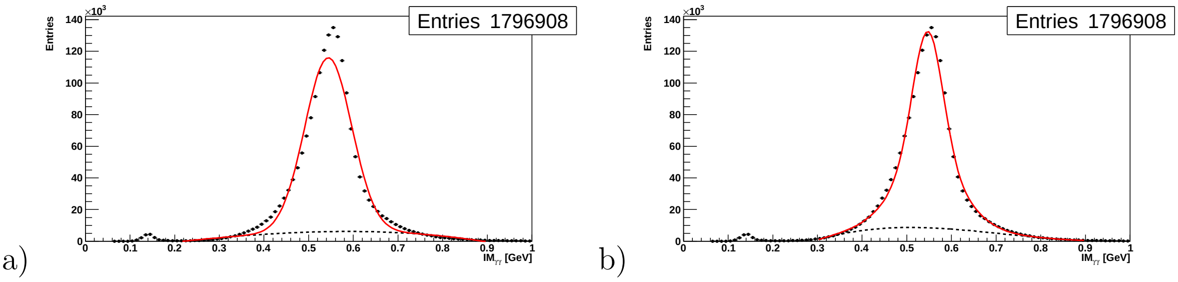

Figure 58: *Invariant mass of two photons distribution for data events (points) above polynomial background (dotted line). Red line is a sum of signal function and background contribution. The pictures shows the distributions with a fit using single gaussian distribution (a) or double gaussian distribution (b) as described in text.*

- The shape and range of the background function fitted.
  Several checks were performed using the different ranges for fitting the final distribution of the invariant mass of two photons with polynomial background function. Two sample distributions are shown if in fig.59. In the left picture the range of polynomial background has been changed from 0.2-0.9 GeV to 0.3-0.8 GeV. In the right picture the background function used was a polynomial of a higher order. Several attempts varying fit ranges and background shapes were made and the results are shown in table 7.

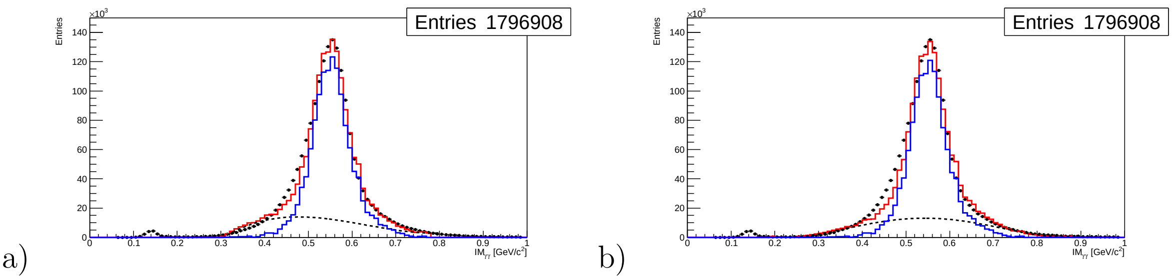

Figure 59: *Invariant mass of two photons distribution for data events (points) with fitted gaussian shape (blue line) above polynomial background (dotted line). Red line is a sum of signal function and background contribution. The pictures shows the sample distributions using different range of fit (a) and different shape of background assumed (b).*

If we take into account the different contributions to the systematic error using the equation 15 for the different systematic errors show in the table 7 the obtained result is $\sigma_{sys} = 0.14 \cdot 10^7$. The statistical error is negligible compared to the systematic errors. So finally the number of η mesons produced when we include the systematical error can be express be a number:

$$N_\eta =\sim 5.97 \pm 0.14_{syst} \cdot 10^7.$$

The other attempt to calculate the number of η mesons produced is to take the average of results obtained in table 7. Using the same method of systematic error calculation as previously we can express it as follows:

$$\overline{N}_\eta =\sim 5.91 \pm 0.12_{syst} \cdot 10^7.$$

Condition	$N_\eta \cdot 10^7$	*Acc*	$\lvert\Delta N_\eta\rvert \cdot 10^7$
Initial	5.97	6.0%	
Loose MM_{pp}	5.82	6.2%	0.15
Strict MM_{pp}	6.16	5.5%	0.19
Loose E_γ	5.97	6.0%	0.00
Strict E_γ	5.97	6.0%	0.00
Loose EdepLR	5.87	6.0%	0.10
Strict EdepLR	6.07	5.9%	0.10
Photon selection	5.97	6.0%	0.00
Gaussian shape	6.17	6.0%	0.20
Double gaussian shape	6.52	6.0%	0.55
Background shape	5.37 – 6.10	6.0%	up to 0.60
Fit range	5.28 – 6.05	6.0%	up to 0.69

Table 7: *The summarization of the systematic uncertainties under different analysis conditions or fit parameters. The table shows the total number of η mesons produced obtained while changing the initial parameters (N_η), the deviation of the result from the original value ($\lvert\Delta N_\eta\rvert$), Acc is acceptance taken from $\eta \to \gamma\gamma$ channel simulation under this condition. For the description of different analysis conditions please refer to the text.*

5 Analysis of $pp \to pp(\eta \to e^+e^-\gamma)$ Reaction

5.1 Introduction

The Feynman diagram of process in which the meson decays into a virtual photon and a real photon as shown in fig.60a. In the framework of Quantum Electrodynamics (QED) the virtual photon converts into e^+e^- pair, where q^2 is the squared four-momentum of this virtual photon and it is equal to the squared mass of the e^+e^- pair, following the relation below [61]:

$$q^2 = M^2_{e+e-} = (E_{e+} + E_{e-})^2 - (p_{e+} + p_{e-})^2, \tag{16}$$

where E denotes particle energy and p stands for its momentum. This process is called conversion decay or referred as single Dalitz decay. The QED theory gives an approximation for the formula of the differential cross section under assumption that the meson is point-like particle [60]:

$$\frac{d\Gamma_{l^+l^-\gamma}}{dq^2 \cdot \Gamma_{\gamma\gamma}} = \frac{2\alpha}{3\pi q^2}\sqrt{1 - \frac{4m_l^2}{q^2}}\left(1 + \frac{2m_l^2}{q^2}\right)\left(1 - \frac{q^2}{M_P^2}\right), \tag{17}$$

where l denotes lepton, α is the fine-structure constant, q^2 is the mass squared of the lepton-antilepton pair, m_l stands for the lepton mass, M_P is the mass of pseudoscalar meson. This calculations give the theoretical shape of e^+e^- invariant mass distribution shown in fig.60b (solid line) with detector influence not taken into account. The picture shows a dominant contribution from small masses of e^+e^-. The above equation does not take into account the structure of meson. To answer this problem all effects caused be the inner structure of the meson are introduced as an additional term called the transition form factor - $F(q^2)$:

$$\frac{d\Gamma_{l^+l^-\gamma}}{dq^2} = \frac{d\Gamma_{l^+l^-\gamma}}{dq^2 \cdot \Gamma_{\gamma\gamma}} \cdot \mid F(q^2) \mid^2 . \tag{18}$$

In the case of η meson Dalitz decays we have a situation when the transition vertex contains only one meson, so the transition form factor gives an information about the structure and the properties of the meson itself. The transition form factor used in generation assumed single-pole formula with parameter Λ related to the mass of the vector meson [68]:

$$F(q^2) = \left(1 - \frac{q^2}{\Lambda_P^2}\right)^{-1}, \tag{19}$$

where $\Lambda_P = 0.73$ and q^2 is the mass squared of the lepton-antilepton pair. The corrections to the the QED formula introduced by a transition form factor term are shown in fig.60c (dotted line) with detector influence not taken into account. In the following studies we analyze only events that are below the regime were the transition form factor plays a role (roughly above 200 MeV for $\eta \to e^+e^-\gamma$ see fig.60b) so its details will be not discussed here. For more details about the transition form factor simulation see 6.3.3.

5.2 The $pp \to pp(\eta \to e^+e^-\gamma)$ Reaction Simulation

The $pp \to pp(\eta \to e^+e^-\gamma)$ reaction have been simulated using the phase space model of production and η meson two-body decay into dilepton and real photon. The dilepton mass

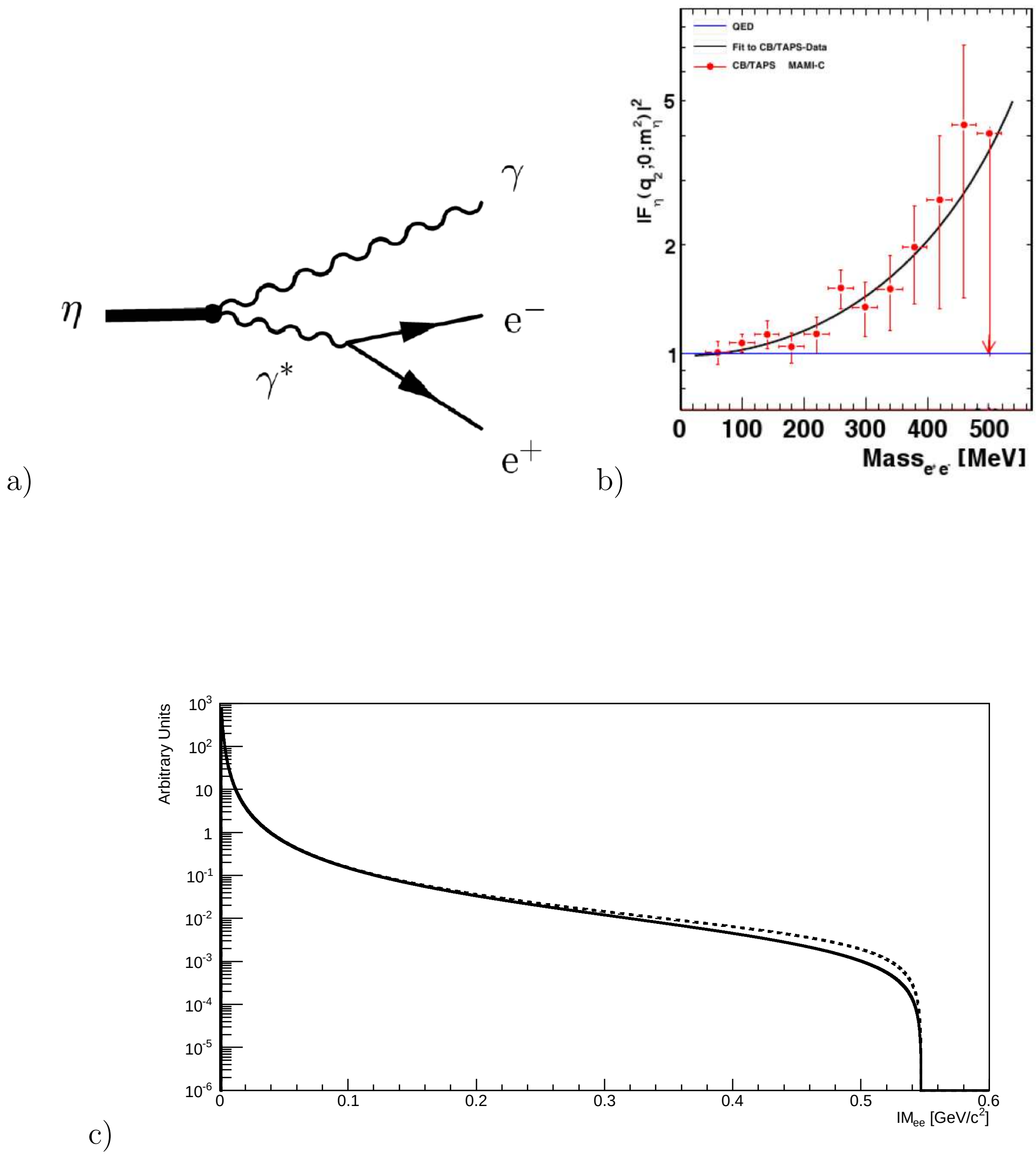

Figure 60: *a) Feynman diagram showing the $\eta \rightarrow e^+e^-\gamma$ single Dalitz decay in the framework of QED theory. b) The squared transition form factor of the η meson plotted as a function of the lepton-antilepton pair mass and the results of the CB/TAPS measurement of the $\eta \rightarrow e^+e^-\gamma$ decay. c) The expected in QED e^+e^- mass distribution using equation 17 (solid line) and calculated with η form factor (dotted line) using single-pole formula 19.*

was probed using the formula 17 from QED distribution under assumption that the η meson is point-like particle [60]. The simulation also included the transition form factor (of the form shown in equation 19) which don't play an important role for $IM_{ee} < 200\ MeV$ so it will be not discussed here. For more information about the transition form factor simulation see previous subsection and subsection 6.3.3.

5.3 Time Cuts and Particle Multiplicities

Meanwhile the check if using energy trigger one can see more pronounced decay channel of the η meson into virtual photon and real photon was performed. This channel also can serve as a experimental field for checking the detector response to e-p pairs with a wide range of invariant masses. Below the list of cuts used to select this decay channel is shown:

- Two or more charged tracks in the Forward Detector. Multiplicity of those track for data and Monte Carlo simulation for $\eta \to \gamma\gamma$ is shown on fig.61.

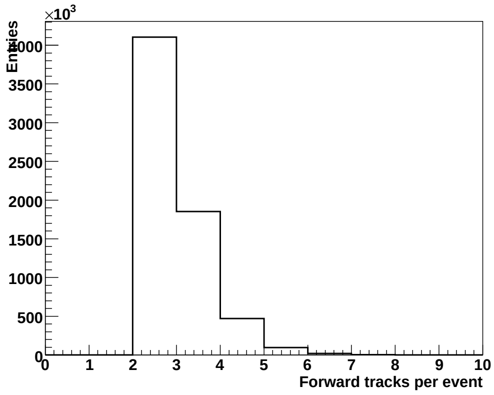

a)

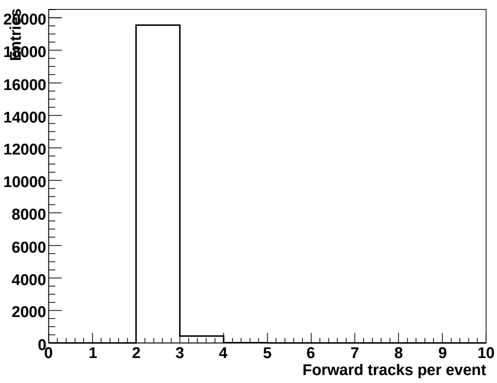

b)

Figure 61: *Charged tracks multiplicity in the Forward Detector per event: a) data and b)* $\eta \to e^+e^-\gamma$ *simulation.*

- At lest two Central Detector charged particles, where at least one is positively charged and at least one is negatively charged. Number of those tracks for data and Monte Carlo simulation for $\eta \to e^+e^-\gamma$ is shown on fig.62.
- One or more neutral track in the Central Detector. Multiplicity of those tracks for data and Monte Carlo simulation for $\eta \to e^+e^-\gamma$ is shown on fig.63.
- The two charged tracks in the Forward Detector closest in time within theta angular range of 3°-18° and emitted with the time difference less than 20ns (see fig.64 for the time difference distribution for those tracks) were selected.
- We request two charged particles of opposite sign giving the smallest opening angle between them in the XY plane. This angle is strongly correlated to invariant mass of particles and the XY plane was chosen because of better reconstruction of charged tracks in this plane. The correlation plot between opening angle in the XY plane and

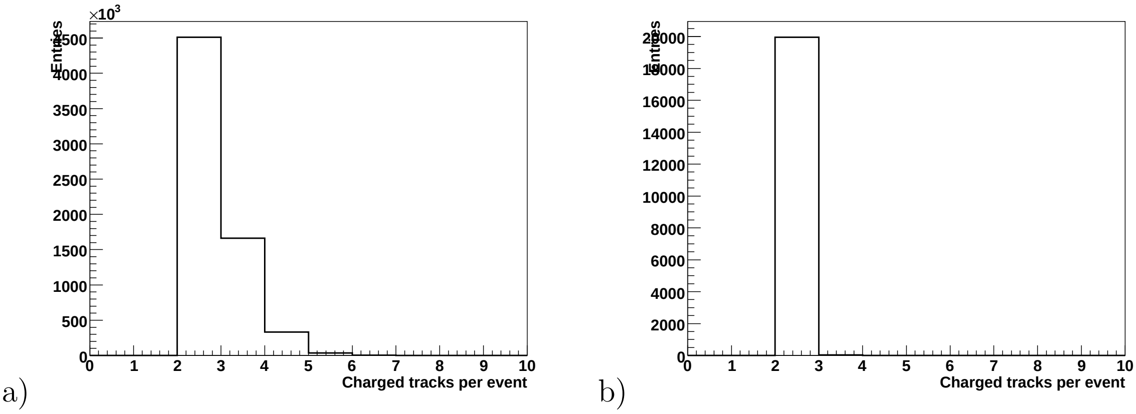

Figure 62: *Charged tracks multiplicity in the Central Detector per event: a) data and b)* $\eta \to e^+e^-\gamma$ *simulation.*

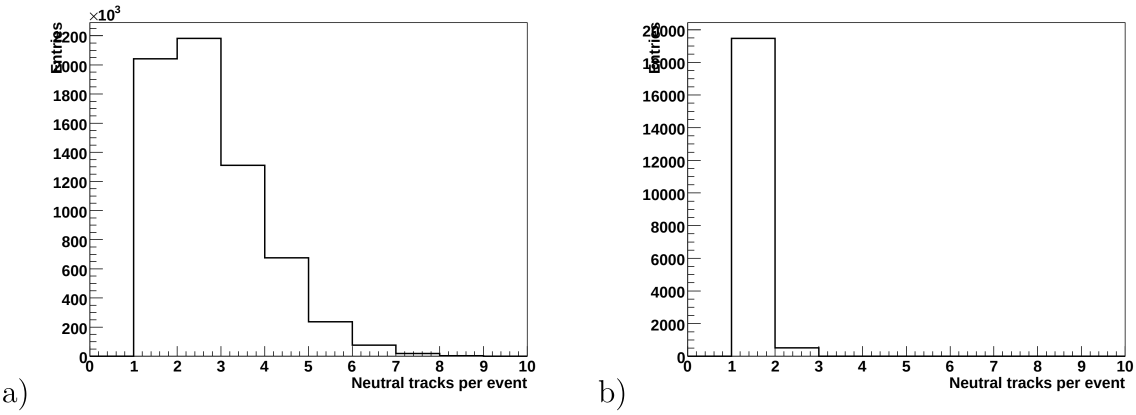

Figure 63: *Neutral tracks multiplicity in the Central Detector per event: a) data and b)* $\eta \to e^+e^-\gamma$ *simulation.*

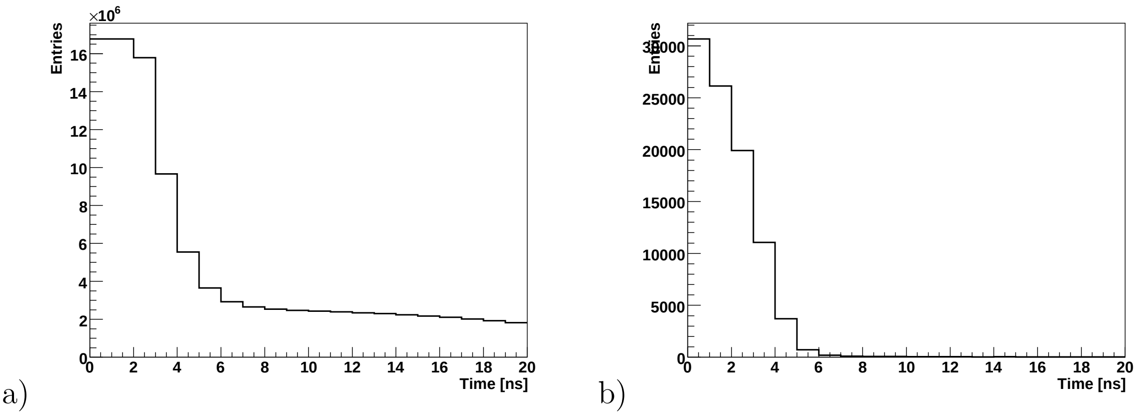

Figure 64: *Time difference between charged tracks in the Forward Detector: a) data and b)* $\eta \to e^+e^-\gamma$ *simulation.*

invariant mass of electron-positron pair for both data candidates and Monte Carlo simulation of $\eta \rightarrow e^+e^-\gamma$ channel is shown in fig.65.

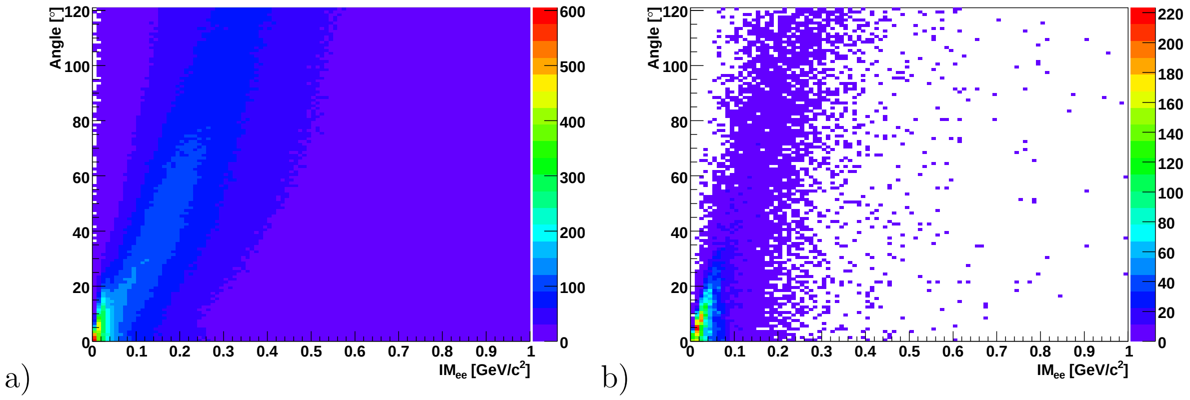

Figure 65: *Emission angle between selected two charged tracks in the central detector in the XY plane versus invariant mass of electron-positron pair: a) data and b) $\eta \rightarrow e^+e^-\gamma$ simulation.*

- Those tracks have to be emitted in [-25,+35]ns bounds around mean time of two Forward Detector charged tracks found in previous step (see fig.66 for the time difference distribution for those tracks).

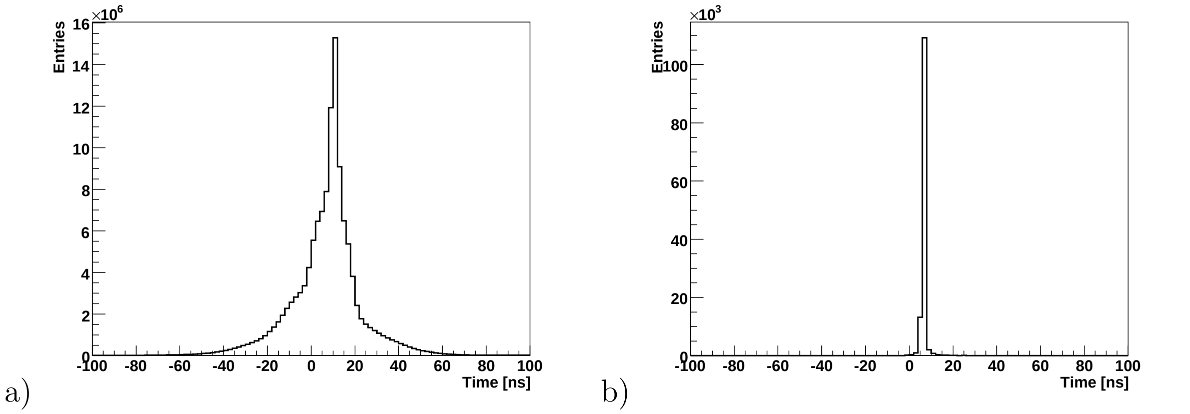

Figure 66: *Time difference between mean time of charged tracks in the Forward Detector and charged tracks in the Central Detector: a) data and b) $\eta \rightarrow e^+e^-\gamma$ simulation.*

- In addition the time difference between the two Central Detector charged tracks cannot be greater than 50ns (see fig.67 for the time difference distribution for those tracks) and there have be a Plastic Scintillator hit in time interval of 100ns around each of this Central Detector charged track. The correlation between charged tracks in the Central Detector and hits in the Plastic Scintillator is shown in fig.68.

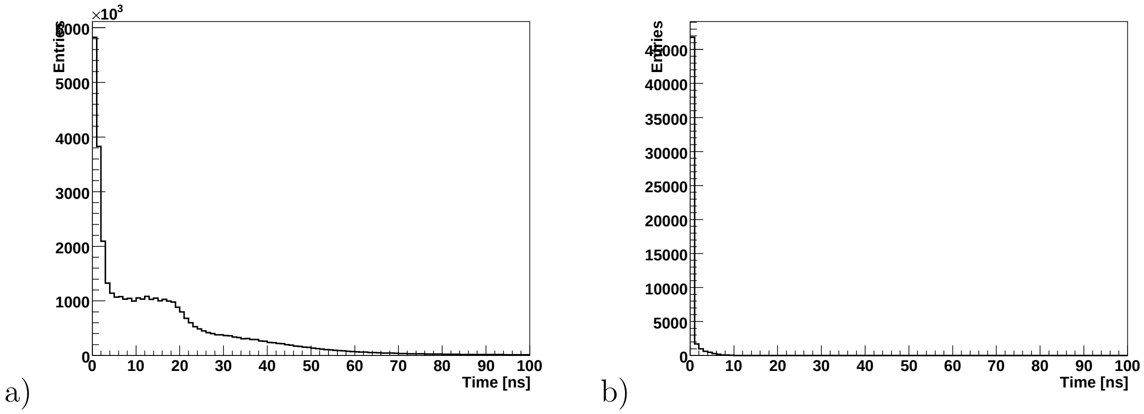

Figure 67: *Time difference between charged tracks in the Central Detector: a) data and b)* $\eta \rightarrow e^+e^-\gamma$ *simulation.*

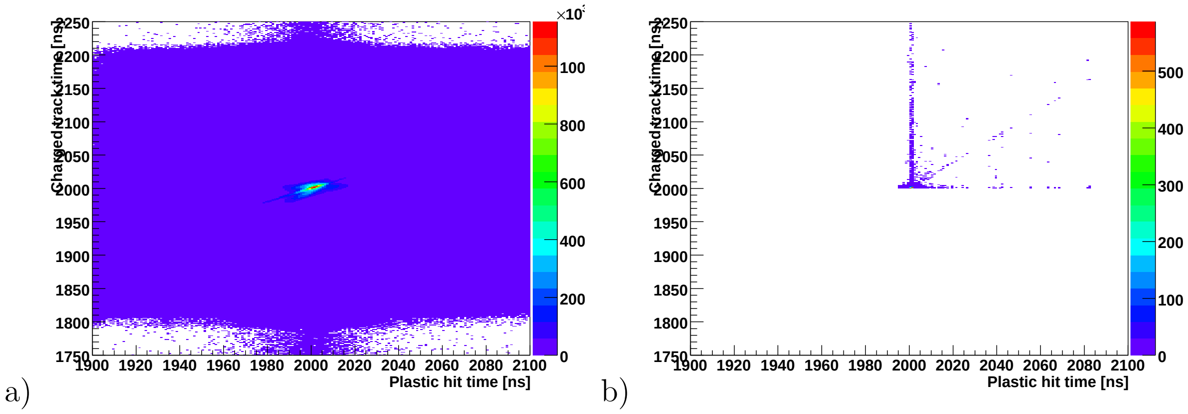

Figure 68: *Time correlation between charged tracks in the Central Detector and Plastic Scintillator hits: a) data and b)* $\eta \rightarrow e^+e^-\gamma$ *simulation.*

- We request one neutral particle giving the greatest opening angle in the XY plane to electron-positron pair, found in previous step. This is an approximation of back-to-back emission of the two photons, one virtual and one real, from the eta meson decay in the CM system - see fig.69.

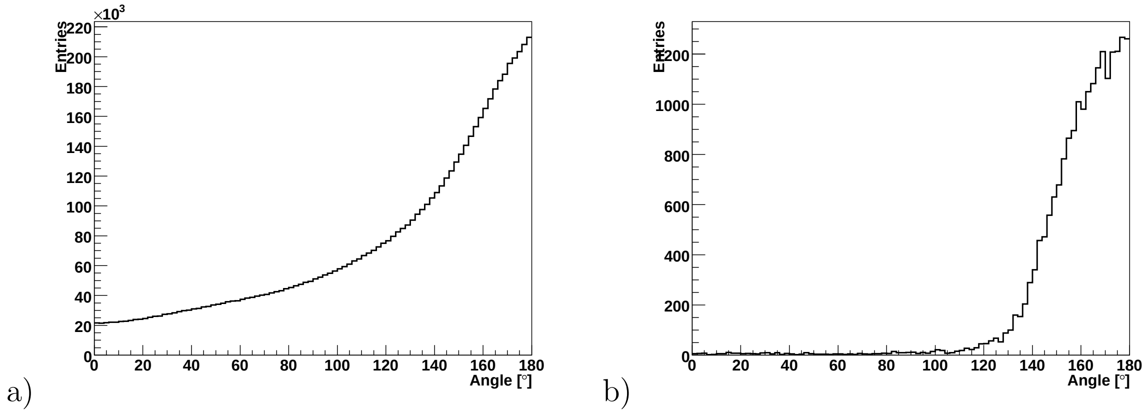

Figure 69: *Opening angle in the XY plane between selected two charged tracks in the central detector and one neutral track: a) data and b) $\eta \to e^+e^-\gamma$ simulation.*

- The neutral tracks have to be emitted in [-25,+35]ns bounds around mean time of two Forward Detector charged tracks found in previous step - see fig.70 for the time difference distribution for those tracks.

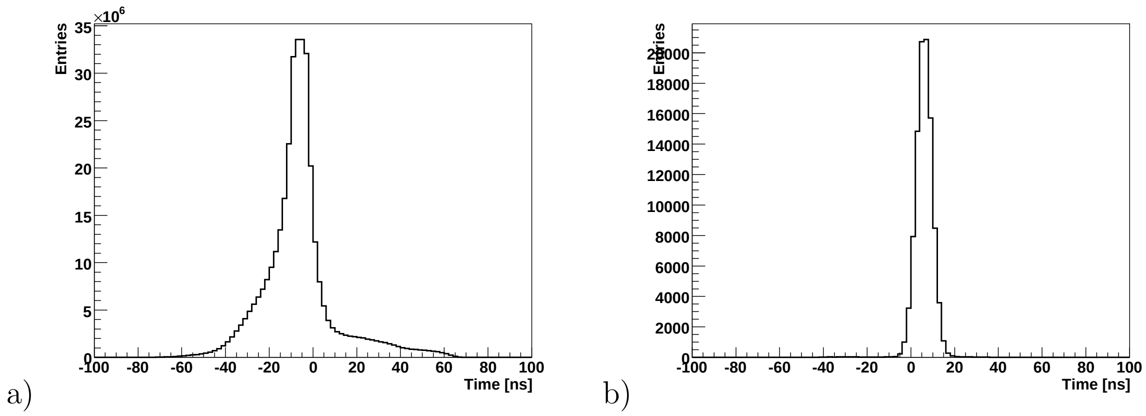

Figure 70: *Time difference between the mean time of charged tracks in the Forward Detector and neutral tracks in the Central Detector: a) data and b) $\eta \to e^+e^-\gamma$ simulation.*

- Each Central Detector track have to be in the proper theta angle interval to mimic the trigger conditions for Monte Carlo data sample (for more information about trigger see section 3.3).

The distribution of IM_{ee} after the selection criteria listed above is shown in fig.71. The enhance at small masses is connected to Dalitz decays of π° and η mesons as well as external conversion of photons in the detector material.

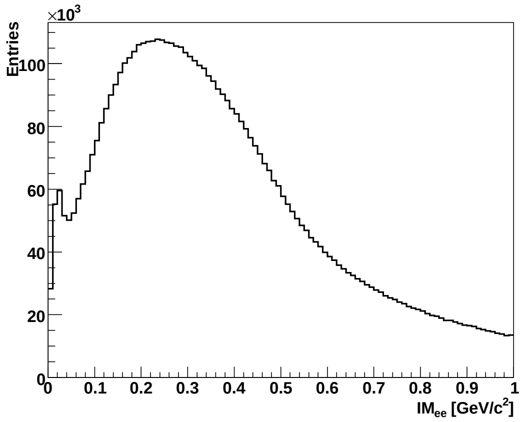

Figure 71: *Invariant mass of electron-positron pair before $\eta \rightarrow e^+e^-\gamma$ channel selection.*

5.4 Selection

In fig.72 one can see the invariant mass of $e^+e^-\gamma$ as a function of missing mass of two protons for events in data with a restriction of small invariant masses of electron-positron pairs (< 0.125 GeV).

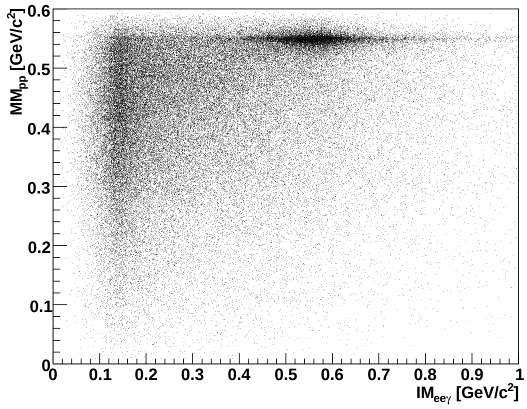

Figure 72: *Missing mass of two protons as a function of invariant mass of $e^+e^-\gamma$ for events in data with a restriction of small invariant masses of electron-positron pairs in $\eta \rightarrow e^+e^-\gamma$.*

I order to select events from this decay channel more precisely we introduce the following cuts:

- Missing mass of two protons in the range of 0.5 - 0.6 GeV - see fig.73
- Invariant mass of e-p pair < 0.125 GeV - see fig.74
- Angle between electron and positron less then 60°- see fig.75
- Emission angle of eta < 30°- see fig.76

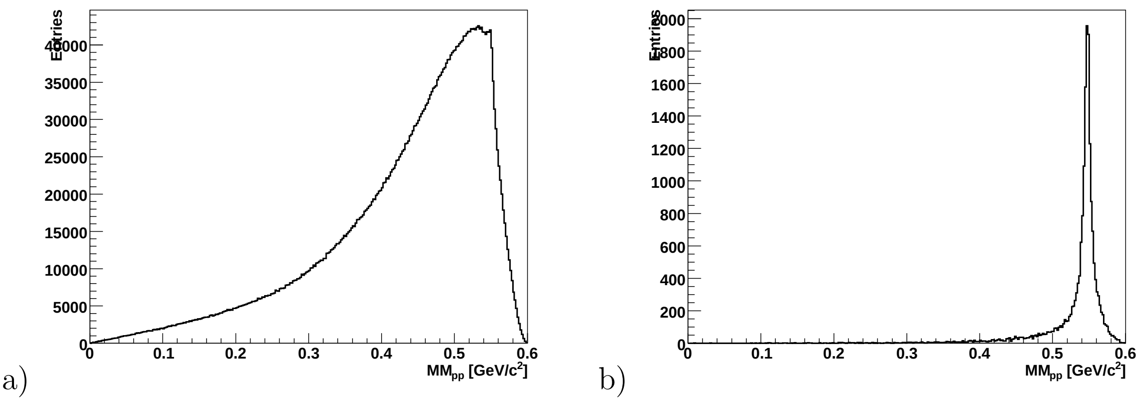

Figure 73: *Missing mass of two protons: a) data and b) $\eta \to e^+e^-\gamma$ simulation.*

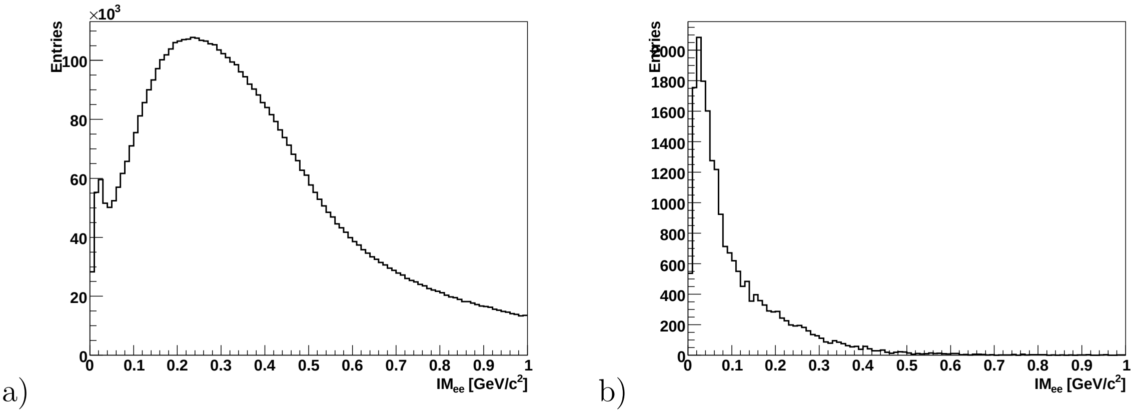

Figure 74: *Invariant mass of electron-positron pair: a) data and b) $\eta \to e^+e^-\gamma$ simulation.*

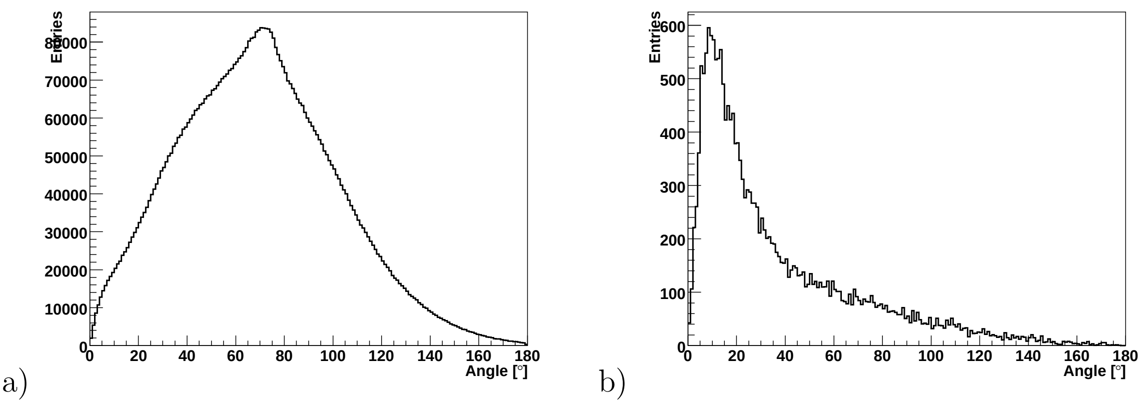

Figure 75: *Opening angle between electron and positron in the LAB frame: a) data and b) $\eta \to e^+e^-\gamma$ simulation.*

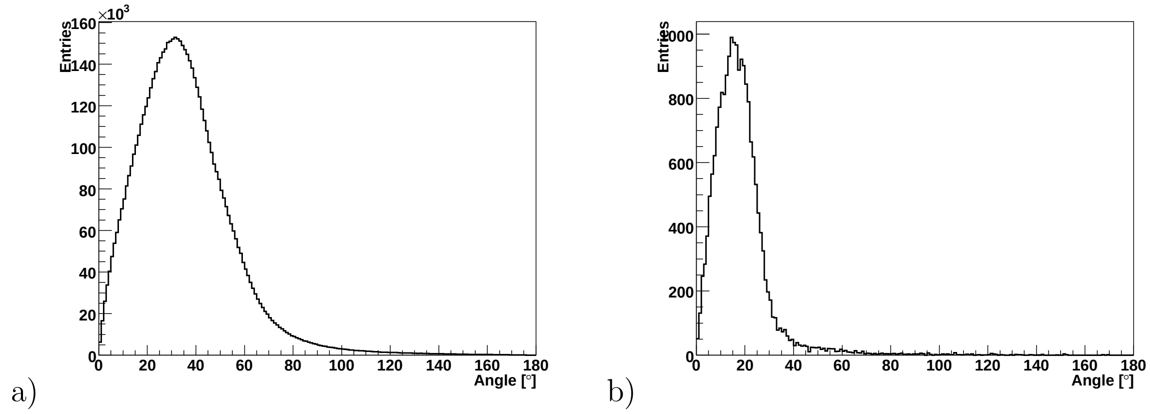

Figure 76: *Emission angle of the η meson in the LAB frame: a) data and b) $\eta \to e^+e^-\gamma$ simulation.*

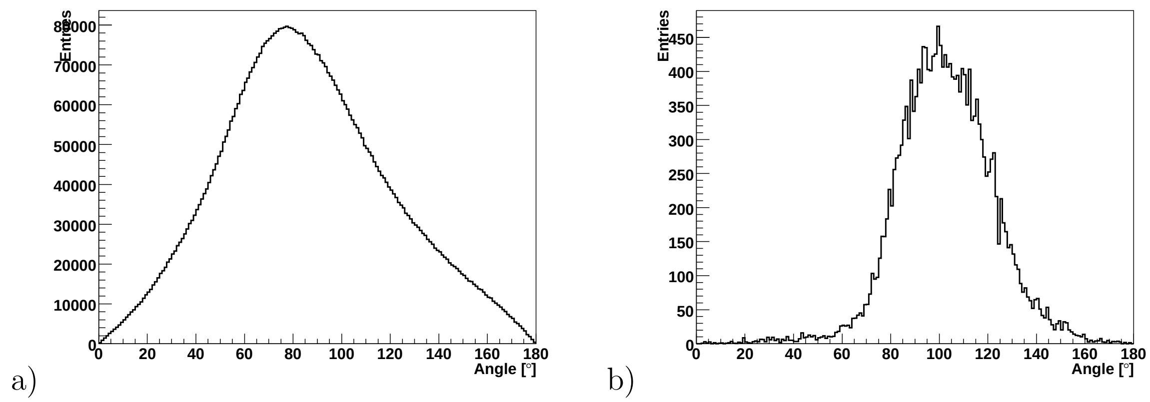

Figure 77: *Opening angle between electron-positron pair and photon in the LAB frame: a) data and b) $\eta \to e^+e^-\gamma$ simulation.*

- Angle between e-p pair and photon in the range of 70°-140°- see fig.77
- Missing mass to e-p pair and photon in the range of 1.6 - 2.2 GeV - see fig.78

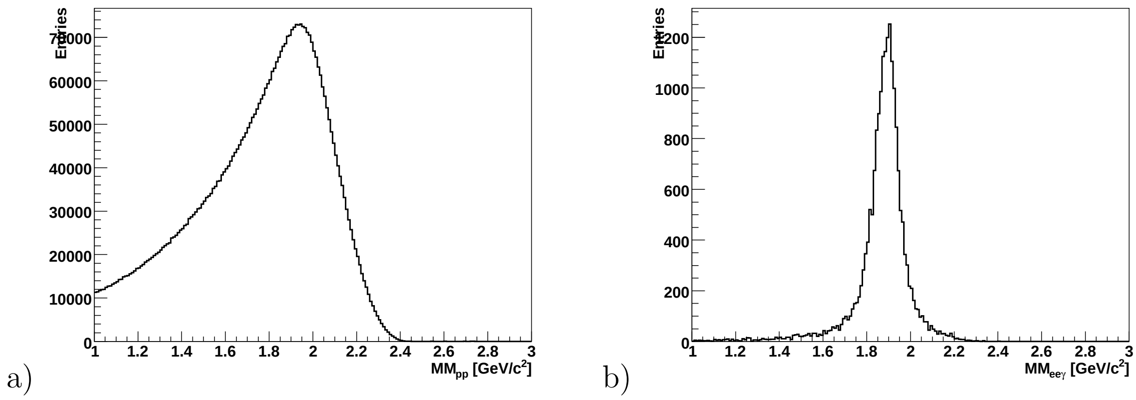

Figure 78: *Missing mass of electron-positron pair and photon distribution: a) data and b)* $\eta \rightarrow e^+e^-\gamma$ *simulation.*

- At least one track identified as an electron by ratio R=momentum/deposited energy, R < 1.65 - see fig.79

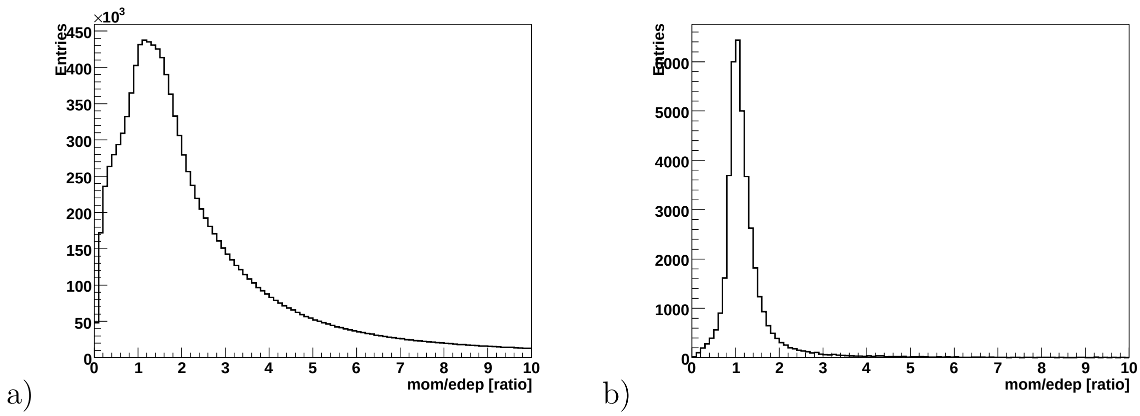

Figure 79: *Identification plot of ratio R equal to momentum divided by deposited energy: a) data and b)* $\eta \rightarrow e^+e^-\gamma$ *simulation.*

- Conversion reduction cut on vertex distance less then 30 mm and invariant mass of e^+e^- pair calculated on the position of the beam pipe less than 10 MeV (for more information on the conversion see section 3.5)
- Trigger effects cut (energy deposit in each half of SEC > 150 MeV and at least one particle in each half of the central detector) - see fig.80

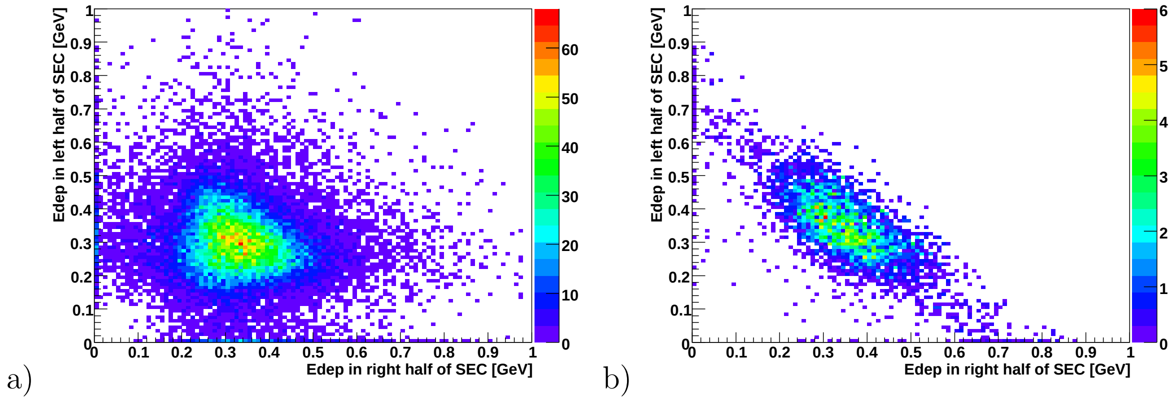

Figure 80: *Energy deposits in each half of the Electromagnetic Calorimeter: a) data and b) $\eta \to e^+e^-\gamma$ simulation.*

5.5 Simulated Background Channels

The list of simulated channels with Branching Ratios for η and π° decays taken from [3] and cross-sections for direct pion production is collected in table tab.8.

Reaction channel	BR or CS at 1.4 GeV	Acc select	Final N_{ev}
$pp \to pp\eta$	$9.8 \pm 1.0\ \mu b$ [55]	—	—
$\eta \to e^+e^-\gamma$	$6.9 \cdot 10^{-3}$ [3]	5.82%	7887
$\eta \to \gamma\gamma$	39.31% [3]	0.07%	596
$\eta \to \pi^+\pi^-(\pi^\circ \to \gamma\gamma)$	22.74% [3]	0.47%	138
$\eta \to \pi^+\pi^-(\pi^\circ \to e^+e^-\gamma)$	$22.74\% * BR(\pi^0_D)$ [3]	1.02%	3
$\eta \to (3\pi^\circ \to \gamma\gamma)$	32.57% [3]	0.06%	0
$\eta \to (2\pi^\circ \to \gamma\gamma)(\pi^\circ \to e^+e^-\gamma)$	$32.57\% * BR(\pi^0_D)$ [3]	2.31%	44
$\eta \to \pi^+\pi^-\gamma$	4.60% [3]	0.56%	145
$pp \to pp\pi^+\pi^-$	$2\ mb$ [59, 57]	0.07%	0
$pp \to pp\pi^+\pi^-(\pi^\circ \to \gamma\gamma)$	$4.6 \pm 1.2^{-0.9}_{+0.7}\ \mu b$ [38]	0.39%	0
$pp \to pp\pi^+\pi^-(\pi^\circ \to e^+e^-\gamma)$	$4.6 \pm 1.2^{-0.9}_{+0.7} * BR(\pi^0_D)\ \mu b$ [38]	0.76%	113
$pp \to pp(3\pi^\circ \to \gamma\gamma)$	$0.8 \pm 0.2^{-0.2}_{+0.1}\ \mu b$ [56]	0.03%	0
$pp \to pp(2\pi^\circ \to \gamma\gamma)(\pi^\circ \to e^+e^-\gamma)$	$0.8 \pm 0.2^{-0.2}_{+0.1} * BR(\pi^0_D)\ \mu b$ [56]	1.30%	52
$\pi^\circ_D = \pi^\circ \to e^+e^-\gamma$	1.174% [3]	—	—

Table 8: *Monte Carlo simulated signal and background samples with corresponding Branching Ratios (BR) and Cross-Sections (CS) for particular channel. ,,Acc select" stands for acceptance after particle selection and time cuts and ,,Final N_{ev}" indicates the number of events expected from a certain reaction after all selection criteria including kinematical cuts.*

5.6 Final Distributions for the $e^+e^-\gamma$ Decay

We divide the invariant mass distribution of $e^+e^-\gamma$ into two classes - one with exactly one high energy photon and any number of low energetic photons and the second one with more than one high energy neutral track in the Central Detector. In the fig.81a one can see invariant mass of $e^+e^-\gamma$ distributions for both classes plotted without the condition on number of high energy photons. The plot with more than one high energy neutral track doesn't show a maximum at the mass of $\eta \to e^+e^-\gamma$ decay. Moreover the invariant mass of the photon chosen for the analysis and the second one is showing the maximum at the π° mass, which is shown in the fig.81b. Due to that fact for further analysis only events with exactly one high energy neutral track in the Central Detector were chosen.

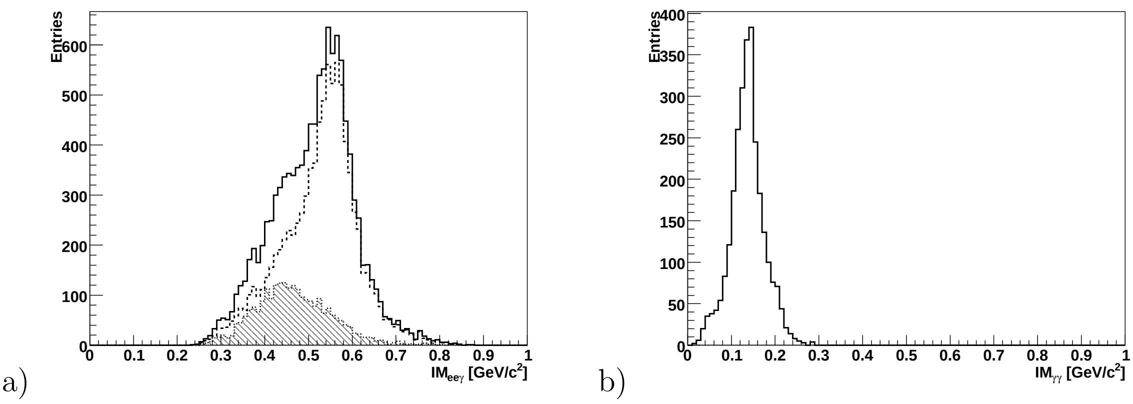

Figure 81: *a) Invariant mass of $e^+e^-\gamma$ for events with: any number of high energy photons (solid line), exactly one high energy photon (dashed line), more than one high energy photon (filled histogram). In the figure b) the invariant mass of photons from the class where we have more than one energetic photon is shown.*

The decomposition of invariant mass of electron-positron pair (see fig.83), invariant mass of $e^+e^-\gamma$ (see fig.82) and missing mass of two protons (see fig.84) are shown in appropriate pictures. Normalization is based on the total number of η mesons produced obtained from $\eta \to \gamma\gamma$ analysis (see section 4). The same notation is used for those three pictures: data is shown as points with statistical error only, black solid line is sum of Monte Carlo cocktail (signal plus background), green solid line indicates simulated $\eta \to e^+e^-\gamma$ signal contribution, and blue solid line shows background from direct pion production and eta meson decays other than $\eta \to e^+e^-\gamma$. The plots show that the reconstruction parameters for data are not exactly matching the ones used in Monte Carlo simulations. Moreover the generated spectra of invariant mass of $e^+e^-\gamma$ don't have a tail left to the η meson mass, which can be due to pileup events that were not taken into account in the simulations.

Two attempts were made to check if the observed number of $e^+e^-\gamma$ events fits the one expected assuming the N_η obtained from $\eta \to \gamma\gamma$. In the first, we assume that all events in the final distribution of invariant mass of $e^+e^-\gamma$ (see fig.82) are the signal events. After taking into account the Branching Ratios and signal content in Monte Carlo cocktail it leads to $N_\eta = 5.59 \cdot 10^7$. But on the other hand we expect that most of events located left side to the η meson peak in the plot of invariant mass of $e^+e^-\gamma$ are connected to the unknown

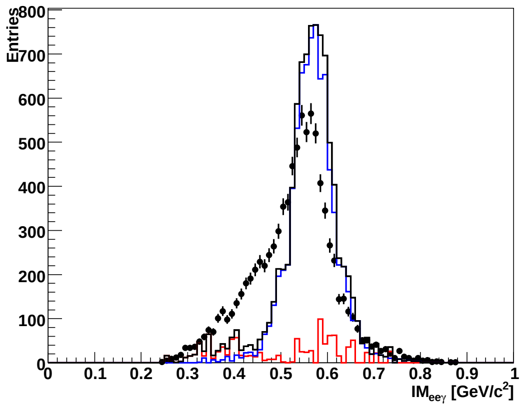

Figure 82: *Invariant mass of $e^+e^-\gamma$ for the final selection of the $\eta \to e^+e^-\gamma$ channel. Data is shown as points with statistical error only, black solid line is sum of Monte Carlo cocktail, blue solid line indicates simulated $\eta \to e^+e^-\gamma$ signal contribution, and red solid line shows background from direct pion production and eta meson decays other than the $\eta \to e^+e^-\gamma$.*

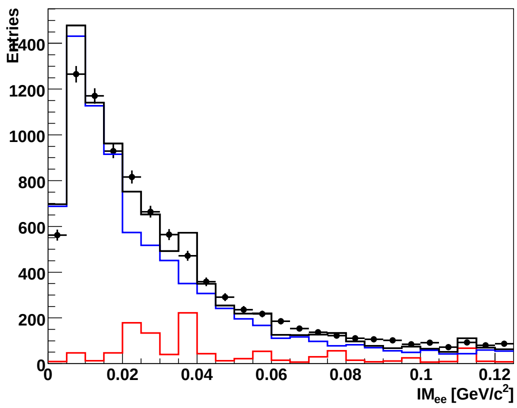

Figure 83: *Invariant mass of electron-positron pair for the final selection of the $\eta \to e^+e^-\gamma$ channel. Data is shown as points with statistical error only, black solid line is sum of Monte Carlo cocktail, blue solid line indicates simulated $\eta \to e^+e^-\gamma$ signal contribution, and red solid line shows background from direct pion production and eta meson decays other than the $\eta \to e^+e^-\gamma$.*

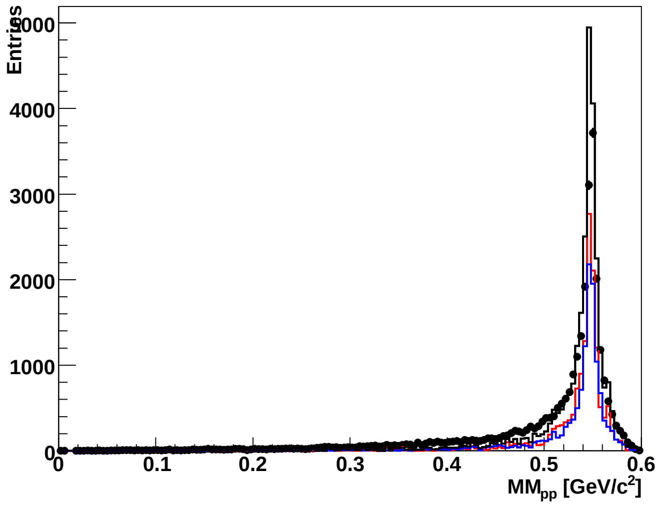

a)

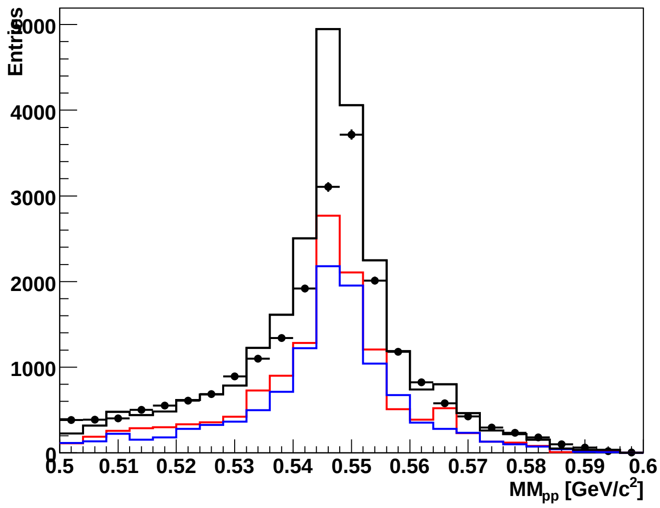

b)

Figure 84: *Missing mass of two protons for the final selection of the* $\eta \to e^+e^-\gamma$ *channel. Data is shown as points with statistical error only, black solid line is sum of Monte Carlo cocktail, blue solid line indicates simulated* $\eta \to e^+e^-\gamma$ *signal contribution, and red solid line shows background from direct pion production and eta meson decays other than the* $\eta \to e^+e^-\gamma$*. Right picture shows the same distribution with zoom to the area of* η *meson mass.*

background contribution or possibly the contribution from pile-ups (see fig.81b). Expected background from channels with charged pions misidentified as electrons or channels with π°'s are also located in the area on the left side of the η meson mass. Due to that the second check were performed when only the right hand side of the η meson peak in the plot of invariant mass of $e^+e^-\gamma$ (in the interval of 0.56-0.8 GeV) were used to fit the expected from Monte Carlo simulations signal plus background shape. The results of this fit are shown in fig.85 and corresponding to it the total number of η mesons produced is equal to $4.94 \cdot 10^7$.

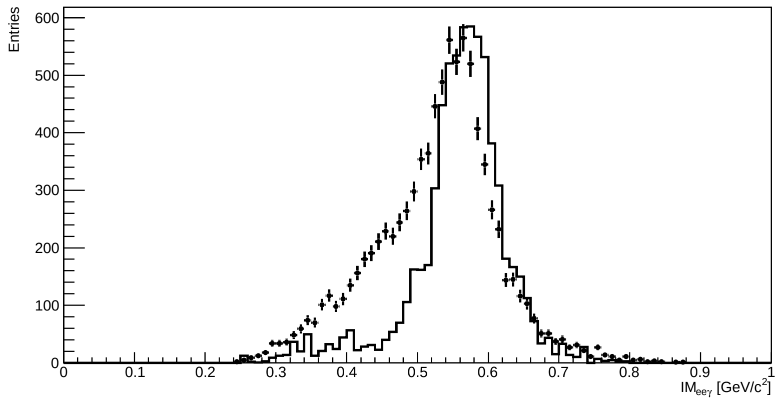

Figure 85: *Invariant mass of* $e^+e^-\gamma$ *for the final selection of the* $\eta \to e^+e^-\gamma$ *channel. Data is shown as points with statistical error only and black solid line is the fit of sum of Monte Carlo cocktail of signal and background channel. The fit area used only the right side of* $IM_{ee\gamma}$ *distribution.*

These numbers are in agreement within less then 15% error with total number of η mesons produced obtained from $\eta \to \gamma\gamma$ analysis shown in section 4. For example $\overline{N}_\eta$ from $\eta \to \gamma\gamma$ decay channel is $\overline{N}_{gg} = 5.91 \cdot 10^7$, the $\overline{N}'_\eta$ from $\eta \to e^+e^-\gamma$ decay channel is $\overline{N}_{eeg} = 5.27 \cdot 10^7$, so $\triangle\overline{N}_\eta = \overline{N}_{gg} - \overline{N}_{eeg} = 0.64 \cdot 10^7$, which is 12% of the $\overline{N}_{eeg}$.

6 Search for $pp \to pp(\eta \to e^+e^-)$ Reaction

6.1 The $\eta \to e^+e^-$ Signature

The $\eta \to e^+e^-$ decays of η meson have it's own very distinctive characteristic. It involves two body decay of a high mass particle into single electron-positron pair with an opening angle in the center of the mass equal to 180°. At our incident proton energy of 1.4 GeV this angle transforms to $\sim$ 100° because of the boost at the laboratory frame. Each decay particle takes roughly half of available energy of $\sim$ 300 MeV on average and stops in the material of the electromagnetic calorimeter. The eta mesons are tagged by the observation of the two charged particles in the forward detector (within θ range of $3° - 18°$. The electrons and positrons are tracked inside the central detector. In the central detector we measured the momenta of particles with the drift chamber, collect the energy deposits with the electromagnetic calorimeter and check if the particle has a charge using the plastic barrel in between the above detectors.

Here we want to compare the most of the studied characteristics of $\eta \to e^+e^-$ decays with the direct two charged pion production which is the one of the background channels for this decay. All histograms in this subsection are plotted after reconstruction and particle selection, taking into account detector acceptance. We assumed here the electron masses for the charged particles in the central detector.

In the fig.86 the missing mass of two protons is shown, where for the signal a clear peak around the eta meson mass at $\sim$ 547 MeV is visible, and for the direct production the distribution has a continuous behavior in the η meson mass range.

a) 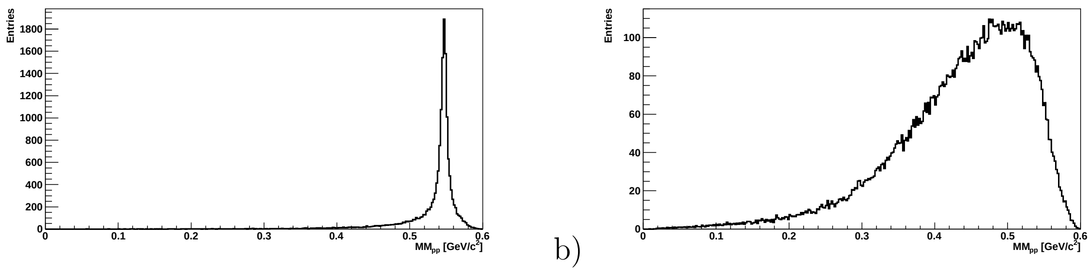

Figure 86: *Missing mass of two protons after reconstruction: a) $\eta \to e^+e^-$ simulation and b) $pp \to pp\pi^+\pi^-$ simulation.*

In the fig.87 the invariant mass of electron-positron pair is shown, where for the signal simulation a bump near the eta meson mass is seen and again a continuous shape for the direct production is visible. In the signal simulation the tails are connected to the events in which the reconstruction algorithm provides us a wrong momenta of the high energy electron(s). The reason for such unprecise reconstruction is that charged particles with high momenta have small track curvature.

In the fig.88 the opening angle between electron and positron is drown, where the signal events are concentrated around $\sim$ 100° and the direct production occupies the whole available range.

In the fig.89 the ratio between the particle momentum and the energy deposited in the electromagnetic calorimeter is shown, where for the signal tracks - electrons and positrons

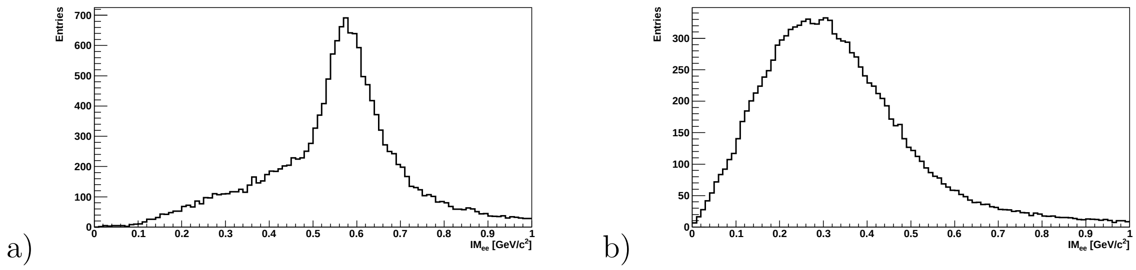

Figure 87: *Invariant mass of electron-positron pair after reconstruction: a) $\eta \to e^+e^-$ simulation and b) $pp \to pp\pi^+\pi^-$ simulation.*

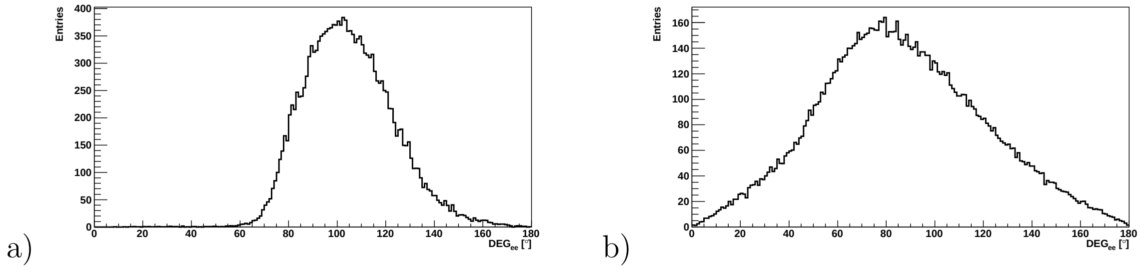

Figure 88: *Opening angle of electron-positron pair after reconstruction: a) $\eta \to e^+e^-$ simulation and b) $pp \to pp\pi^+\pi^-$ simulation.*

this ratio should be close to one, due to very low mass and small cascade length in comparison to charged pions.

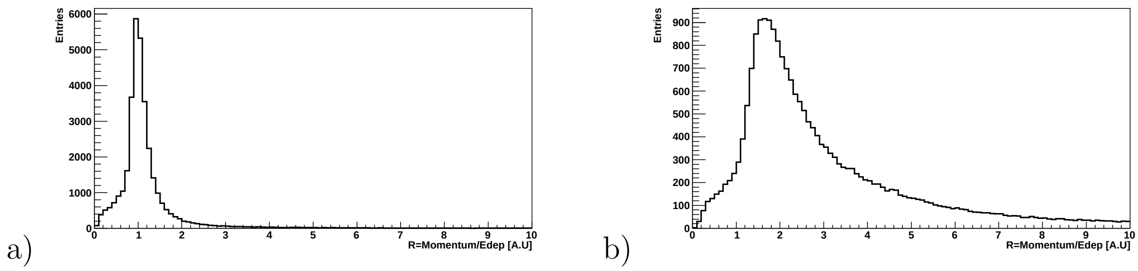

Figure 89: *Ratio between the particle momentum and it's deposited energy after reconstruction: a) $\eta \to e^+e^-$ simulation and b) $pp \to pp\pi^+\pi^-$ simulation.*

In the fig.90 the correlation plot between energy deposit in the electromagnetic calorimeter of one charged track in the central detector is shown versus the other one. The high energy electrons and positrons leave most of its energy in the electromagnetic calorimeter. Fast pions (of energy $> \sim 170\ MeV$ are frequently leaving the detector and therefore depositing only part of their energy.

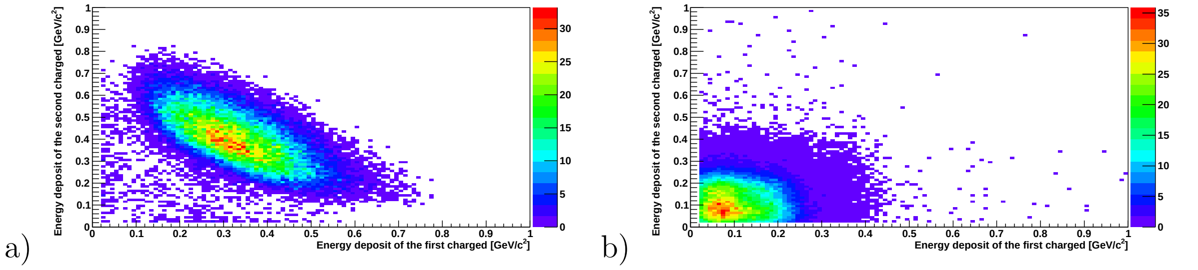

Figure 90: *Deposited energy of both of the central detector charged tracks after reconstruction: a) $\eta \to e^+e^-$ simulation and b) $pp \to pp\pi^+\pi^-$ simulation.*

6.2 Background Reaction Channels to the $\eta \to e^+e^-$ Decay

From the theoretical studies we can establish the three main sources of background reactions for $\eta \to e^+e^-$ decay channel - direct two charged pion production, single Dalitz decay of the η meson with a real photon of very low energy, Dalitz decays of baryonic resonances and combinatorial background.

6.2.1 The $pp \to pp\pi^+\pi^-$

The first important background channel is direct two charged pion production ($pp \to pp\pi^+\pi^-$) due to the fact that cross-section (CS) for this reaction ($\sim$ 1.5 mb) [59, 57] is about 150 times larger then the cross-section for eta meson production ($\sim$ 10 μb) in pp reaction at 1.4 GeV [55]. This channel decay products lead to the same topology as $\eta \to e^+e^-$ decay because of exactly two charged particles in the final state. There are several facts that help us to get rid of this channel. Only a small fraction of events ($\sim 1\%$) for this channel is in the one σ range of the η mass according to the Monte Carlo simulations (see fig.86b). The second fact is that electrons/positrons, if are going into electromagnetic calorimeter, leave almost all of their energy inside it, via electromagnetic shower. Pions on the other hand, if not suffering from nuclear interactions (or are not decaying), are passing through the SEC, leaving only part of their energy. Also we know that the light decay products like e^+e^- pairs carry larger kinetic energy than the pions. Other direct pion production channels don't play an important role as a background due to lower cross-section than direct two charged pion production and also to the fact that they have different number of final state particles then $\eta \to e^+e^-$ decay channel.

6.2.2 The $pp \to pp(\eta \to e^+e^-\gamma)$

The second background to consider is the single Dalitz decay of η meson for the large masses of the virtual photon. The invariant mass of e^+e^- pair produced in this reaction channel can be very large if the virtual photon takes most of the decay energy. In that situation the real gamma produced has very low energy and can easily be undetected or cut off on the threshold values of the detector. It can also be lost in some part of the detector where we cannot measure neutral particles. This situation is rare, but because in this case we have only electron-positron pair with a high mass when assuming that photon was undetected, it is very hard to distinguish it from $\eta \rightarrow e^+e^-$ decay channel because of the same topology. Also those events have very similar kinematics as there were also produced from decay of η meson.

6.2.3 Dalitz Decays of Baryonic Resonances

Dalitz decays of baryonic resonances were found to be an important background due to the same final state particles as in $\eta \rightarrow e^+e^-$ decay channel. It is hard to calculate the amount of background events due to very limited information on cross-section for production of several important channels and rather unknown form factor of Dalitz decays of baryonic resonances in the area of high masses of e^+e^- pairs. The composition plot of $IM_{e^+e^-}$ for various baryonic resonances at the incident proton energy of 1.61 GeV can be found in fig.91 [63] and cross-section for the baryonic resonance cocktail for the energy 1.4 GeV is shown in fig.92 [65].

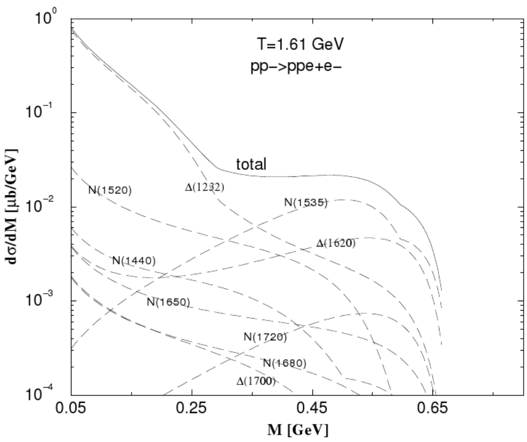

Figure 91: IM_{ee} *cross-section for* $pp \rightarrow pX$ *reaction for the incident proton energy of 1.61 GeV [63].*

In this work we assumed that the main background channel is Dalitz decay of $\Delta(1232)$ in the reaction $pp \rightarrow p(\Delta(1232) \rightarrow pe^+e^-)$ and the cross-section of baryonic resonances around the η meson mass is dominated by this decay. The $\Delta(1232)$ is dominant at this energy and cross-sections for the other baryonic resonances like N(1520), N(1535), $\Delta(1620)$ at 1.4 GeV are lower by at least one order of magnitude and branching ratios for the Dalitz decays are at least at the same order of magnitude.

6.2.4 Combinatorial Background

Another possible background contributing to $\eta \rightarrow e^+e^-$ is combinatorial background. For an estimation of this background the like-sign method can be used. This method looks for the same sign pairs in the data that pass all the same selection criteria as the signal events. The number of combinatorial background events (N_{CB}) can be estimated from the formula:

$$N_{CB} = 2\sqrt{N_{++} \cdot N_{--}}, \tag{20}$$

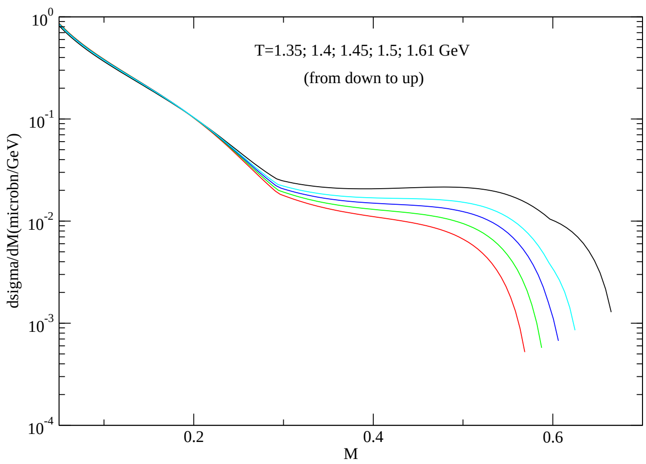

Figure 92: *IM_{ee} cross-section for $pp \to pX$ reaction for various energy of protons [65]. The green line shows the differential cross-section for the energy of incident protons 1.4 GeV.*

where N_{++} and N_{--} is the yield of positively and negatively charged pairs. This formula can be obtained in a following way. Lets assume that in an event we have N pairs with one negatively charged particle and one positively charged particle. The total number of unlike sign combinations that are possible is equal to N^2. But on the other hand to get the number of random combinations only, we have to subtract the pair that come from a real decay. So we have:

$$N_{+-} = N^2 - N = N(N-1) \tag{21}$$

To calculate the number of like-sign combinations, for example for the ++ combinations, we add the number of combinations made by the first positively charged particle, which is equal to a total of $(N-1)$ pairs, then $(N-2)$ created by the second charged particle and so on. Finally the total number of ++ combinations can be express by an equation:

$$N_{++} = (N-1) + (N-2) + ... + [N - (N-1)] + (N-N) \tag{22}$$

where there are N terms. If we change the order of terms it is easy to see that the equation can be simplified to:

$$N_{++} = N \cdot N - (1 + 2 + ... + N) = N^2 - \frac{1}{2}[N(N-1)] = \frac{1}{2}N(N-1) \tag{23}$$

And similarly for N_{--}. The formula 20 is applicable if there are no acceptance or reconstruction effects, either for positively or negatively charged particles. For this we check the 100k Monte Carlo simulations of $\eta \to e^+e^-$ decay channel and the difference is within the statistical error, so we did not consider any correction factor to take such effects into account. The results of this study are shown in table 9.

Most likely this background doesn't come from pileups of events with an another event with charged pair because in this case we should have similar number of N_{++} and N_{--}. In our case we see the majority of N_{++} which can be due to overlapping with $pp \to d\pi^+$, $pp \to pn\pi^+$ or proton-proton elastic scattering reactions which have much higher cross-section in comparison to the η meson production.

The number of events and results obtained using this method are shown in section 7.

N_- negatively charged tracks	78855 ± 281
N_+ positively charged tracks	78393 ± 280
$\|N_- - N_+\|$ difference	462 ± 397

Table 9: *The Monte Carlo derived acceptance study for the tracks of different sign.*

6.3 Monte Carlo Simulations

In order to find out which background is most important in the study of the very rare η meson decay we generated several Monte Carlo data samples for signal as well as background channels:

6.3.1 Signal from the $\eta \to e^+e^-$

The $pp \to pp(\eta \to e^+e^-)$ channel have been generated using a simple phase-space model of three body production of protons and η meson and binary decay of the η meson into the lepton-antilepton pair.

6.3.2 The $pp \to pp\pi^+\pi^-$

Several models for the two charged pion production were considered and generated using the PLUTO event generator:

- $pp \to pp(\rho(770)^0 \to \pi^+\pi^-)$
- $pp \to (\Delta^{++} \to p\pi^+)(\Delta^0 \to p\pi^-)$
- $pp \to pp\pi^+\pi^-$ phase space direct production
- $pp \to pp\pi^+\pi^-$with condition on mass of $\pi^+\pi^-$ equal to the η meson mass to enhance the number of expected events in the area of interest around the η meson mass at $\sim 547\ MeV$

6.3.3 The $pp \to pp(\eta \to e^+e^-\gamma)$

The single Dalitz decay of η mason have been simulated using the following conditions:

- The $IM_{e^+e^-} > 0.3\ GeV$
- The mass distribution according to the assumption that η meson is point-like particle [60]:

$$\frac{d\Gamma_{l^+l^-\gamma}}{dq^2 \cdot \Gamma_{\gamma\gamma}} = \frac{2\alpha}{3\pi q^2}\sqrt{1-\frac{4m_l^2}{q^2}}\left(1+\frac{2m_l^2}{q^2}\right)\left(1-\frac{q^2}{M_P^2}\right), \tag{24}$$

  where l denotes lepton, α is the fine-structure constant, q^2 is the mass squared of the lepton-antilepton pair, m_l stands for the lepton mass, M_P is the mass of pseudoscalar meson

- The form factor using single-pole formula with parameter Λ related to the mass of the vector meson [68]:

$$F(q^2) = \left(1 - \frac{q^2}{\Lambda_P^2}\right)^{-1}, \qquad (25)$$

where $\Lambda_P = 0.73$ and q^2 is the mass squared of the lepton-antilepton pair

This simulation corresponds to less than 2% of $pp \to pp(\eta \to e^+e^-\gamma)$ decay without cut 0.3 GeV on IM_{ee}[66].

6.3.4 Radiative Decay of Baryonic Resonances

The $pp \to p(\Delta(1232) \to pe^+e^-)$ reaction were simulated using PLUTO event generator under the following conditions:

- The mass-dependent width of the Breit-Wigner distribution of the Delta
- The anisotropic (s+p wave) production angle for the $pp \to p\Delta(1232)$ channel
- The dilepton mass for $Delta(1232)$ Dalitz decay using formulas 24 and 25

6.3.5 Summary of Monte Carlo Simulations

The summary of Monte Carlo generated background channel as well as the signal can be found in tab.10. For the most of reactions the PLUTO generator was used, except for the $pp \to pp(\eta \to e^+e^-)$, where phase space model was assumed and $pp \to pp(\eta \to e^+e^-\gamma)$, where events were generated according to formulas 24 and 25.

Reaction channel	N_{ev}	Cross-section	Branching ratio	Remarks
$pp \to pp(\eta \to e^+e^-)$	10^6	10 μb [55]	—	
$pp \to pp\pi^+\pi^-$	10^6	1.5 mb [59, 57]	—	
$pp \to pp\pi^+\pi^-$	10^7	1.5 mb [59, 57]	—	$IM(\pi^+\pi^-)$ equal to the η mass
$pp \to pp(\rho(770)^0 \to \pi^+\pi^-)$	10^5	1 μb [67]	$\sim 100\%$ [3]	
$pp \to (\Delta^{++} \to p\pi^+)(\Delta^0 \to p\pi^-)$	10^5	1.5 mb [59, 57]	—	
$pp \to pp(\eta \to e^+e^-\gamma)$	10^5	10 μb [55]	$7 \cdot 10^{-3}$ [3]	Generated with $IM_{ee} > 0.3$ GeV
$pp \to p(\Delta(1232) \to pe^+e^-)$	10^6	5.5 μb [65]	$4 \cdot 10^{-5}$ [64]	

Table 10: *Summary of Monte Carlo samples used in the $\eta \to e^+e^-$ analysis. N_{ev} - Number of background or signal events generated.*

6.4 Selection of the $\eta \to e^+e^-$ Event Candidates

After reconstruction $\sim 1.5 \cdot 10^8$ events in all preselected files are seen. Further selection introducing following particle number selection cuts and time cuts was applied:

a) 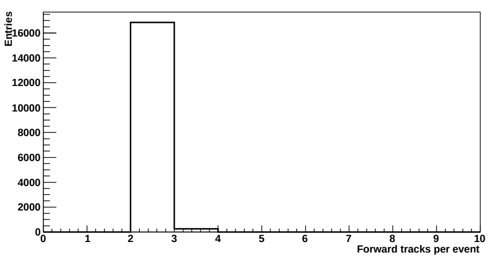

b) 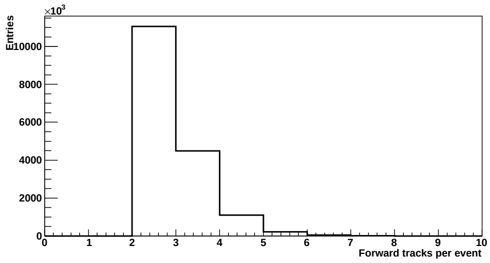

Figure 93: *Forward detector charged tracks multiplicity. a) $\eta \to e^+e^-$ simulation, b) data.*

- Two or more forward detector charged tracks (see fig.93).
- From all forward detector charged tracks we are choosing the two closest in time within theta angular range of 3°-18° and having time difference less than 10ns. The time difference the mean time for all combinations of charged tracks in the forward detector and distribution of time difference for all combination of forward detector charged track can be found in fig.94.

a) 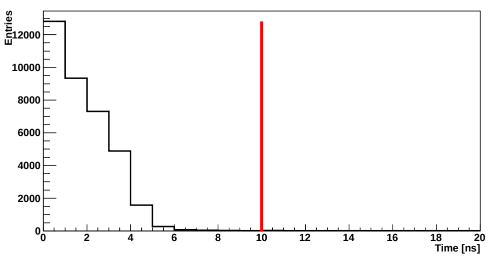

b) 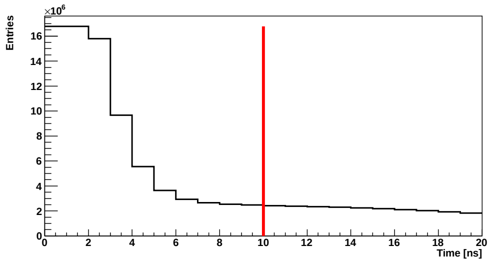

Figure 94: *Time difference distribution for all combinations of charged tracks in the forward detector. a) $\eta \to e^+e^-$ simulation, b) data. The selection condition is shown in red, only events left to the line are accepted.*

- No neutral tracks in the central detector with energy greater then 20 MeV
- Two or more central detector charged tracks, at least one positively and negatively charged (see fig.95).

a) 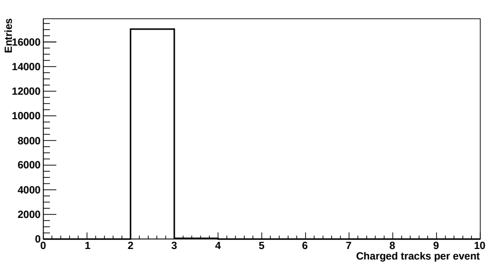

b) 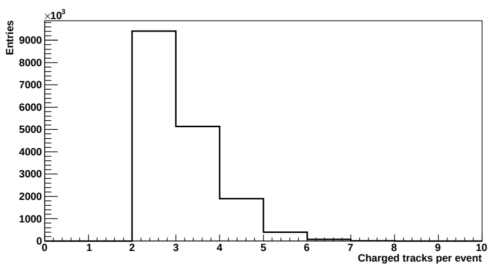

Figure 95: *Central detector charged tracks multiplicity. a) $\eta \to e^+e^-$ simulation, b) data.*

- We request two oppositely charged particles in central detector giving the greatest opening angle between them on the XY plane. For the distribution of the opening angle between electron and positron on the XY plane see fig.96. Those tracks have to be in the time coincidence with previously chosen forward detector charged tracks therefore we are requesting the time difference between 0 and 20 ns (see fig.97). In

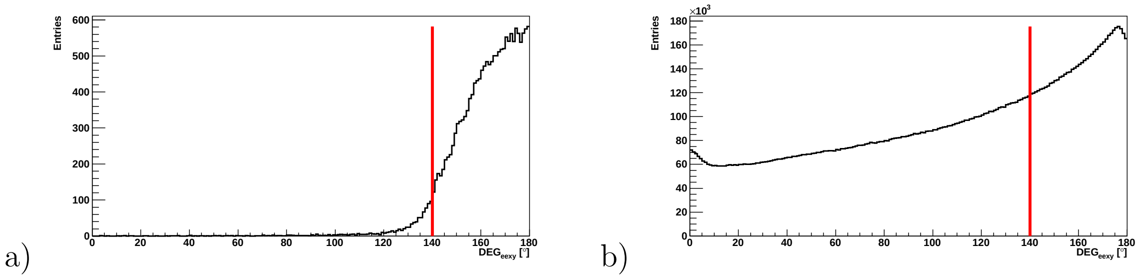

Figure 96: *Opening angle between electron and positron on the XY plane. a) $\eta \to e^+e^-$ simulation, b) data. The selection condition is shown in red, only events right to the line are accepted.*

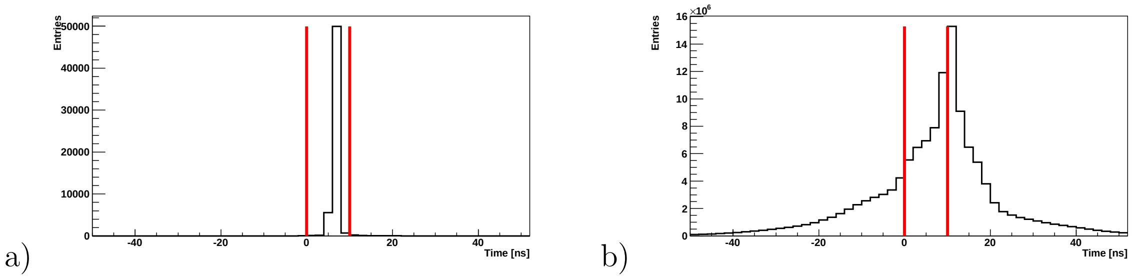

Figure 97: *Time difference between all combinations of charged tracks in the forward detector and the central detector charged tracks. a) $\eta \to e^+e^-$ simulation, b) data. The selection condition is shown in red, only events between the lines are accepted.*

addition time difference between those two central detector charged tracks cannot be greater than 10ns (see fig.98) and there must be at least one plastic barrel hit in time interval of 20ns around each of those central detector charged tracks (see fig.99).

6.5 Cut Optimization

In order to find the best possible values of kinematical and identification cuts to select $\eta \to e^+e^-$ signal events from data, linear optimization of every cut was used. Data and Monte carlo samples were taken after selection (see section 6.4) involving at least two charged particles in the central detector, at least two protons in the forward detector and a number of cleaning time cuts. As an input for optimization procedure four different Monte Carlo simulations were used, where the first one as a signal and three other as a background:

- 100k $\eta \to e^+e^-$

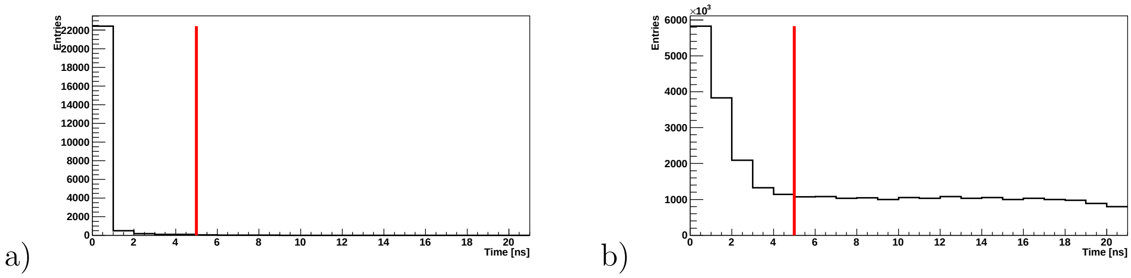

Figure 98: *Time difference distribution for all combinations of charged tracks in the central detector. a) $\eta \rightarrow e^+e^-$ simulation, b) data. The selection condition is shown in red, only events left to the line are accepted.*

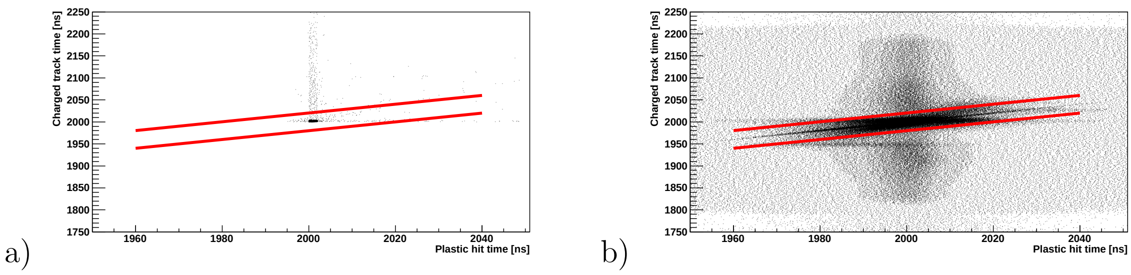

Figure 99: *Time correlation between all times taken from the plastic scintillator detector and time for each charged particle in central detector. a) $\eta \rightarrow e^+e^-$ simulation, b) data. The selection condition is shown in red, only events between the lines are accepted.*

- 100k $\eta \rightarrow e^+e^-\gamma$, where $IM_{ee} > 0.3\ GeV$
- 1 million $pp \rightarrow p(\Delta(1232) \rightarrow pe^+e^-)$
- 1 million $pp \rightarrow pp\pi^+\pi^-$

In this analysis it was decided to chose the form of optimization function in order to provide the smallest branching ratio upper limit. The upper limit formula has the form of:

$$BR_{limit} = \frac{(N_{ev} - N_{bcg}) + \lambda \cdot \sigma_{ev}}{Acc \cdot N_\eta}, \tag{26}$$

where σ_{ev} is the statistical error on number of event candidates, Acc stands for the simulated signal acceptance, and N_η is the total number of η mesons produced obtained in the section 4. If we assume that the term $N_{ev} - N_{bcg}$ is very small the whole equation is proportional to the ratio between the square root of number of events in the final distribution divided by the the efficiency for the signal channel with constant λ and N_η terms (more about the upper limit formula can be found in section 7). Lets define significance was as follows:

$$S = \frac{\sqrt{N_{bg}}}{Acc}, \tag{27}$$

where N_{bg} is estimated from Monte Carlo simulations number of expected events using experimental values for cross-sections and branching rations, *Acc* stands for the sum of geometrical acceptance and detector efficiency for the simulated signal.

More than fifteen different kinematical and identification variables were checked. The list contains:

- Missing mass of all particles
- Invariant mass of e^+e^- pair (IMee)
- Invariant mass of e^+e^- pair and one of the protons
- Angle between electron and positron (DEGee)
- Angle between electron and positron on the XY plane
- Sum of momenta of electron and positron
- Sum of kinetic energy of electron and positron
- Sum of energy deposits of electron and positron (SumEdep)
- Ratio between momentum and energy deposit (Iden)
- Emission angle of eta meson calculated from electron and positron
- Emission angle of eta meson calculated from protons
- Total missing energy

- Total missing momentum
- Total missing angle
- Missing transverse momentum
- Phi angle difference for electron and positron

For the most of possible distributions mentioned above the optimization procedure didn't find extremum due to similar shape of distributions for background sum and signal. The only possible variables to be optimized using this procedure were: invariant mass of electron-positron pair, opening angle between electron and positron in the LAB frame, ratio between particles momentum and it's energy deposit in the electromagnetic calorimeter and sum of energy deposits in electromagnetic calorimeter for both electron and positron. See fig.100, fig.101, fig.102, fig.103 for the comparison between distributions for simulated signal, generated $\pi^+\pi^-$ background channel and data. In the fig.100 the distribution of invariant mass of electron-positron pair as a function of opening angle between electron and positron in the LAB frame is shown. Due to the fact that this two variables are correlated the 2-dim optimization procedure was initialized here. In the calculations all charged tracks were treated as electrons.

The output of optimization algorithm is shown in fig.104 only for the variables for which the maximum can be found. The significance value in 2-dim plot (fig.104c) is shown in colors. The points correspond to the value obtained from the equation 27 for a given cut used in the analysis. The analysis was repeated for each possible value of the cut and from the given distribution the cut value corresponding to the maximum of significance have been obtained. In the analysis the obtained optimized value for the cut on invariant mass of e^+e^- and sum of energy deposits for charged tracks was changed from 0.54 GeV to 0.48 GeV and from 0.64 GeV to 0.55 GeV respectively in order to avoid the systematical effects connected to the fact that the cut will be put in the middle of the distribution.

The results of the described procedure are collected in tab.11. In the table one can find the acceptance before any cuts, its change after introducing one of the cuts obtained from optimization procedure and the final value after all criteria. Those values are shown for simulated signal, three different backgrounds. In addition the reduction factor for data event candidates is shown with the starting number of events and its change after introducing selection criteria, one by one or all at once.

6.6 Analysis of the $\eta \to e^+e^-$ Decay Channel

The following cuts were used in this analysis in addition to conditions described in section 6.4. The value of some of the cuts were obtained by initializing the optimization procedure described in section 6.5. As a remark we have to mention that all charged tracks in the central detector have the electron mass assumed.

- The sum of energy deposits of each of the central detector charged tracks previously selected > 550 MeV (see fig.105)
- Opening angle between the central detector selected charged tracks on the XY plane greater than 140°(see fig.106)

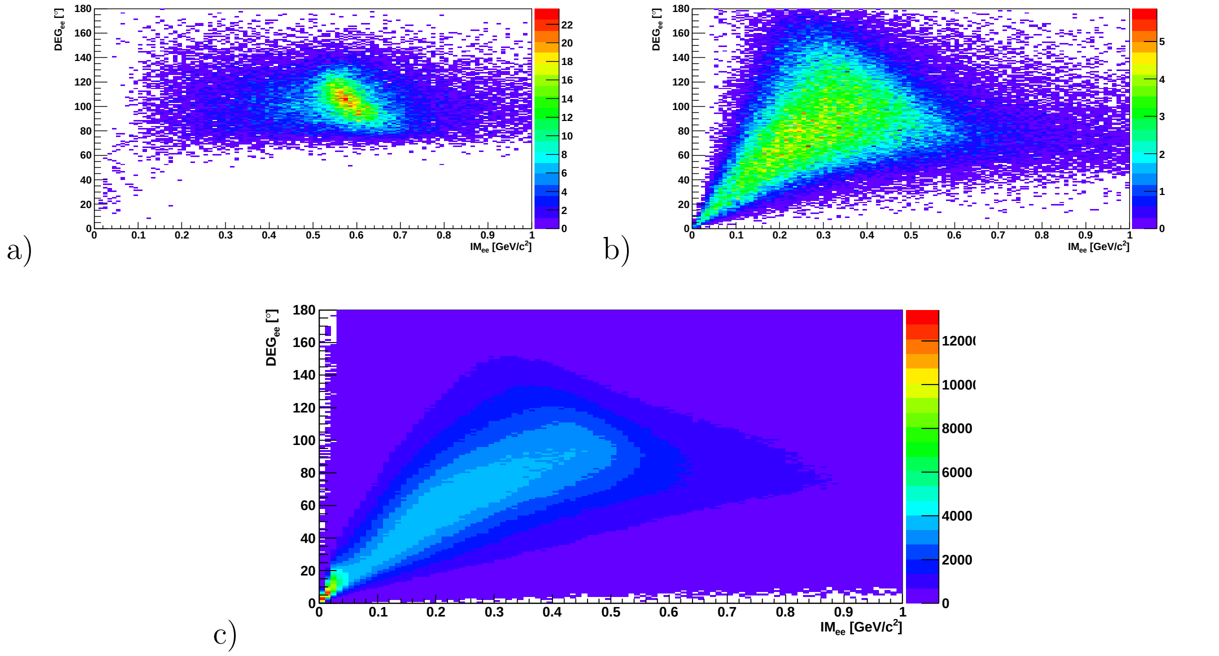

Figure 100: *Invariant mass of electron-positron pair as a function of opening angle between electron and positron for: a) generated signal, b)* $\pi^+\pi^-$ *background simulation, c) data.*

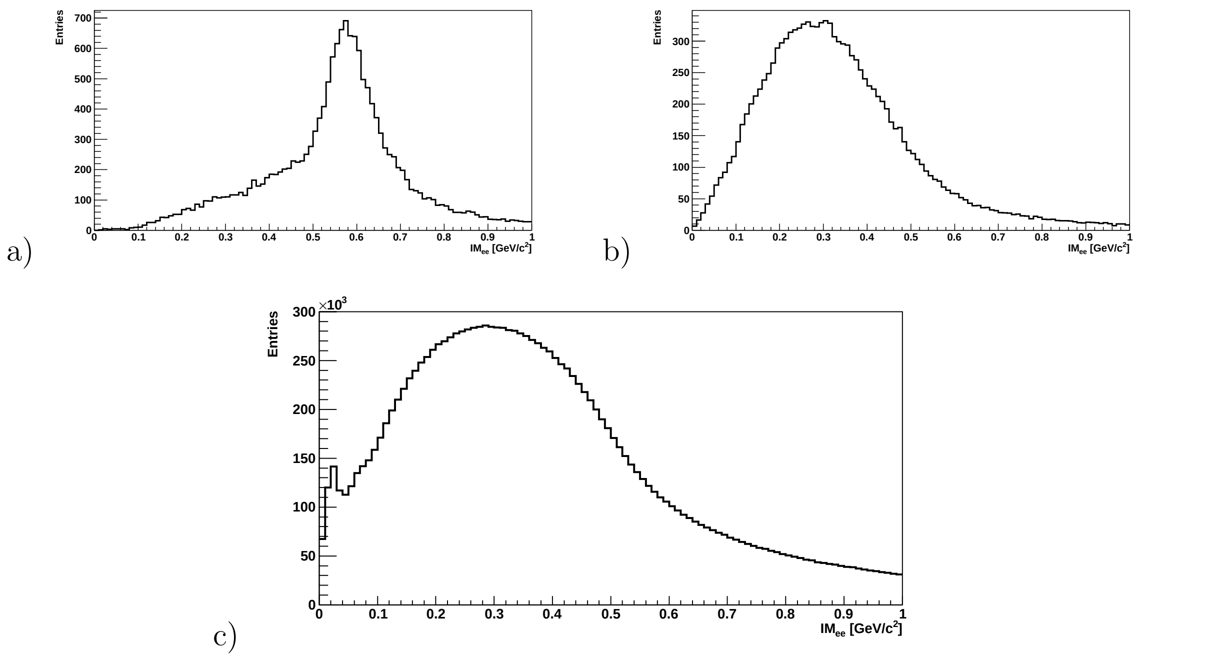

Figure 101: *Invariant mass of electron-positron pair for: a) generated signal, b)* $\pi^+\pi^-$ *background simulation, c) data.*

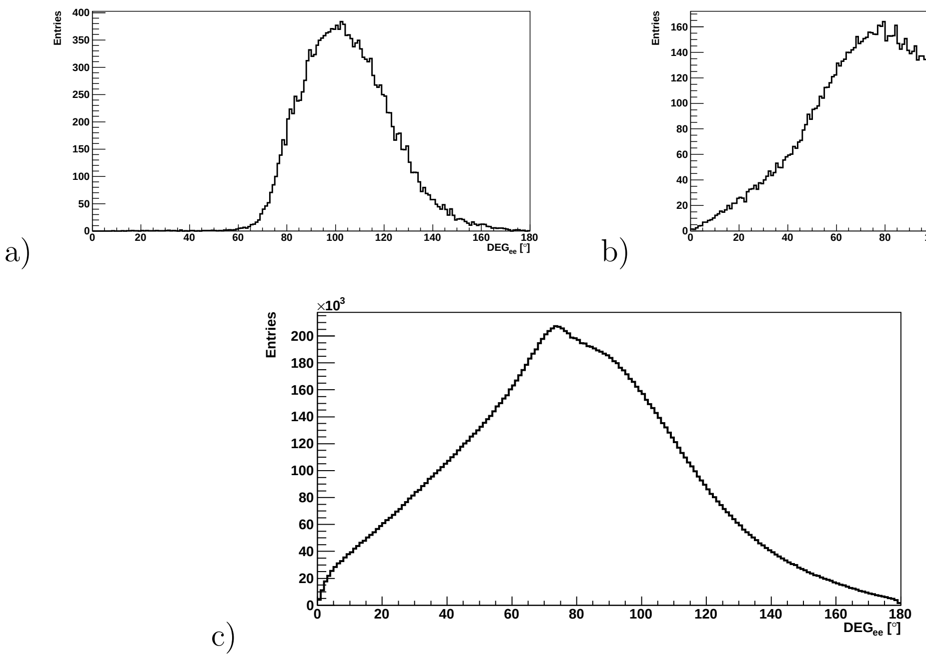

Figure 102: *Opening angle between electron and positron for: a) generated signal, b) $\pi^+\pi^-$ background simulation, c) data.*

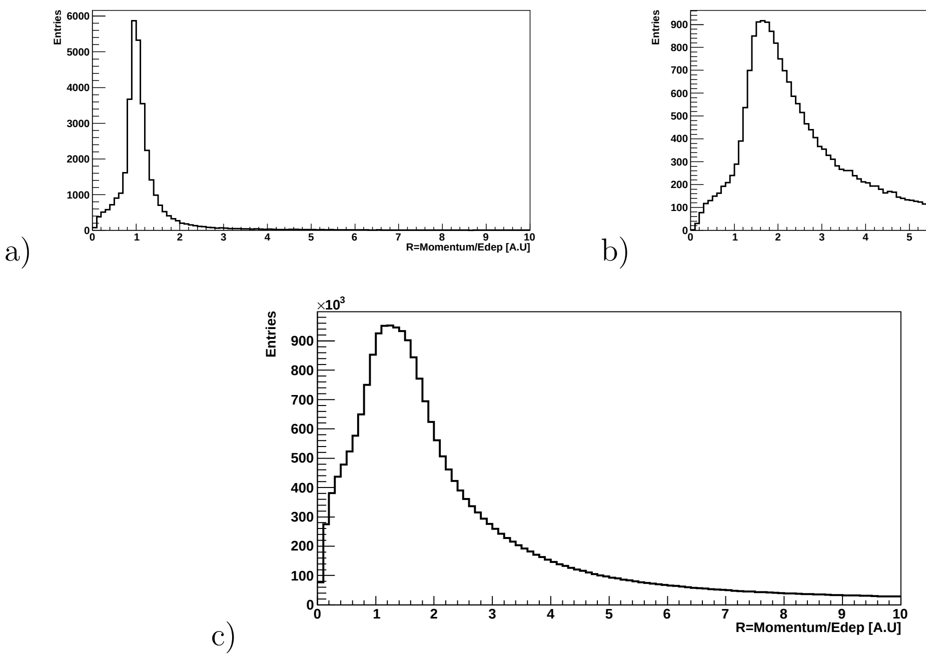

Figure 103: *Ratio between momentum and energy deposit for: a) generated signal, b) $\pi^+\pi^-$ background simulation, c) data.*

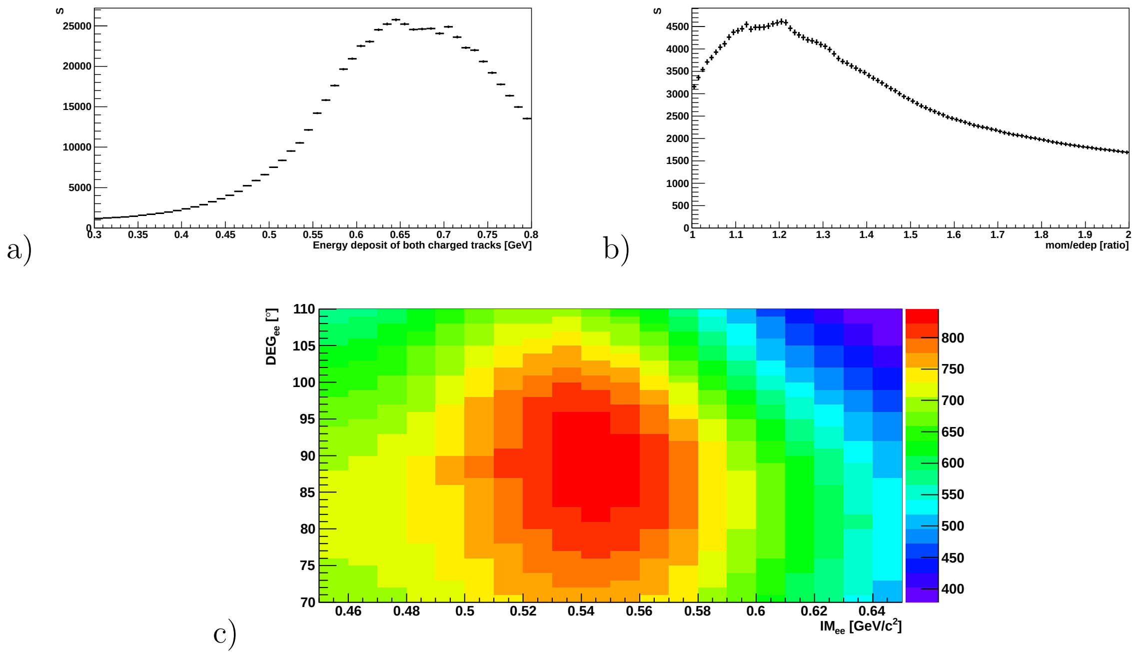

Figure 104: *The results of optimization procedure. The points shows the value obtained from the formula 27 for a given cut used in the analysis. Optimization of: a) sum of energy deposits in electromagnetic calorimeter for both electron and positron, b) ratio between particles momentum and it's energy deposit in electromagnetic calorimeter, c) invariant mass of electron-positron pair as a function of opening angle between electron and positron.*

Property	Without cuts	IM_{ee}	DEG_{ee}	$EdepSum$	$Ratio$	All cuts
Cut obtained	—	$> 480\ MeV$	$> 77°$	$> 550\ MeV$	< 1.2	—
Signal	38.1%	24.4%	36.7%	32.8%	19.0%	5.8%
Expected $\pi^+\pi^-$	17.7%	6.0%	15.7%	0.00%	0.13%	$< 0.001\%$
Expected Δ	4.4%	0.5%	0.8%	0.7%	1.3%	0.01%
Expected Dalitz	10.5%	0.9%	9.9%	1.7%	5.5%	0.01%
Data reduction	$1.7 \cdot 10^7$ ev	97%	50%	93%	20%	300 ev

Table 11: *Results of the optimization procedure, where ,,Without cuts" shows the acceptance for particular reaction channel after reconstruction and topology conditions, ,,All cuts" is the acceptance after all cuts mentioned. The EdepSum stands for sum of energy deposits in electromagnetic calorimeter for both electron and positron, IM_{ee} is invariant mass of electron-positron pair, DEG_{ee} denotes opening angle between electron and positron, Ratio means ratio between particles momentum and it's energy deposit in electromagnetic calorimeter.*

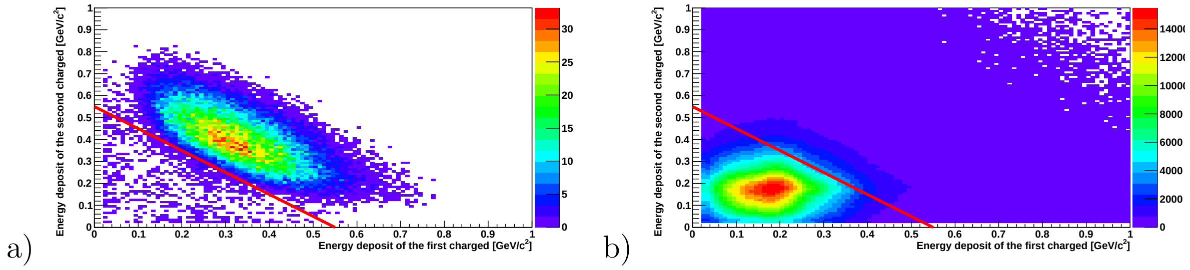

Figure 105: *Deposited energy of each of the selected central detector charged tracks. a) $\eta \to e^+e^-$ simulated signal and b) data. The selection condition is shown in red, only events above the line are accepted.*

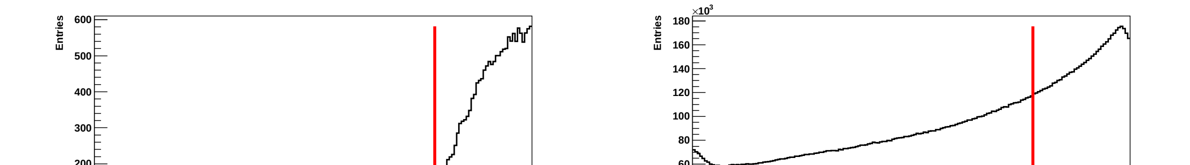

Figure 106: *Distributions of the opening angle between the selected central detector charged tracks on the XY plane. a) $\eta \to e^+e^-$ simulated signal and b) data. The selection condition is shown in red, only events right to the line are accepted.*

- Invariant mass of the selected charged tracks in the central detector greater than 0.48 MeV (see fig.107)

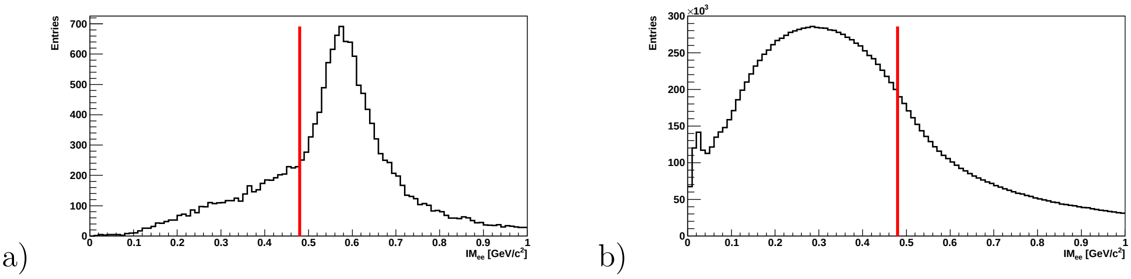

Figure 107: *Invariant mass of the selected electron and positron pair. a) $\eta \rightarrow e^+e^-$ simulated signal and b) data. The selection condition is shown in red, only events right to the line are accepted.*

- Both charged tracks in the central detector identified as electrons by the ratio R between momentum and energy deposited in the electromagnetic calorimeter, $0.8 < R < 1.1$ (see fig.108). The lower value of cut corresponds to the rejection of events for which energy deposit is substantially larger than reconstructed momentum indicating the merging with to many clusters in electromagnetic calorimeter.

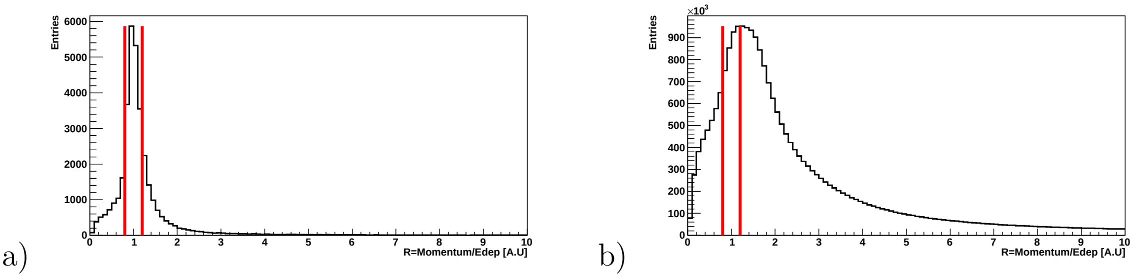

Figure 108: *Identification of charged tracks in the central detector by the ratio R between momentum and energy deposited in the electromagnetic calorimeter. a) $\eta \rightarrow e^+e^-$ simulated signal and b) data. The selection conditions are shown in red, only events between the lines were accepted.*

7 Results

In the search for $\eta \rightarrow e^+e^-$ decay the first step was determination of the main background sources which appeared to be: $pp \rightarrow pp\pi^+\pi^-$, $pp \rightarrow pp(\eta \rightarrow e^+e^-\gamma)$, combinatorial background and $pp \rightarrow p(\Delta(1232) \rightarrow pe^+e^-)$. The direct two charged pion production has about 150 time larger cross-section then the eta meson production. The single Dalitz decay of the eta meson leads to the same final state charged particles, if the mass of virtual photon is close to the η meson mass and real low energy photon is not observed. The combinatorial background contribution can be driven from data and it's caused by wrong track selection in the overlapping events or from two pairs. The radiative decay of Delta(1232) resonance leads to the the same final state as $\eta \rightarrow e^+e^-$. According to the Monte Carlo distributions mentioned before and signal simulation optimization procedure for cuts were evoked. The particles in the Central Detector were identified using two different methods: energy deposited in electromagnetic calorimeter and by using ratio of deposited energy to a particle momentum.

7.1 Background Contribution

Event selection for the $\eta \rightarrow e^+e^-$ (see section 6.4) included requiring at least two protons in the Forward Detector (if there were more, two closest in time were used), veto on neutral particles in the Central Detector of energy more than 20 MeV, at least two oppositely charged (if more, two giving the greatest opening angle were used) and time correlation between both charged in Central Detector and protons in the Forward Detector. After this step of analysis (see section 6.6) 300 event candidates remain in the whole data sample in the plot of the missing mass of two protons (see fig.109). using cut optimization (see section 6.5), obtaining Monte Carlo signal acceptance $Acc = 5.2\%$ (defined and described using the equation 13 in the section 4). The number of event candidates in the range of MM_{pp} 0.5-0.6 GeV is equal to 207. The plot shows an example of distribution obtained from the Monte Carlo simulation signal shape fit (blue line) above the polynomial background (red line). The sum of the two distributions mentioned before is plotted in black. The number of possible candidates for $\eta \rightarrow e^+e^-$ decay channel derived from the example of signal shape distribution is $N_{ev} = 35.6 \pm 13.0$ with the expected number of events coming from $\eta \rightarrow e^+e^-\gamma$ decay $N_{bcg} = 3.5 \pm 1.5$, where the other η meson decay channels contribution were found to be negligible. The statistical error for the number of events derived from the signal shape is taken from the fit parametrization. The results of analysis are summarized in table 12, where the expected number of events contributing to the MM_{pp} from different Monte Carlo simulations are shown. The table 1 from [70] was used to calculate the errors of small number of events. As for the combinatorial background contribution we used the equation 20 from the subsection 6.2.4. The numbers used for was as follows: $N_{++} = 43$ and $N_{--} = 4$, which gives $N_{CB} = 2\sqrt{N_{++} \cdot N_{--}} = 26$. The other background channels shows 0 events contributing at this level but if there was even one simulated event candidate it could explain the possible excess of data events over the expectations.

For the branching ratio limit calculations for a different confidence level we are using the

Reaction channel	N_{gen}	N_{ev}	Remarks
$pp \to pp\pi^+\pi^-$	10^7	63^{+158}_{-17}	$IM(\pi^+\pi^-)$ equal to the η mass
$pp \to pp(\eta \to e^+e^-\gamma)$	10^5	$3.5 \pm 1.5^*$	Generated with $IM_{ee} > 0.3$ GeV
$pp \to p(\Delta(1232) \to pe^+e^-)$	10^6	$4.5 \pm 2.3^*$	
combinatorial background	—	26 ± 7	Driven from data
$\eta \to e^+e^-$ signal	10^6	—	$Acc = 5.2\%$
data	—	207	

Table 12: *N_{gen} - Number of background or signal events generated, N_{ev} - Expected number of events for a selected background channel reaction in comparison to number of data event candidates both in the range of MM_{pp} equal to 0.5-0.6 GeV. * - based on weighted events.*

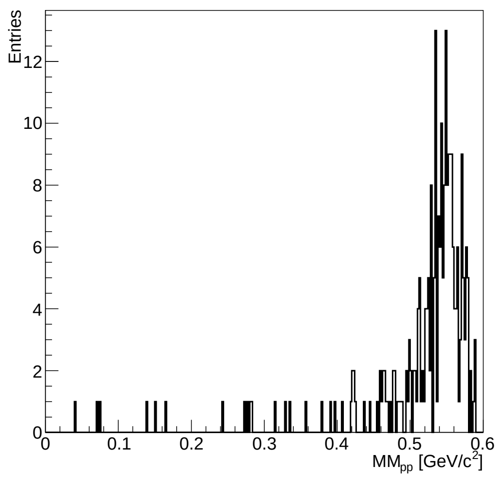

a)

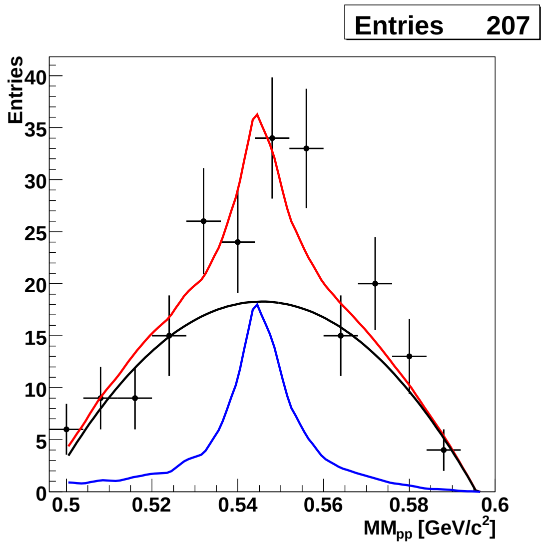

b)

Figure 109: *Missing mass of two protons for data $\eta \to e^+e^-$ event candidates after particle and time selection and optimized cuts (a). On the right side the same distribution in the restricted area after rebinning with superimposed fit results is shown. Red line shows the sum of fitted signal shape (blue line) and polynomial background (black line). For more details please refer to the text.*

equation taken from [69] proposed by Feldman and R. D. Cousins:

$$BR_{limit} = BR + \lambda \cdot \sigma_{BR} = \frac{(N_{ev} - N_{bcg}) + \lambda \cdot \sigma_{ev}}{Acc \cdot N_{\eta}}, \quad (28)$$

where σ_{ev} is the statistical error on number of event candidates, Acc stands for the simulated signal acceptance, and N_η is the total number of η mesons produced obtained in the section 4. The λ term depends on the assumed confidence interval via formula:

$$\int_{-\infty}^{\mu+\lambda\sigma} \frac{1}{\sigma\sqrt{2\pi}} exp\left[-\frac{1}{2}\left(\frac{x-\mu}{\sigma}\right)^2\right] dx = \frac{1}{2}\left[1 + erf\left(\frac{\lambda}{\sqrt{2}}\right)\right] = CL, \quad (29)$$

where the mean value μ (corresponding to the BR value) and standard deviation σ (corresponding to the σ_{BR} value) are taken from the equation 28. If we consider Confidence Level (CL) equal to 90%, the λ value fulfilling this equation is 1.28. The branching ratio limits using various fit intervals and assumed types of background functions are summarized in table 13.

The other approach is to fit only background shape in the range of MM_{pp} equal to 0.5-0.6 GeV using the polynomial function assuming that no signal is visible. The corresponding plots are shown in fig.110, where the right hand side picture shows the background subtracted spectrum. Number of events in the subtracted spectrum in the range of MM_{pp} equal to 0.5-0.6 GeV is equal to 20 ± 14 and the value of upper limit obtained using this method and the equation 28 is equal to $2.1 \cdot 10^{-5}$ *at CL* 90%.

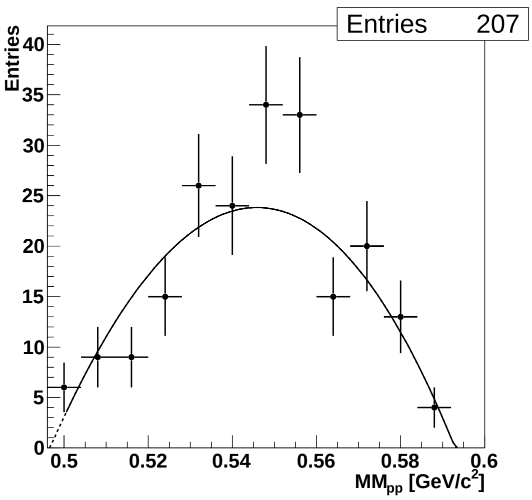

a)

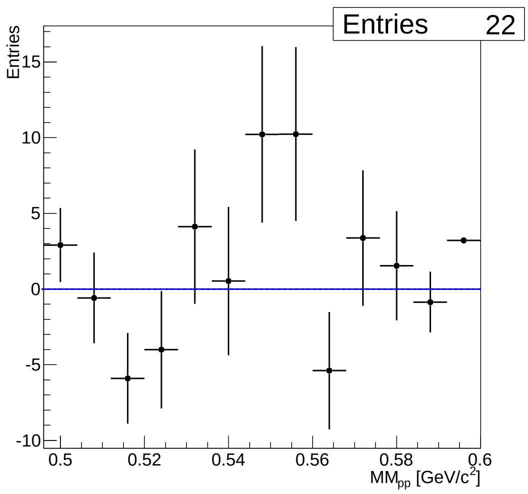

b)

Figure 110: *Figure a) shows the missing mass of two protons for data $\eta \to e^+e^-$ event candidates after particle and time selection and optimized cuts with superimposed fit results (black line), b) shows the background subtracted spectrum (last point is not taken into account).*

The value of branching ratio limit is dependent on the range of fitting and varies also with different background function assumed therefore further cleaning cuts were applied.

background function	MM_{pp} fit range	N_{ev}	Signal Acc
poly3	[0.50-0.60]	35.6 ± 14.5	5.2%
poly3	[0.52-0.58]	24.6 ± 14.7	4.9%
poly3	[0.52-0.60]	9.2 ± 13.6	4.9%
poly3	[0.50-0.58]	36.7 ± 14.1	5.2%
poly2	[0.50-0.60]	36.3 ± 12.9	5.2%
poly2	[0.52-0.58]	29.7 ± 14.6	4.9%
poly2	[0.52-0.60]	24.1 ± 13.1	4.9%
poly2	[0.50-0.58]	40.2 ± 14.1	5.2%

Table 13: *Number of $\eta \rightarrow e^+e^-$ event candidates, Monte Carlo acceptance after selection criteria and Branching Ratio limit calculations for different background fit functions (polyX denotes a polynomial function of a given order) and in the several ranges of missing mass of two protons (MM_{pp}). N_{ev} - Number of data event candidates taken from the fit parameters; Signal Acc - Acceptance taken from $\eta \rightarrow e^+e^-$ channel simulation under this condition.*

7.2 Final Analysis of the $\eta \rightarrow e^+e^-$ Decay

The effective rejection of $\eta \rightarrow e^+e^-$ decay candidates was obtained with the following cuts:

- time and multiplicity cuts given in the subsection 6.4;
- sum of energy deposits for the central detector charged tracks $> 550\ MeV$;
- invariant mass of $e^+e^- > 0.48\ GeV$;
- opening angle between electron and positron $> 77°$;
- ratio between momentum and energy deposit in the electromagnetic calorimeter between 0.8 and 1.1;
- opening angle between the central detector selected charged tracks on the XY plane greater than 140°;

The lack of the signal events after cuts mentioned above leads us to the calculated branching ratio upper limit equal to $2.1 \cdot 10^{-6}$ *at CL* 90% using the formula 28.

Since the equation 28 does not incorporate the systematic uncertainty in the experiment, we consider a formula taken from [71] proposed by Cousins and Highland. It includes systematic error with a Bayesian treatment of statistical approach for a case where the small number of events are observed.

$$U_n = U_{n0}(1 + E_n\sigma^2_{syst}/2), \tag{30}$$

where U_n is a new upper limit, U_{n0} denotes the classical value of upper limit, where no event are observed, with the 90% confidence level parameter, which is $ln10 \approx 2.30$, $E_n \equiv U_{n0} - n$ stands for the excess of the classical upper limit over the number n of observed events, and

σ_{syst} is the systematic uncertainty. In our case, due to the fact that no events are seen in the area of interest and we have no background contribution, the equation 30 simplifies to:

$$U_n = U_{n0} + U_{n0}^2 \sigma_{syst}^2 / 2. \tag{31}$$

It was assumed that the systematic error is dominated by the difference of the normalization obtained from $\eta \rightarrow \gamma\gamma$ and $\eta \rightarrow e^+e^-\gamma$ channel shown in the end of section 5. This error is as large as 15%. Taking this factor into account in the formula 31 we obtain the corrected value of 90% confidence level branching ratio upper limit:

$$BR_{limit} = \ 3.9 \cdot 10^{-6} \ at \ CL \ 90\%.$$

This number is almost an order of magnitude better than the previous result obtained by CELSIUS/WASA collaboration ($2.7 \cdot 10^{-5}$ *at* $CL = 90\%$) and slightly better than the most recent measurement from the HADES Collaboration ($4.9 \cdot 10^{-6}$ *at* $CL = 90\%$) [20].

8 Summary and Outlook

During a two week experiment performed at 2008 the WASA-at-COSY collaboration collected a sample of η meson decays corresponding to about $5.91 \cdot 10^7$ mesons produced. The experiment took place at Institute for Nuclear Physics of the Forschungszentrum Juelich in Germany using Wide Angle Shower Apparatus (WASA) detection system. The detector was installed at the Cooler Synchrotron (COSY) storage ring. Data sample was collected using the reaction $pp \to ppX$ at the incident proton energy of 1.4 GeV. The internal proton beam was scattered on frozen hydrogen pellets crossing the beam. All the final particles, both charged and neutral, were detected and measured in the dedicated parts the WASA detector which covers nearly 4π of decay space. Detector was constructed in order to allow the search for very rare light meson decays into e^+e^- pair and to minimize the possible background from external conversion by using specially designed pellet target system and low amount of structural material. The production of η meson was identified using the missing mass technique. In this work the various electromagnetic η meson decays were observed and its properties were measured. The new trigger system based on high energy deposits in both halves of electromagnetic calorimeter developed especially for such decays of the η meson was tested. Its performance was examined and its operation was implemented into the analysis software. The performance of the WASA detector was investigated using more frequent decay channels like $\eta \to \gamma\gamma$ and $\eta \to e^+e^-\gamma$. Those two decay modes served as a testing field for the extraction of the reconstruction efficiency, crosscheck of normalization and moreover for testing the response of the detector for electron-positron pairs of various energies. For this processes several tests were performed on conversion reduction, simulation of beam interaction with the rest gas, vertex size and its position and trigger response for particles of different energies.

It was checked that the normalization is in agreement within 15% error between $\eta \to \gamma\gamma$ and $\eta \to e^+e^-$ channel. We see resonable agreement in the shape between data and Monte Carlo simulations for the invariant mass and missing mass distributions.

The main goal of this work was searching for $\eta \to e^+e^-$ rare decay. The various cuts that permit efficient selection of this channel were elaborated on the base of Monte Carlo generated events. The simulations were performed for the signal and several background channels as for example single Dalitz decay of η meson, direct two charged pion production and Dalitz decays of baryonic resonances. For the applied cuts optimization procedure were developed. The following studies allowed to put a branching ratio upper limit for this process $3.9 \cdot 10^{-6}$ *at CL* 90%. This number is better than the best measured value in the international database coming from HADES collaboration. Unfortunately both results are still three orders of magnitude above the theoretical predictions from the Standard Model for the decay and at least two orders of magnitude above the expected hypothetical interactions that arise from physics beyond the Standard Model.

It was shown that WASA detector is a perfect tool in the field of searching for rare light meson decays. The developed techniques and the experience gained could be used in the analysis of the data taken during the last years of WASA detector operation. The much higher statistics nowadays available will allow to push the border even further.

References

[1] T.N. Pham, *$\eta - \eta'$ mixing angle from Vector Meson Radiative Decays*, Phys.Lett.B694:129-133 (2010), arXiv:hep-ph/1005.5671

[2] A. Bramon, R. Escribano and M.D. Scadron, *The $\eta - \eta'$ mixing angle revisited*, Eur.Phys.J.,C7:271-278 (1997), arXiv:hep-ph/9711229

[3] K. Nakamura *et al.* (Particle Data Group), Journal of Physics G37, 075021 (2010) and 2011 partial update for the 2012 edition.

[4] S. Drell, *Direct decay $\pi^\circ \to e^+e^-$*, Nuov.Cim.XI:693 (1959)

[5] S.M. Berman and D.A. Geffen, *The Electromagnetic Structure and Alternative Decay Modes of the* π°, Nuov.Cim.XVIII:1192 (1960)

[6] L. Bergstroem, *Rare decay of a pseudoscalar meson into a lepton pair: A way to detect new interactions?*, Zeit.Phys.C14:129 (1982)

[7] G.V. Efimov, M.A. Ivanov, R.K. Muradov, and M.M. Solomonovich, *Decays $P \to l^+l^-$ in nonlocal quark model*, J.Lett.34:221 (1981)

[8] R.E. Cutkosky, *Singularities and discontinuities of Feynman amplitudes*, J.Math.Phys.1:429 (1960)

[9] S. Mandelstam, *Analytic properties of transition amplitudes in perturbation theory*, Phys.Rev.115:1741 (1959)

[10] T. Petri, *Anomalous decays of pseudoscalar mesons*, Diplom-Thesis (2010), arXiv:nucl-th/1010.2378

[11] A.E. Dorokhov, M.A. Ivanov, and S.G. Kovalenko *Complete structure dependent analysis of the decay $P \to l^+l^-$*, Phys.Lett.B677:145 (2009), arXiv:hep-ph/0903.4249

[12] M.J. Savage, M.E. Luke, and M.B. Wise, *The Rare Decays $\pi^\circ \to e^+e^-$, $\eta \to e^+e^-$ and $\eta \to \mu^+\mu^-$ in Chiral Perturbation Theory*, Phys.Lett.B291:481 (1992), arXiv:hep-ph/9207233

[13] A.E. Dorokhov and M.A. Ivanov, *Rare decay $\pi^\circ \to e^+e^-$: theory confronts KTeV data*, Phys.Rev.D75:114007 (2007) arXiv:hep-ph/0704.3498

[14] D. Gomez Dumm and A. Pich, *Long-distance contributions to the $K_L \to \mu^+\mu^-$ decay width*, Phys.Rev.Lett.80:4633 (1998) arXiv:hep-ph/9801298

[15] M. Knecht, S. Peris, M. Perrottet, and E. de Rafael, *Decay of pseudoscalars into lepton pairs and large-Nc QCD*, Phys.Rev.Lett.83:5230 (1999), arXiv:hep-ph/9908283

[16] J.D. Davies *et al.*, *Experimental Limits to the $\pi^\circ \to e^+e^-$ Rate and their Consequences for a Direct Electron Hadron Coupling*, Nuov.Cim.24A:324 (1974)

[17] D.B. White *et al.*, *Search for the Decays $\eta \to \mu e$ and $\eta \to e^+e^-$*, Phys.Rev.D53:6658-6661 (1996)

[18] T.E. Browder *et al.*, *A New Upper Limit on the Decay $\eta \to e^+e^-$*, Phys.Rev.D56:5359 (1997), arXiv:hep-ex/9706005

[19] M. Berłowski *et al.* [CELSIUS/WASA], *Measurement of eta meson decays into lepton-antilepton pairs*, Phys.Rev.D77:032004 (2008), arXiv:hep-ph/0711.3531

[20] G. Agakichiev *et al.*, *Inclusive dielectron spectra in p+p collisions at 3.5 GeV*, Eur.J.Phys.A48:64 (2012), arXiv:1112.3607v1 [nucl-ex]

[21] A.E. Dorokhov and M.A. Ivanov, *On mass corrections to the decay $P \to l^+l^-$*, J.Lett.87:531536 (2008), arXiv:hep-ph/0803.4493

[22] Y. Kahn, M. Schmitt, and T.M.P. Tait, *Enhanced rare pion decays from a model of MeV dark matter*, Phys.Rev.D78:115002 (2008), arXiv:hep-ph/0712.0007

[23] P. Fayet, *Parity violation effects induced by a new gauge boson*, Phys.Lett.B96:83 (1980)

[24] P. Fayet, *A la recherche d'un nouveau boson de spin un*, Nucl.Phys.B187:184 (1981)

[25] C. Boehm and P. Fayet, *Scalar Dark Matter candidates*, Nucl.Phys.B683:219263 (2004), arXiv:hep-ph/0305261

[26] C. Boehm, T.A. Ensslin and J. Silk, *Can annihilating Dark Matter be lighter than a few GeVs?*, J.Phys.G30:279286 (2004), arXiv:astro-ph/0208458

[27] C. Boehm *et al.*, *MeV Dark Matter: Has It Been Detected?*, Phys.Rev.Lett.92:101301 (2004), arXiv:astro-ph/0309686

[28] C. Boehm and Y. Ascasibar, *More evidence in favour of Light Dark Matter particles?*, Phys.Rev.D70:115013 (2004), arXiv:hep-ph/0408213

[29] P. Fayet, *Light spin-1/2 or spin-0 Dark Matter particles*, Phys.Rev.D70:023514 (2004) arXiv:hep-ph/0403226

[30] O. Adriani *et al.* [PAMELA Collaboration], *Observation of an anomalous positron abundance in the cosmic radiation*, Nature 458 (2009) 607, arXiv:0810.4995

[31] J. Chang *et al.*, *An excess of cosmic ray electrons at energies of* 300800 *GeV*, Nature 456 (2008) 362

[32] F. Aharonian *et al.* [H.E.S.S. Collaboration], *The energy spectrum of cosmic-ray electrons at TeV energies*, Phys.Rev.Lett.101 (2008) 261104, arXiv:0811.3894

[33] P. Jean *et al.*, *Early SPI/INTEGRAL measurements of galactic 511 keV line emission from positron annihilation*, Astron.Astrophys.407 (2003) L55, arXiv:astro-ph/0309484

[34] R. Abegg *et al.*, *Measurement of the branching ratio for the decay $\eta \to \mu^+\mu^-$*, Phys.Rev.D50:92103 (1994)

[35] B. Trostell, *Vacuum injection of hydrogen micro-sphere beams*, Nucl.Instr.Meth.A362 (1995) 41

[36] C. Ekstrom *et al.*, *Hydrogen pellet targets for circulating particle beams*, Nucl.Instr.Meth.A371 (1996) 572

[37] R. J. M. Y. Ruber, *An ultrathin walled superconducting solenoid for meson decay physics*, PhD. Thesis, Uppsala Universitet, Sweden (1999)

[38] M. Jacewicz, *Measurement of the reaction $pp \to pp\pi^+\pi^-\pi^\circ$ with CELSIUS/WASA at 1.36 GeV*, PhD thesis, Uppsala Universitet, Sweden, (2004)

[39] J. Zabierowski and J. Rachowski, *The Light-Pulser Monitoring System for the WASA detector facility*, Nucl.Instrum.Meth.A606 (2009) 411-418

[40] I. Koch, *Measurements of $2\pi^\circ$ and $3\pi^\circ$ Production in Proton-Proton Collisions at a Center of Mass Energy of 2.465 GeV*, PhD thesis, Uppsala Universitet, Sweden, (2004)

[41] H. Kleines *et al.*, *Performance Issues of the New DAQ System for WASA at COSY*, IEEE Transactions on Nuclear Science 55(1):261-264, (2008)

[42] C. F. Redmer, *In search of the Box-Anomaly with theWASA facility at COSY*, Doctoral thesis, Bergische Universitat Wuppertal, (2010)

[43] K. Fransson, *The trigger system of the CELSIUS/WASA detector*, Phys.Scripta T99:176-182 (2002)

[44] I. Froehlich *et al.*, *Pluto: A Monte Carlo Simulation Tool for Hadronic Physics*, PoSACAT2007,076 (2007), arXiv:0708.2382 [nucl-ex]

[45] I. Froehlich *et al.*, *Design of the Pluto Event Generator*, J.Phys.Conf.Ser.219:032039 (2010), arXiv:0905.2568 [nucl-ex]

[46] http://root.cern.ch

[47] R. Brun and F. Rademakers, *ROOT - An Object Oriented Data Analysis Framework*, Nucl.Instr.Meth.Phys.Res.A389 (1997) 8186

[48] F. James, *W515 N-Body Monte-Carlo Event Generator*, Technical report (1975)

[49] R. Brun, F. Carminati and S. Giani, *GEANT Detector Description and Simulation Tool*, CERN-W5013

[50] Application Software Group Computing and Networks Division, *GEANT - Detector Description and Simulation Tool*, Technical report (1993)

[51] V. Hejny, M. Hartmann, and A. Mussgiller, *RootSorter: A New Analysis Framework for ANKE*, IKP / COSY Annual Report 2002 (2003) Juel-4052

[52] M. Komogorov, B. Morosov, A. Povtorejko, V. Tikhomirov, *Track recognition algorithm for WASA Mini Drift Chamber*, WASA Memo 97-11 (1997)

[53] C. Zheng, *Matching Trigger Efficiency of Forward Detector of WASA-at-COSY*, Berichte des Forschungszentrums Juelich Juel-4282, (2009) ISSN 0944-2952

[54] C. Adolph *et al.* [The WASA-at-COSY Collaboration], *Measurement of the $\eta \to 3\pi^\circ$ Dalitz Plot Distribution with the WASA Detector at COSY*, Phys.Lett.B677 (2009) 24-29, arXiv:0811.2763 [nucl-ex]

[55] E. Chiavassa *et al.*, *Measurement of the $pp \to pp\eta$ total cross section between 1.265 and 1.50 GeV*, Phys.Lett.B322 (1994) 270-274

[56] C. Pauly *et al.*, *The $pp \to pp\pi\pi\pi$ reaction channels in the threshold region*, Phys.Lett.B649 (2007) 122-127, arXiv:nucl-ex/0602006

[57] S. A. Bass *et al.*, *Microscopic Models for Ultrarelativistic Heavy Ion Collisions*, Prog.Part.Nucl.Phys.41 (1998) 255-369, arXiv:nucl-th/9803035

[58] M. I. Krivoruchenko *et al.*, *Electromagnetic transition form factors and dilepton decay rates of nucleon resonances*, Annals Phys. 296 (2002) 299-346, arXiv:nucl-th/0110066

[59] S. Teis *et al.*, *Pion-Production in Heavy-Ion Collisions at SIS energies*, Z.Phys.A356 (1997) 421-435, arXiv:nucl-th/9609009

[60] L. G. Landsberg, *Electromagnetic Decays of Light Mesons*, Phys.Rept.128 (1985) 301-376

[61] N. M. Kroll and W. Wada, *Internal pair production associated with the emission of high-energy gamma rays*, Phys.Rev.98 (1955) 1355-1359

[62] H. Berghauser *et al.*, *Determination of the eta-transition form factor in the $\gamma p \to p\eta \to p\gamma e^+e^-$ reaction*, Phys.Lett.B701 (2011) 562-567

[63] A. Faessler, C. Fuchs, M.I. Krivoruchenko, B.V. Martemyanov, *Dilepton production in proton-proton collisions at BEVALAC energies*, J.Phys.G29 (2003) 603-624, arXiv:nucl-th/0010056

[64] A. Faessler, C. Fuchs, M.I. Krivoruchenko, *Dilepton spectra from decays of light unflavored mesons*, Phys.Rev.C61 (2000) 035206, arXiv:nucl-th/9904024

[65] B.V. Martemyanov, private communication

[66] J. Bijnens, F. Persson, *Effects of different Form-factors in Meson-Photon-Photon Transitions and the Muon Anomalous Magnetic Moment*, LU TP (1999) 99–39, arXiv:hep-ph/0106130

[67] W. Kuhn *et al.*, *Meson production in p p reactions at 2.85 GeV*, Nucl.Phys.A684 (2001) 440-442

[68] L. Ametller, J. Bijnens, A. Bramon and F. Cornet, *Transition form-factors in π°, η and η' couplings to $\gamma\gamma*$*, Phys.Rev.D45 (1992) 986-989

[69] G. J. Feldman and R. D. Cousins, *Unified approach to the classical statistical analysis of small signals*, Phys.Rev.D57 (1998) 3873-3889

[70] O. Helene, *Errors in experiments with small numbers of events*, Nucl.Instr.Meth.Phys.Res.A228 (1984) 120-128

[71] R. D. Cousins and V. L. Highland, *Incorporating systematic uncertainties into an upper limit*, Nucl.Instr.Meth.Phys.Res.A320 (1992) 331-335